ASSESSMENT OF PARTICULATE ACCUMULATION CLIMATOLOGY

UNDER INVERSIONS IN GLACIER BAY FOR THE

2008 TOURIST SEASON USING WRF/CHEM DATA

By

Michael A. Pirhalla

RECOMMENDED: _____
                             Dr. Uma Bhatt

                           _____
                             Dr. Igor Polyakov

                             _____
                             Dr. Scott Gende

                             _____
                             Dr. Nicole Mölders
                             Advisory Committee Chair

                             _____
                             Dr. Uma Bhatt
                             Chair, Department of Atmospheric Sciences

APPROVED: _____
                             Dr. Paul Layer
                             Dean, College of Natural Science and Mathematics

                             _____
                             Dr. John Eichelberger
                             Dean of the Graduate School

                             _____
                             Date

ASSESSMENT OF PARTICULATE ACCUMULATION CLIMATOLOGY

UNDER INVERSIONS IN GLACIER BAY FOR THE

2008 TOURIST SEASON USING WRF/CHEM DATA

A

THESIS

Presented to the Faculty

of the University of Alaska Fairbanks

in Partial Fulfillment of the Requirements

for the Degree of

MASTER OF SCIENCE

By

Michael A. Pirhalla, B.S.

Fairbanks, Alaska

May 2014

Abstract

Each summer, roughly one million tourists come to Southeast Alaska aboard cruise ships to see the pristine landscape and wildlife. Tourism is an integral component in the economy for most of the towns and villages on the Alaska Panhandle. With ship emissions only modestly regulated, there have been some concerns regarding the potential environmental impacts that cruise ships have on air quality, wildlife, and visitor experience. Cruise ships travel to remote regions, and are frequently the only anthropogenic emissions source in federally protected parks, such as Glacier Bay National Park and Preserve. In the absence of winds and synoptic scale storm systems common in the Gulf of Alaska, temperature inversions frequently develop inside Glacier Bay due to radiative cooling influenced by the complex topography inside the park. Inversions act as a lid, and may trap pollutants from cruise-ship emissions depending on the meteorological conditions present.

Since meteorological observations are sparse and frequently skewed to easily accessible locations, data from the Weather Research and Forecasting Model, coupled with a chemistry package (WRF/Chem), were used to examine the physical and chemical processes that are impossible to determine through direct observations. Model simulation data for 124 days during the 2008 tourist season (May 15 to September 15), including a cruise-ship emission inventory for all 225 cruise ship entries in Glacier Bay, was analyzed. Evaluation of WRF/Chem through meteorological observations reveals that the model accurately captures the synoptic conditions for most of the summer, despite problems with complex topography. WRF/Chem simulated quasi-multi-day inversion events, with strengths as high as 6.7 K $(100 \text{ m})^{-1}$. Inversions were present in all grid-cell locations in Glacier Bay, with inversions occurring on average of 42% of the days during the tourist season. WRF/Chem was able to model PM_{10} (particulate matter with diameter less than 10 μm) concentrations from cruise ships, but the absence of aerosol monitoring sites does not allow us to confirm the results. However, no simulated particulates ever exceed the daily average National Ambient Air Quality Standard (NAAQS) of 150 μg m^{-3}. The high variability of particle concentrations in Glacier Bay suggests the need for an air quality observational network to further assess local air quality issues.

Table of Contents

List of Figures

List of Tables

Acknowledgements

Lastly, I owe a huge thanks to my family, especially Alex and Helen Pirhalla and Barbara Lischak for the love and encouragement throughout my studies at UAF. The distance from home was difficult to manage, but I knew they were always a phone call away. I also would like to thank my best friends Ashley Tomlinson, Nicole Petrin, and Bobby Salerno for their support all the way from the New England.

Chapter 1 Introduction

With stunning vistas of snow-capped mountains, massive glaciers, and unique wildlife, Alaska is undoubtedly one of the most popular tourist destinations in the world. The Southeast Panhandle is a pristine location in Alaska, containing the largest national forest in the United States, Tongass National Forest. It is a Pacific temperate rainforest, due to its characteristic flora, fauna, and rainy climate (with up to or exceeding 3500 mm yr^{-1} in some places). Each summer, thousands of tourists arrive aboard cruise ships to see Alaska's natural beauty, and to tour sections of its six national parks and monuments. Between 2006-2011, approximately 1.1 million visitors per year came to Southeast Alaska, of which nearly 900,000 arrived aboard cruise ships (Wright et al. 2012). Cruise-ship traffic in Alaska peaked in 2008, but has slightly decreased since then. Passenger visits in Alaska dominated at approximately 65% of all visits at U.S. ports of call (CLIA 2012). As a result, tourism is the third most important form of commerce in Southeast Alaska, at 8% of total earnings. This equates to approximately $160 million in wages each year (Wright et al. 2012). The average cruise ship visitor will spend about $427 during their stay in Southeast Alaska, which excludes the cost of their cruise package (McDowell Group, Inc. 2012). Government employment and commercial fishing are the only two industries that surpass tourism.

Cruise-ship passengers keep small towns (with ≥ 100 inhabitants) and villages (≤ 100 inhabitants) thriving. Many towns have small numbers of permanent residents, but tend to see explosive population growth from May 15 to September 15 each year. This period is the typical Alaska tourism season. By 2011, the population in Southeast Alaska was 73,528 and it was the fastest growing region in the entire state (Wright et al. 2012). Southeast Alaska houses Juneau (population 32,164), Alaska's state capital and economic hub.

This thesis investigates the impact of cruise ships emissions on the environment in Southeast Alaska, with an emphasis on Glacier Bay National Park. With a sparse network of measurements, model data provided by Mölders et al. (2013) is used to gain understanding of the atmospheric conditions during the 2008 tourist season. The area of interest considers all of Southeast Alaska, plus the far southwest region of Yukon Territory, including the province's capital city of Whitehorse (pop. 23,276). A rough estimate of approximately 100,000 people in the domain of interest translates to just over eight people per 7x7 km^2 grid-cell in our numerical

model, making this region extremely remote and pristine. The road network connecting Southeast Alaska to rest of Alaska, Canada, and the lower 48 states links only three communities. The three towns: Haines, Hyder, and Skagway, have a combined population of 3,515, which is only about 4.8% of the entire population in Southeast Alaska. Transportation is mostly limited to ships and planes. Islands make up 40% of the total land area, and almost 95% of the land is managed by the Federal Government in the form of National Parks and Preserves.

Global shipping accounts for approximately 16% of transportation related fuel consumption, but produces far more pollutants (e.g. NO_x, SO_x, and sulfur) than automobile and aviation traffic combined. Ships emit about 1,200 times more particulate matter than airplanes (Eyring et al. 2005). While the worldwide fleet of cruise ships is relatively small (all passenger ships account for less than 7%; Buhaug et al. 2009), they often utilize highly traveled shipping lanes and dock in secluded towns targeted for tourists (Snyder 2007). An often-overlooked issue is the ecological and environmental impact cruise ships and their emissions impose on the unspoiled Alaska wilderness. In remote ports in Alaska, cruise ships may represent the only anthropogenic emission source, emitting pollutants directly into the relatively clean marine boundary layer (Eyring et al. 2005). Cruise ships entering Alaska National Parks pose a threat to endangered humpback whales, and lethal collisions have occurred (Gabriele et al. 2007). In sections of Glacier Bay National Park, habitats of harbor seals have also been disrupted (Young 2009). Furthermore, the anthropogenic emissions from cruise ships pose concerns for air quality, visibility, and acid deposition in Southeast Alaska.

1.1 Motivation

Ship emissions are currently modestly regulated, although in 2010, the International Maritime Organization (IMO) designated all waters approximately 320 km (200 miles) off North American coastlines to be Emission Control Areas (ECA; EPA 2010). By 2016, ship companies will need to adhere by stricter guidelines than today, such as using 0.1% sulfur fuel, which is expected to reduce particulate matter and SO_x emissions by more than 85% (EPA 2010). Alternatively, ships can be equipped with scrubbers on their exhaust systems to prevent sulfur from escaping into the surrounding air. While these ordinances are expected to cost ship companies an estimated $3.2 billion dollars by 2020 (EPA 2010), their expenses should greatly decrease ship emissions over coastal waters of the United States and Canada.
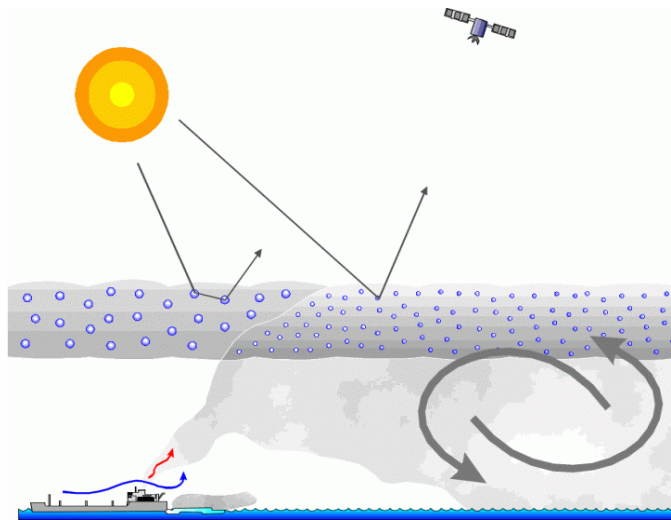
Figure 1.1 Schematic showing the impact of ship emissions on the marine boundary layer (MBL). Aerosols released from ships interact with clouds, precipitation development, and solar radiation. The aerosols compete for water vapor, leading to smaller cloud droplets that have higher albedo, and therefore produce ship trails in visible satellite imagery. From: D. Rosenfeld (2003), the Hebrew University of Jerusalem.

a)

b)
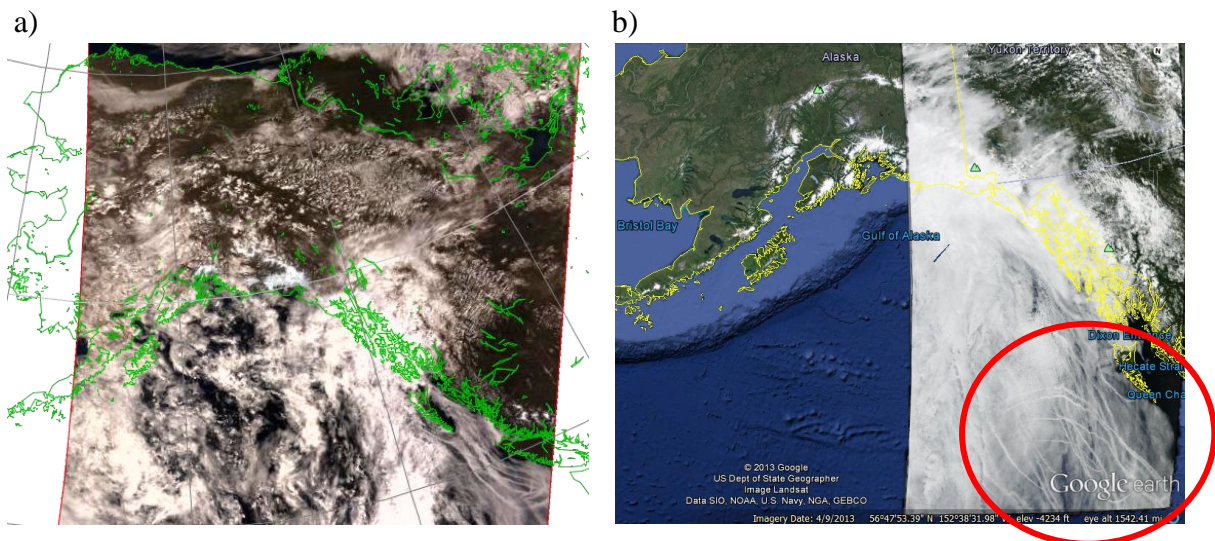
Figure 1.2 a) Ship tracks on MODIS Terra-1 satellite imagery off Vancouver Island and the Southern Alaska Panhandle on 11:20 am, August 16, 2008. b) More examples of ship tracks on June 11, 2010. Modified from: University of Alaska, GINA, www.gina.alaska.edu

Evidence of ship emissions can be validated by observing highly traveled shipping lanes on satellite imagery (Fig. 1.2). Long-lived, linear regions (nearly straight lines) of enhanced reflectivity that appear downwind of ships in maritime stratus are considered "ship tracks", and develop as ships release high quantities of particulates into the atmosphere that act as cloud

3

condensation nuclei (CCN; Hobbs et al. 2000). Cloud droplet formation may be enhanced by gas-to-particle conversion (Russell et al. 1999). Aerosols released from ships compete for water-vapor molecules, leading to large droplet concentrations but small cloud droplets, as they are less likely to grow by collision or coalescence (Radke et al. 1989). Ship tracks may modify existing clouds by increasing the droplet concentration. In addition, the annual reduction in radiative forcing from backscattered longwave radiation at the top of the atmosphere can be up to 43 Wm^{-2} in highly traveled shipping lanes (Schreier et al. 2006).

There are growing concerns in the public about the potential impacts of cruise ship activity and emissions on air quality, wildlife, and visitors' experience in the National Park Service (Mölders et al. 2013). Pollutants react with other atmospheric compounds and tend to degrade air quality and visibility by forming haze. High amounts of sulfur in fuel are oxidized during combustion, which produces sulfur dioxide (SO_2). When combined with water vapor in the air, SO_2 is quickly converted to sulfuric acid (H_2SO_4), and may be removed from the environment as acid rain. It is detrimental for vegetation and aquatic life, since sulfuric acid is corrosive. Nitrogen oxides (NO_x; including nitric oxide, NO, and nitrogen dioxide, NO_2) are produced as a byproduct of fuel combustion as it reacts with the surrounding air. These gases can form secondary particles, smog, ground-level ozone, and also have acidifying properties. Particulate matter (PM), which can be produced naturally from precursor gases existing in the atmosphere, or stem from primary anthropogenic emissions in the form of ultrafine particles and soot, also contribute to haze and reduced visibility.

Figure 1.3 The Diamond Princess cruise ship departing the port of Vancouver on July 5, 2008. This ship traveled through Alaska's Inside Passage sailing to: Ketchikan, Juneau, Skagway, Glacier Bay, and the College Fjord. (Photo: M. Pirhalla, 2008).

Limited point sources of pollution in Southeast Alaska make the area especially vulnerable to cruise-ship emission impacts. Cruise ships typically embark on seven-day itineraries through the Inside Passage, stopping at several ports along the way. Most cruise-ship companies will sail through Glacier Bay National Park and Preserve, a 13,287 km^2 expanse of deep fjords and numerous glaciers. It is within the National Park Service's (NPS) management goals to sustain visitor volume, while also improving tourists' experience. However, some guests have expressed concern about the increasing amounts of ship pollution in Glacier Bay (Scott Gende, personal communication, 2013).

The NPS manages a quota on the number of ships allowed to sail inside the park. In 2003, the Vessel Quota and Operating Requirements Final Environmental Impact Statement (VQOR EIS) set a restriction of two daily cruise-ship entries, and a total tourist season restriction of 139 vessels, which was later increased to 153 ships in 2007.

Year 2008 saw a peak number of tourists during the seven-year period from 2006-2011 (CLIA 2012), with a total of 225 cruise ships entering Glacier Bay (Mölders et al. 2013). The ships can be quite large (Fig. 1.3), with some capable of accommodating upwards of 8,000 passengers and crew members. Vessels typically spend a total of 9-12 hours inside the park. They enter the park at Icy Strait, sail through the steep fjords, and stop for glacier viewing as far as John Hopkins Inlet (Fig. 1.4) before turning around and exiting the park along the same route.

Figure 1.4 The John Hopkins Glacier inside Glacier Bay National Park, as seen aboard the MS Zaandam. The weather was relatively calm, with isolated fog and mist. However, a low cloud ceiling is evident. (Photo: M. Pirhalla, 2008)

Figure 1.5 Images of emission plumes from cruise ships trapped under inversions in Glacier Bay. Due to low level inversions and weak winds, exhaust smoke does not readily escape or diffuse. It remains stationary, just above the inversion level. The particles begin to swell since the air tends to have high relative humidly values. The haze particles become visible, which reduces overall visibility (Photos courtesy of Scott Gende, 2013, NPS).

The unique, steep-walled topography of Glacier Bay provides favorable conditions for temperature inversions to form during the summer (Mölders et al. 2013), particularly due to cold air drainage and radiative cooling. The stable conditions associated with inversions trap pollution (Mölders and Kramm 2010) and provide a suitable environment for haze formation. During Alaska summers, solar insolation is high in the Glacier Bay region (up to about 500 W m^{-2}). However, at such high latitudes (about 59°N), the sun is relatively low in the sky and never directly overhead. Thus, an inversion level may rise during high insolation and strengthen as insolation drops during nighttime hours. Mountains may inhibit and/or shorten the time of direct insolation. With the absence of moderate winds or storm systems to stir stagnant air, inversions may persist for several days. The existence of inversions and its persistence are important problems to study, as ship pollution may become trapped under inversions for a period of hours to days until the air is recirculated (Zhao et al. 2013). The trapped pollution leads to unsightly

haze and reduced visibility (Fig. 1.5), a stark contrast to what visitors expect to see in such a remote place. With the absence of in-situ measurements in Glacier Bay, additional means are necessary to understand such complex physical processes. Thus, we turn to numerical modeling as the tool to examine these problems.

1.2 Inversions

Air temperature typically decreases with altitude, following more or less an average environmental lapse rate of 6.5 K km^{-1}. However, in some situations, temperatures increase with height and such events are called atmospheric temperature inversions (hereafter simply called "inversions"). They often develop under clear skies and anticyclonic conditions (Shulski and Wendler 2007). High latitude regions notoriously experience high frequencies of temperature inversions due to the net loss of solar radiation that cools the surface level to a lower temperature than air above it (Bourne et al. 2010). Inversions have been known in the scientific community for decades. According to Serreze and Barry (2005), Brooks (1931) was the first to quantitatively demonstrate the frequency of inversions using kite ascents in Siberia. More detailed evidence of the vertical structure of inversions was published by Sverdrup (1933) during the *Maud* Expedition in the Arctic Ocean. Wexler (1936) was the first to propose mechanisms behind many high latitude inversions, namely their formation due to radiation loss.

Biello (1966) analyzed inversion characteristics, such as frequency, thickness, and strength in Fairbanks, Alaska, which is home to some of the strongest winter inversions upwards of 20 K (100m)$^{-1}$ (Wendler and Nicpon 1975). A study by Serreze et al. (1992) proposed high latitude inversions were due to more complex factors than just radiative cooling. In particular, a combination of warm air advection, season, snow cover, subsidence, and topography affect the frequency and strength of inversions (Serreze et al. 1992). Furthermore, Kankanala (2007) and Bourne (2008) showed that inversions are more likely to set up under clear skies, as cloudy conditions permit downwelling longwave terrestrial radiation that warms the surface layer.

Low-level inversions, regardless of strength, are typically present in almost all winter radiosonde ascents in Interior Alaska (Wendler 1975; Tran and Mölders 2011). The usual winter Arctic surface inversion is shallow, starting around 30-80 m above the surface (Serreze and Barry 2005). While their frequency decreases in the summer, Serreze and Barry (2005) have

found that high latitude inversions are still present in the summer, albeit weaker and slightly elevated around 200-400 m.

There are roughly two main categories of inversions that form in a slightly different manner: surface based inversions (SBIs) and elevated inversions (EIs). SBIs develop during stagnant synoptic conditions when air immediately above the surface of the Earth is cooled by infrared radiation (IR) loss (Garratt and Brost 1981). A SBI is regulated by several factors such as local flows and development of surface winds, absences of shear stress turbulence, clouds, and the local energy balance between net radiation and downwelling IR (Wendler and Jayaweera 1972; Wendler and Nicpon 1975; Serreze and Barry 2005). During SBIs, the atmosphere is stable, meaning there is no exchange between the atmospheric boundary layer (ABL) and the free atmosphere above. Stratification of the atmosphere can occur by warm air advection, potentially by a weather front at upper levels, where relatively warmer air overrides relatively colder air closer to the surface.

Besides inversions formed by advection, radiation inversions (Fig. 1.7a) are the predominant type of SBIs, and as found in this thesis, are the most commonly seen inversions inside Glacier Bay (further discussion in Chapter 4). Radiation inversions often develop during nights with calm wind where warmer and less dense air above the surface does not readily mix (Ahrens 1985). A deficit of net radiation creates thermally stratified and stable conditions (Wendler 1975). On calm and clear nights, the ground surface is able to rapidly radiate energy to space, thus cooling the surface layer faster than the air above it. According to Hudson and Brandt (2005), a strong SBI develops in the lowest 50 m of the atmosphere during evening hours when there is net radiation loss, but begins to rise as the solar angle increases and surface temperature rises in the morning. Even though the sun is above the horizon for long hours during Alaska summers (over 18 hours during the solstice), its altitude is low in the sky and may be obscured at times by local topography.

Cold air drainage is an important concept governing SBIs in areas with complex topography, and tends to enhance radiation inversions (Shulski and Wendler 2007). During the evening hours, cold air is formed at elevated land surfaces. The cooler air has a greater density than air at the same height in the middle of a valley, leading drainage down mountain slopes and pooling at lower elevations (Fig. 1.6). In addition, land surfaces cool faster than water surfaces, as water has a higher heat capacity. These effects tend to form inversions in valleys, including

Glacier Bay. Cold air drainage has been studied in several places, namely by Sakiyama (1990) in Alberta, linking drainage flow inversions and their subsequent breakup due to thermodynamic processes.

Figure 1.6 Schematic of cold air drainage into a valley, forming a SBI. Image retrieved from: http://backyard.weatherbug.com/profiles/blogs/the-south-central-texas-216 on 11-5-2013.
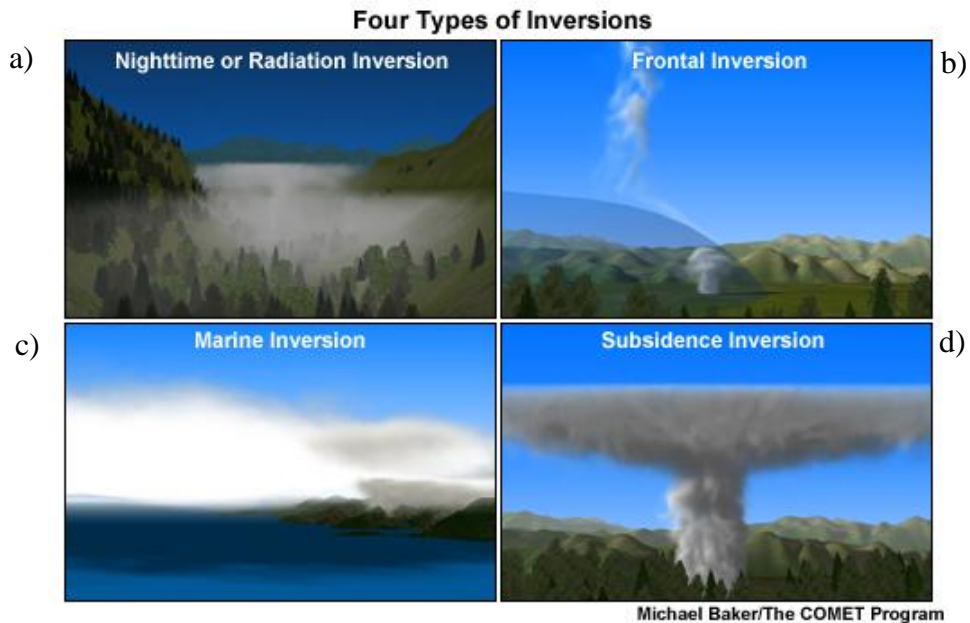
Fig 1.7 Examples of four types of inversions: a) radiation inversions, b) frontal inversions, c) marine inversions, and d) subsidence inversions. Retrieved 11-12-13 from the MetEd COMET Module: http://www.meted.ucar.edu/fire/s290/unit6/print_3.htm.

Depending on synoptic situations, EIs may develop further above the ground. EIs are discontinuities of air density between SBIs and the free troposphere, leading to inversions in the ABL flow (Mayfield 2011; Mayfield and Fochesatto 2013). Such types of inversions can be sub-classified as frontal inversions, subsidence inversions, and marine inversions.

Frontal inversions (Fig. 1.7b) are mainly due to warm air advection, and occur when warm air flows through elevated ridges over stagnant ABL flow further below it (Busch et al. 1982), or as warm air flows over water with a relatively cooler surface (Csanady 1974). These inversions are particularly important during sleet or freezing rain events.

Subsidence inversions (Fig. 1.7d) form due to a layer of stable, sinking air that warms by adiabatic compression, forming an inversion "lid" (Ahrens 1985). As the layer sinks and compresses, the upper portion warms at the dry adiabatic lapse rate of 9.8 K km^{-1}, capping off the cooler and denser air below it. When a subsidence inversion occurs close to the ground, pollutants from any anthropogenic sources are unable to escape, leading to episodes of poor air quality (Morgan and Bornstein 1977). This formation process is especially the case in Los Angeles, where subsidence inversions occur between 85-95% of the year, resulting in unhealthy amounts of pollution from aerosols, CO_2 and NO_x (Jacobson 2002). As the afternoon progresses, warming of the ground surface weakens the subsidence inversion, causing instability and the potential for the inversion to break. Inversions in Los Angeles are classified as trade-wind large-scale subsidence induced inversions (Neiburger et al. 1961).

Also related to subsidence inversions (Fig. 1.7c), maritime inversions may develop near coastal areas. The sun's radiation heats land surfaces quicker than the ocean, leading to pressure differences and a subsequent sea breeze circulation. When cool air moves inland during a sea breeze, warm inland air is forced over it (since it is less dense), creating the maritime inversion layer (Jacobson 2002).

1.3 Prior Modeling Studies

It is well known that inversions and stable air play a crucial role on air quality (Bowling 1986; Jacobson 2002; Mölders and Kramm 2010). As demonstrated in Bridgman et al. (1989), air quality below inversions is largely determined by local point sources rather than pollutants transported from far distances. When the atmosphere is unstable, convection and wind permits pollutants to become diffused over great expanses. However, with stable air commonly

associated with inversions, pollutants are trapped and the air does not readily recirculate. Thus, inversions can cause severe pollution problems, especially in Fairbanks during the winter, where concentrations of $PM_{2.5}$ (particulate matter with diameter less than 2.5 μm) often exceed the 24 hour average National Ambient Air Quality Standard (NAAQS) of 35 μg m^{-3} (Tran and Mölders 2011). The city has been designated a non-attainment area, meaning that the city must take measures in pollution reduction to improve air quality conditions.

Air quality and inversions in high latitude regions have been documented well by Wendler and Jayaweera (1972), Wendler (1975), Bowling (1986), and Tran and Mölders (2011). However, inversion modeling related to air quality is an area of research only touched upon in the atmospheric science community. Bourne (2008) used model simulations of the PSU/NCAR Mesoscale Model (MM5; Grell et al. 1995) downscaled from NCEP reanalysis data for Fairbanks. It was found that the model was able to capture inversions, but tended to overestimate overall vertical temperature profiles compared to the actual radiosondes. This was especially apparent in the lowest 100 m. Using the MM5 downscaled from Community Climate System Model (CCSM3; Collins et al. 2006), simulations overestimated inversion frequency, implying general circulation models (GCMs) have trouble resolving vertical structures of inversions, as opposed to dynamically downscaled simulations (Bourne 2008). Boé et al. (2009) and Pavelsky et al. (2011) also found that inversion strengths are poorly represented in GCMs, especially in high latitudes where the models strongly overestimate temperature profiles.

The use of a mesoscale model, where resolution is typically greater than in a GCM, may improve results when modeling complex processes, including inversions. Kukkonen et al. (2005) determined that the temporal evolution of inversions and stability were the key processes for predicting air pollution events in Helsinki, London, Milan, and Oslo. Basing her work after Kukkonen et al., Milford et al. (2008) used a 2 km resolution MM5 model run to predict air pollution episodes on the Canary Islands. The model was proven effective for predicting pollution episodes up to 108 hours ahead of time when initialized with the European Center for Medium Range Weather Forecasting (ECMWF) reanalysis data. It was especially helpful forecasting weather over complex topography, where mountains divert air flow, stagnating air and forming inversions over Santa Cruz de Tenerife (Milford et al. 2008). Note that over the Canary Islands, inversions are due to subsidence.

Mölders and Kramm (2010) used the Weather Research and Forecasting Model (WRF; Skamarock et al. 2008) in Interior Alaska to analyze its performance on winter inversions using multiple combinations of parameterization packages. Simulated inversions varied based on physical parameterizations used, but the authors concluded all simulations had difficulties estimating the full strength of inversions. The radiation scheme of the Community Atmosphere Model (CAM3; Collins et al. 2004) combined with the Rapid Update Cycle (RUC; Smirnova et al. 1997; 2000) land-surface model along with the Medium Range Forecast model surface layer captured inversions the best out of all tested schemes (Mölders and Kramm 2010).

WRF's performance has been widely tested in the scientific community since its debut in the late 1990s, and has proven to work effectively through analytical solutions, observations, results from the MM5, the NCEP eta-model, and reanalysis data. Since WRF is fairly flexible to various input characteristics, it has been tested using different configurations and parameterizations, such as in studies by: Etherton and Santos (2008); Mölders and Kramm (2010); Ruiz et al. (2010). WRF has shown success in numerical weather prediction, by accurately forecasting mesoscale convective systems over the Central United States (Done et al. 2004), as well as in simulations of convective storms (Klemp and Skamarock 2004). In addition, PaiMazumder et al. (2012) evaluated WRF over Siberia and found difficulties in predicting the pressure gradient and strength of winter high pressure systems.

Research in numerical modeling using WRF has gained popularity now that computational power increased exponentially since the Millennium. WRF is particularly popular, as it freely available, highly flexible, thoroughly used with a large support group, and efficient on multiple computing platforms (Skamarock et al. 2008).

The WRF model, coupled with a chemistry package (WRF/Chem; Grell et al. 2005; Peckham et al. 2011), has been particularly useful in understanding PM concentrations and transfer. Korotkova (2005) used WRF/Chem to simulate the transport of $PM_{2.5}$ over Iowa, which satisfactorily agreed with observational data's movement and mixing. Michael et al. (2013) also found that WRF/Chem was able to capture many important PM features over the Indian subcontinent, and was a useful tool at predicting regional atmospheric compositions. Hewson et al. (2013) explored aerosol effects on rainfall in Brisbane, Australia through the use of WRF/Chem, but instead selected individual stratiform and cumuliform precipitation events rather than using coarse reanalysis data sets. Their results showed that anthropogenic aerosols

were associated with less intense stratiform rain events, but more intense cumuliform systems downwind of an emission source.

Only a handful of WRF and WRF/Chem evaluations exist in Alaska and high-latitude regions. Some of the studies of particular interest are Brown (2008), Hines and Bromwich (2008), Mölders (2008), Porter (2009), Mölders et al. (2011; 2012), and Tran and Mölders (2012). Hines and Bromwich (2008) showed that the polar version of WRF produced skill that was on par with the Polar MM5, and improved surface-energy flux prediction in the summer. Mölders et al. (2011) found that WRF/Chem had trouble estimating $PM_{2.5}$ concentrations in Fairbanks when there were high errors in temperature, especially when it was about 5-10 K too warm. A subsequent study found that WRF/Chem was able to more accurately forecast $PM_{2.5}$ concentrations between 15-50 μg m^{-3}, but had trouble capturing extremes (Mölders et al. 2012).

Other WRF/Chem studies in Alaska concentrated on PM from naturally induced phenomenon, such as wildfires and volcanic eruptions. Stuefer et al. (2009) used WRF/Chem to forecast wildfire smoke emissions in Alaska. Another study by Grell et al. (2011) applied a plume rise algorithm for wildfires into WRF/Chem, and showed how aerosol interaction with solar radiation led to significant modifications of vertical temperature profiles. The study also showed how wildfire smoke PM had strong impacts on cloud microphysics and CCNs. Brown (2008) and Yarker et al. (2010) examined the local forcing of the 2006 Augustine volcano eruption on regional weather conditions with WRF, concluding that the volcano led to increased cloud cover and surface temperature due to ejected particles.

1.4 Ship Emission Studies

Since the discovery of ship trails on satellite imagery in the mid 1960's (Conover 1966), it became evident that emissions from cruise ships should be studied, particularly since emissions are modestly regulated and cruise ships sail to remote, pristine areas. It is estimated that between 0.9 and 1.7 million tons of PM are released worldwide from global shipping, with most of the pollution occurring within 400 km from land (Endresen et al. 2003; Eyring et al. 2005). Porter (2009) and Mölders et al. (2010) used WRF/Chem to investigate ship-emission impacts on atmospheric compositions in remote Southwest Alaska. The study showed that ship emissions cause significant increases in NO_x, SO_2, and PM in the air, thereby reducing visibility as far as

100 km inland. Ship emissions also lead to increased deposition of the aforementioned pollutants by gravitational settling.

According to a case study in Southern California by Vutukuru and Dabdub (2008), the composition of $PM_{2.5}$ and PM_{10} (particulate matter with diameter less than 10 μm) is dominated by sulfates due to high sulfur fuel. As a result, nearly 50% of PM_{10} direct emissions are assumed to be sulfate particles. Using low sulfur fuel may result in a reduction of SO_2 and PM_{10} by 87% and 74%, respectively, which has been simulated using WRF/Chem in Glacier Bay (Mölders et al. 2013). High concentrations of PM are particularly evident in port cities, where levels of pollution are already elevated from other anthropogenic sources. While in port, ships continue to release pollutants while berthing, and may idle to run backup generators.

Moldanová et al. (2009) analyzed PM_{10} emissions from the exhaust of diesel burning ship engines using heavy fuel oil. They concluded that the mass-size distribution of emitted particles was 0.5 to 7.0 μm on average, resulting in the domination of organic carbon and sulfate, especially upon cooling of the plume. A study by Murphy et al. (2009) determined that organic carbon to sulfate mass ratio of aerosols emitted by the exhaust from modern container ships remained constant for at least an hour upon dilution into the marine boundary layer. Near Venice, Italy, Contini et al. (2011) showed $PM_{2.5}$ emissions from ships contributed to 10% of polycyclic aromatic hydrocarbons (PAHs) and 1-8% for PM_{10}.

1.5 Other Studies in Glacier Bay

A considerable amount of research has been done inside Glacier Bay, however, studies regarding atmospheric sciences are lacking. Most research involves marine projects with aquatic plants and animals, oceanography and mapping, and wilderness and backcountry management. Dr. Daniel Lawson of the Cold Regions Research and Engineering Laboratory in Hanover, NH, has carried out extensive studies regarding climate monitoring, glacier dynamics and hydrology, dendrochronology, and attempts in understanding the paleoclimate from the last 10,000 years inside Glacier Bay National Park (Lawson et al. 2011). Studies conclude that during the Little Ice Age, Glacier Bay was covered in ice as recently as AD 1770 (Motyka et al. 2003), and melting to present day levels contributed to as much as 8 mm of global sea level rise (Larsen et al. 2005).

Concerns about air quality in Glacier Bay is not new. Park Service officials first started to realize air quality and visibility were deteriorating in Glacier Bay's upper fjords during the winter of 1975-76, as stack emissions from cruise ships led to extensive periods of haze, especially during calm and clear weather (Benson et al. 1978). A reconnaissance study to assess the pollution potential was carried out during the summers of 1976 and 1977, where instruments were placed in Goose Cove in the upper reaches of Muir Inlet. It was found that temperature inversions existed on approximately one-third of all days (from June 13-July 21), lasting at least part of the day, and were most common in the early morning (3:00-8:30 am) when skies were clear and radiation balance was negative (Benson et al. 1978). Thus, the authors concluded Glacier Bay has a low tolerance to pollution due to minimal mixing of air once pollutants are injected by ship exhaust. In addition, exhaust gases emitted from fuel combustion have the potential to exceed the original fuel's liquid mass. For example, when one pound of combusted gasoline combines with the surrounding air, 3.1 pounds of CO_2, 1.4 pounds of water vapor, and small amounts of CO are released as exhaust gases during the combustion process (Benson and Rizzo 1980).

According to the U.S. Forest Service (2012), lichen growth in Glacier Bay can be an indicator of air quality. Lichens are specialized fungi that feed on algae, and have limited tolerance with air pollution (U.S. Forest Service 2011). A total of 508 documented varieties of lichen and allied fungal species thrive in Southeast Alaska, due to a rich combination of isolated temperate rain forests, wet oceanic climates, and (typically) excellent air quality (Geiser et al. 1998). Lichens are particularly sensitive to SO_2 and acid rain deposition (Geiser and Dillman 2012). The National Park Service currently has monitoring stations in four popular cruise ship sightseeing locations, including Glacier Bay (Geiser and Dillman 2012). The increase in ship traffic over the past ten years shows a positive correlation in nitrogen, sulfur, lead, and vanadium in lichen in the vicinity of Sitka (U.S. Forest Service 2012).

1.6 Goal of this Thesis

The goal of this thesis is to understand temperature inversions, their formation mechanisms in Glacier Bay, and their impacts on PM distribution and concentrations from cruise-ship emissions. This thesis will analyze when inversions develop, what time of the tourist season they tend to favor, which areas in Glacier Bay have the most frequent inversions, how

strong they become, their typical altitude proximity, and their impact on PM during the 2008 tourist season. With the absence of physical measurements of the vertical temperature and PM profiles in Glacier Bay, WRF/Chem has been used to understand the changes in vertical temperature and PM concentration. In order to quantify how effective WRF/Chem is at reproducing the meteorology during the summer of 2008, model results were compared against a large database of surface and upper air observational data.

Inversion development is highly dependent on regional and local meteorology. Calm, clear weather is necessary, otherwise turbulent motion can cause the mixing of layers and break an inversion. Thus, I hypothesize that the interactions between large-scale synoptic meteorology and mesoscale processes strongly determine the fate of pollutants from ship emissions in Glacier Bay. In this case, mesoscale processes include inversions. Alternatively, the *null* hypothesis can be stated that these same interactions do not determine the fate of pollutants from ship emissions in Glacier Bay. A majority of the inversions are expected to be the result of radiative cooling and due to stagnant flows. PM_{10} concentrations are predicted to rise and stay elevated if a ship enters Glacier Bay with an inversion present. I also examine whether inversions lead to various effects regarding pollutant distribution in Glacier Bay.

This task was tackled through the analysis of WRF/Chem data and statistical software. In the following chapter, I will outline the numerical model setup and parameterizations of the WRF/Chem data I analyzed, discuss sources of observed meteorological data, and introduce statistical skill scores used in the model validation. Chapter 3 will discuss results and skill scores from the model evaluation. Chapter 4 will provide a discussion on the inversions in Glacier Bay and their relation to PM. Finally, I will draw conclusions and wrap up the thesis in the final chapter.

Understanding the frequency and processes behind inversions can provide guidance for future regulations inside Glacier Bay. This is especially noteworthy concerning the number of ships that may enter the bay per day and/or season, the amount of emissions they are allowed to release, and where they can go inside Glacier Bay. Despite ships emitting pollution, Glacier Bay is still an extremely pristine region (Mölders et al. 2013). However, ship-emission impacts from previous ships are not visually appealing, and are unexpected by visitors vacationing through such a remote area.

Chapter 2 Experimental Design and Methodology

The following section explains the methodology used in this thesis. It outlines the use, parameterizations, and overall setup of the Weather Research and Forecasting Model (WRF; Skamarock et al. 2008), inline coupled with a chemistry transport package (WRF/Chem; Grell et al. 2005; Peckham et al. 2011) in its Alaska adapted form (Mölders et. al. 2010; 2011). Descriptions of the model domain, simulations, and emission data are also outlined. In addition, details of validating the model are described, including sources of meteorological data, as well as the calculation of skill scores.

2.1 Model Description

WRF/Chem is a non-hydrostatic, Eulerian atmospheric mesoscale model. It incorporates two dynamics solvers: the Advanced Research WRF (ARW) and the non-hydrostatic mesoscale model (NMM), meaning it solves the full vertical momentum and continuity equations (Jacobson 2005; Skamarock et al. 2008). It has proven to be extremely valuable in providing researchers, graduate students, meteorologists, and air quality managers a better understanding of mesoscale processes and how to effectively adjust operational forecasts. The fully coupled chemistry package accounts for trace-gas cycles from emission sources, through chemical reactions to pollutant removal from the atmosphere.

Building the WRF/Chem code has been made possible by the collaboration of several agencies. Along with numerous university scientists and national labs, the bulk of the WRF model has been developed by the National Center for Atmospheric Research's (NCAR) Mesoscale and Microscale Meteorology (MMM) division. In addition, there has been collaboration between the National Oceanic and Atmospheric Administration (NOAA), Earth System Research Laboratory (ESRL), various university groups, and several other organizations, including other sectors of the United States Government (Skamarock et al. 2008; 2011).

2.1.1 Terrain-Following Vertical Coordinate System

This study used WRF/Chem version 3.3 model data. WRF/Chem implements a staggered Arakawa C grid (Arakawa and Lamb 1977) (Fig. 2.2) in the setup described in Mölders et al. (2013) and contains a terrain following vertical coordinate system (Fig. 2.3). A staggered grid

increases resolution by a factor of two and minimizes the effects of lateral boundaries on calculation of vertical velocity (Pielke 2001). Operator splitting is integrated using 2nd or 3rd order Runge Kutta schemes with the ability for even smaller modes for acoustic and gravity waves (Skamarock et al. 2008).

The WRF/Chem terrain-following vertical coordinate system results in a variation of heights across the domain, which is based on each grid cell's mean terrain height. The model setup used by Mölders et al. (2013) for the simulation analyzed in this thesis contains 28 full vertical eta levels (27 half levels), each with increasing thicknesses with higher elevation. At grid cells starting at sea level, the average top of the first eta level was approximately 64 m. The height of the second level is approximately 150 m, resulting in a thickness of about 87 m. The first 2 km (10 eta levels) are the most useful in this study, as modeled temperature inversions did not occur above that height, with the exception of the inversion at the tropopause.
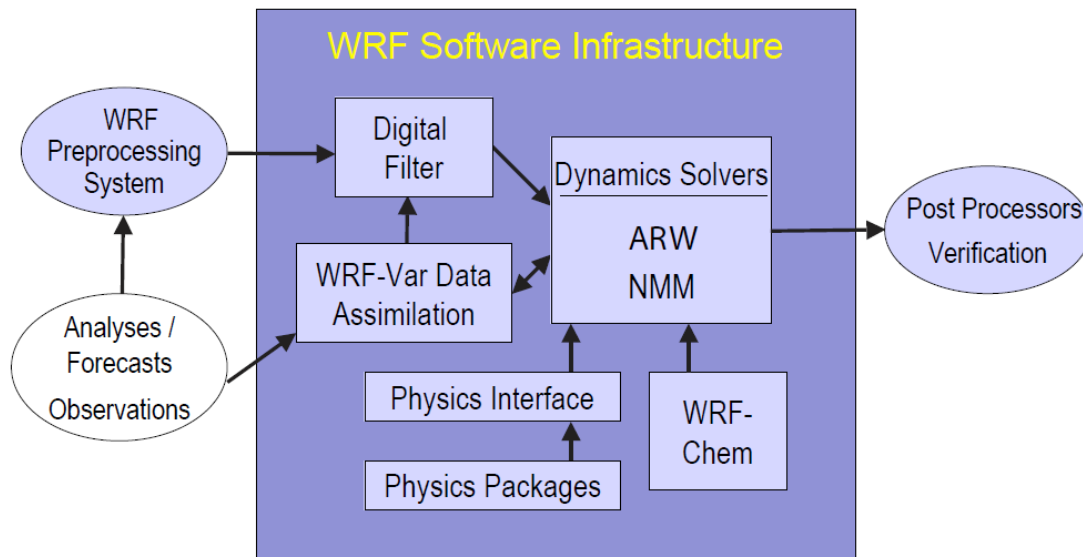
Figure 2.1 Component flowchart of the WRF model (from Skamarock et al. 2008).

(C)
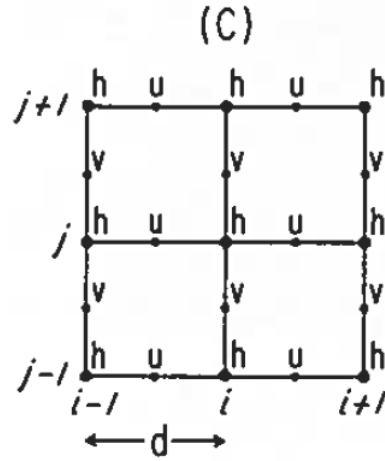
Figure 2.2 Arakawa C Grid (Arakawa and Lamb 1977) where u and v are the geostrophic wind components, h is an observational variable, i and j are the indices of the grid points in the x and y direction, and d is the grid cell size (grid increment).

P_{ht} = constant

η

P_{hs}
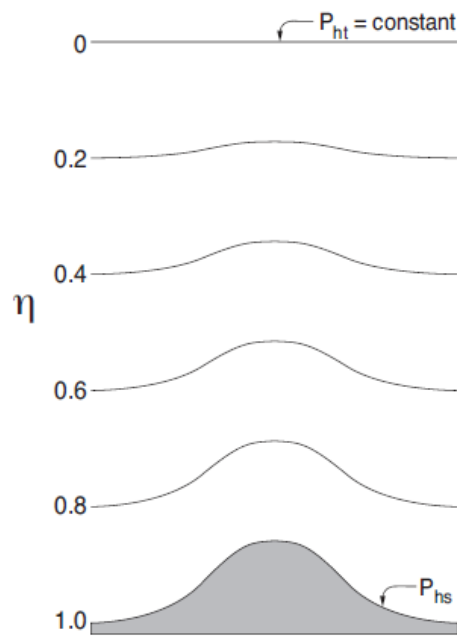
Figure 2.3 Schematic view of the terrain following, vertical coordianate system (from Skamarock et al. 2008).

19

The basic equations used to formulate the terrain-following hydrostatic-pressure vertical coordinate system of WRF/Chem, as depicted in Fig. 2.3, were proposed by Laprise (1992), where:

$$\eta = \frac{p_h - p_{ht}}{p_{hs} - p_{ht}} \qquad (2.1)$$

p_h is the hydrostatic component of pressure and p_{hs} and p_{ht} are pressure values at the surface and top boundaries, respectively (Laprise 1992).

Table 2.1 Average heights and thicknesses of each WRF/Chem level below 4 km at a grid point at sea level (0 m). Thicknesses of each level increase with increasing height.

WRF/Chem Level	Approximate Height of Level (m)	Thickness of Level (m)
1	63	63
2	150	87
3	261	111
4	399	138
5	575	176
6	790	215
7	1091	301
8	1470	379
9	1863	393
10	2273	410
11	2871	598
12	3663	792
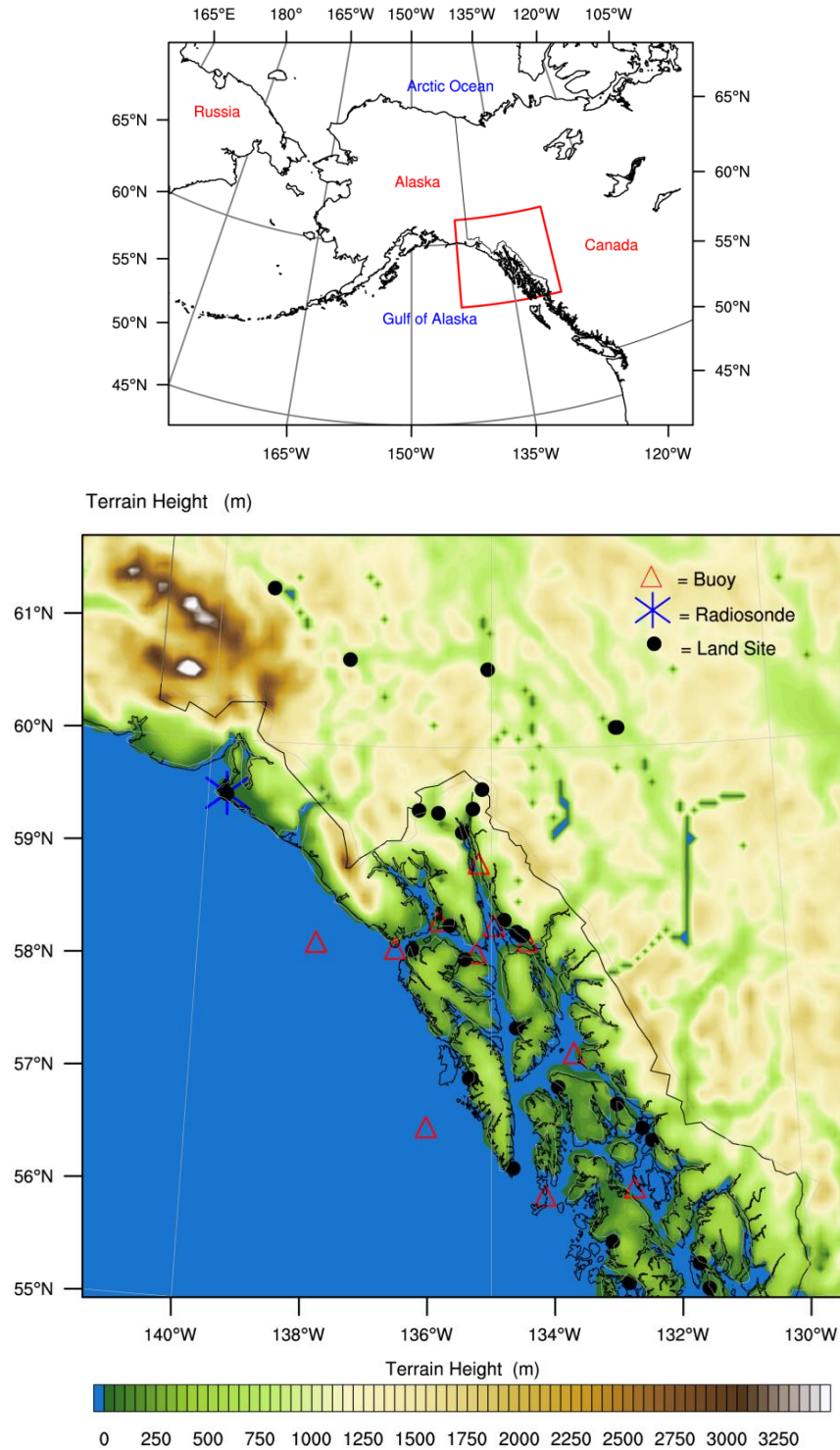
Figure 2.4 WRF/Chem model domain. The top panel displays the State of Alaska and surrounding geography with the domain of interest indicated by a red polygon. The bottom panel shows the model domain of interest, shaded by terrain height and overlaid with locations of surface meteorological sites. Buoys are denoted as red triangles, land-based sites (NCDC and RWIS) with black circles, and the radiosonde with a blue asterisk. Note that the sites are skewed to settlements and easily accessible regions.

2.1.2 Model Domain

The model domain consisted of 120 x 120 grid cells with a 7 km grid increment. However, after running the simulations, the domain was trimmed by five grid cells (35 km) on all four sides to avoid boundary related errors in the analysis. Thus, the trimmed domain used in analyses consists of 110 x 110 grid cells, and is called the domain of interest hereafter. This results in a 592,900 km^2 domain of interest (Fig. 2.4) located on the panhandle of Southeast Alaska, centered over Glacier Bay. The domain encompasses the entire Alaska Panhandle, including the "larger" cities and towns of Juneau (pop. 32,164), Ketchikan (pop. 8,050), Sitka (pop. 8,952), Petersburg (pop. 3,030), Haines (pop. 2,508), and Yakutat (pop. 662). Most of the southwest portion of the domain is occupied by the Gulf of Alaska, while the northeast region encompasses northwest British Columbia and extreme southwest Yukon, Canada, including the city of Whitehorse, YT (pop. 23,276).

2.1.3 Model Initialization

Initial and boundary conditions for meteorological, soil, and snow data was obtained from the National Centers for Environmental Prediction's (NCEP) 6-hour global final analysis data, at 1° x 1° resolution. To initialize the chemical fields and to provide lateral boundary conditions in the simulation, the model also used idealized mean background chemical profiles modified for Alaska (Mölders et al. 2013). The typical values of acetylene, CH$_3$CHO, CH$_3$OOH, CO, ethane, etc. were determined through vertical profiles common in southeast Alaska.

The top boundary condition of the model was set to 100 hPa. While 100 hPa is very high in the atmosphere (at least 16,000 m), and well past the height of the tropopause of approximately 10 km, it is with good programming skill to set the upper boundary conditions far away from the area of interest; this procedure aids in the reduction of boundary related errors (Jacobson 2005). However, it is not necessary to set it to 0 hPa, as there are deep layers of thermodynamic stratification present in the stratosphere (Pielke 2001). This same mentality was used for the horizontal boundary conditions, where ten grid cells at the lateral boundaries were discarded (five on each side). Thus, the trimmed domain of interest results in the positioning of Glacier Bay directly in the center of the domain to avoid boundary problems, with at least 290 km in all directions from the lateral boundaries.

2.2 Physics Packages

The WRF/Chem model can be applied to many different spatial scales throughout all corners of the world, and thus comes with a variety of physical parameterizations to account for processes that the model cannot resolve. The following sections describe the physical packages chosen by Mölders et al. (2013) for the simulations analyzed in this thesis.

2.2.1 Cloud Microphysics

The cloud microphysics option selected was the WRF Single-Moment 5-class scheme (WSM5), as described by Hong et al. (2004) and Hong and Lim (2006). WSM5 treats water vapor, snow, rain, cloud ice, and cloud water separately compared to the WRF Single-Moment 3-class, which only assumes water vapor, cloud water/ice, and rain/snow. WSM5 accounts for ice and mixed-phase cloud processes, and allows for the co-existence of both super-cooled water and ice, and hence for the gradual melting of snow at temperatures above freezing (Skamarock et al. 2008). The three class microphysics option proves to be accurate enough to resolve mesoscale features on grid cells as large as 25 km (Hong et al. 2004). However, with recent state-of-the art computational power and the use of smaller grid increments, modifications have led to a five class scheme. Further updates in computational resources have allowed for the addition of a sixth class. The addition of graupel in the WRF Single-Moment 6-class scheme (WSM6) is now available for use. WSM5 and WSM6 are particularly useful in simulating precipitation and its temporal evolution in high resolution models (Hong and Lim 2006). Single-moment indicates that only the mixing ratio is considered, while two-moment uses the mixing ratio as well as number of droplets. The WSM5 scheme was chosen as it allows feedbacks with radiation and chemistry packages (Peckham et al. 2011).

2.2.2 Cumulus Parameterization

Convective clouds were parameterized using the Grell and Dévényi (2002) cumulus ensemble scheme. Cumulus parameterization is necessary to resolve sub-grid-scale effects due to convection and low level clouds at the 7 km grid increment, as used here. Cumulus clouds are complicated to resolve since they are typically on the order of 1 km in the horizontal scale. The cumulus parameterization is essential in representing vertical fluxes due to updrafts and downdrafts. Similar to the land-surface model (LSM) described in section 2.2.7, the cumulus

parameterization only considers the vertical column at a grid cell, but only where there is moisture present (Skamarock et al. 2008). The modified version of the Grell and Dévényi (2002) 3-dimensional scheme uses multiple cumulus clouds in each grid cell and averages the values. It considers several closure methods, particularly dynamic closure that controls convective available potential energy (CAPE), vorticity, and moisture convergence of 144 sub-grid-scale ensemble members (Skamarock et al. 2008).

2.2.3 Shortwave Radiation

Incoming shortwave radiation is parameterized with the Goddard scheme, which was implemented by Chou and Suarez (1994) and uses a two-stream, 11 spectral band approach. Eight bands are dedicated to ultraviolet (UV) and photosynthetically active radiation, while the remaining three are for infrared solar radiation. The spectral bands consider diffuse (semi-direct) and direct incoming solar radiation, which is both scattered and reflected. The parameterization takes into account cloud effects and ozone profiles with respect to seasons and locations on the planet (e.g. tropics, mid-latitudes, polar), and uses WRF/Chem simulated profiles when cloud radiation is considered in the run (Skamarock et al. 2008).

Both the shortwave and longwave schemes use a correlated-k distribution approach, which accurately determines radiative transfer while reducing computational time (Mlawer et al. 1997). It is based on the concept that spectral transmittance is independent of the absorption coefficient (k) for that spectral interval, as gathered from predetermined values on lookup tables. The technique calculates fluxes and cooling rates for inhomogeneous atmospheres (Mlawer et al. 1997). Additionally, land-use type is used to determine surface albedo in the visible (VIS) and infrared (IR) spectral bands.

2.2.4 Longwave Radiation

The Rapid Radiative Transfer Model (RRTM; Mlawer et al. 1997) scheme was applied for the longwave radiation parameterization. Originally used for the Fifth-Generation Penn State/NCAR Mesoscale Model (MM5; Grell et al. 1995), the RRTM was adapted by Mlawer et al. (1997) and is a spectral band scheme that uses predefined values on lookup tables to accurately represent outgoing terrestrial radiation. It accounts for land-use type and surface

emissivity for processes due to water vapor, ozone, carbon dioxide, methane, nitrous oxide, and trace gases. It also accounts for cloud optical depths (Skamarock et al. 2008).

2.2.5 Surface Layer Physics

The surface layer scheme calculates frictional velocities in order to resolve surface heat and moisture fluxes created in the atmospheric boundary layer (ABL; Skamarock et al., 2008). The surface layer physics are parameterized using the eta surface layer scheme adapted from Janjić (1996; 2002). It is based on Monin and Obukov's (1954) similarity hypothesis, a universal length scale for exchange processes in the surface layer. Monin and Obukov's hypothesis for surface layer physics tends to become violated in regions with highly stable conditions (Mölders and Kramm 2010), such as Fairbanks. However, much of southeast Alaska is predisposed to maritime influences.
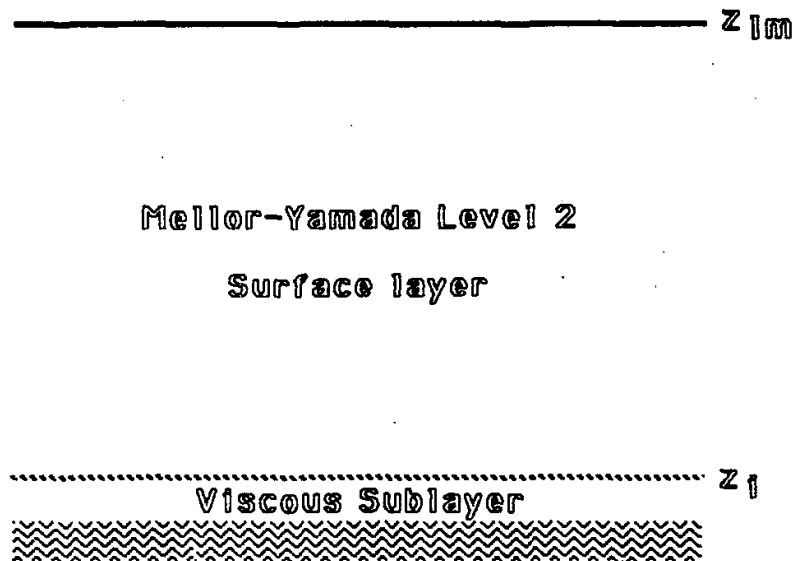
Figure 2.5 Schematic of the viscous sublayer over an ocean surface in the eta model. The dotted line indicates the depths of the viscous sublayer for momentum, heat, and moisture, while the top line is the height of the lowest model level (Janjić 1994).

The parameterization for a viscous sub-layer over water surfaces (Fig. 2.5) follows the eta coordinate model by Janjić (1994). Water surfaces contain two layers: a viscous sub-layer with vertical transport affected by molecular diffusion, and another layer affected by turbulence. Land-use type affects the degree of roughness length. Therefore, variable roughness Reynolds

25

numbers for temperature and humidity are accounted for according to Zilitinkevich (1995). The eta surface layer model is quite accurate when obtaining precipitation forecasts (Janjić 1994).

2.2.6 Atmospheric Boundary Layer Physics

The eta surface layer scheme must also be run in conjunction with the Mellor-Yamada-Janjić (MYJ; Mellor and Yamada 1982; Janjić 1994; 1996; 2002) atmospheric boundary layer (ABL) scheme. Collectively, the surface layer physics and ABL physics are referred to as the MYJ surface scheme. The MYJ scheme describes vertical mixing in the ABL and free troposphere and applies the level 2.5 turbulence closure model (Mellor and Yamada 1982) that considers a range of turbulent processes. Transport, buoyancy, and shear are resolved from equations of turbulent kinetic energy (TKE), and are typically initialized above the ABL so most TKE is dissipated after model spin up (Janjić 1994). The Smagorinsky first-order-closure option is used for the eddy coefficients in the horizontal direction. The eddy viscosity is determined from horizontal deformation (Skamarock et al. 2008). The setup considers vertical turbulent mixing as well as sub-grid-scale convective transport.
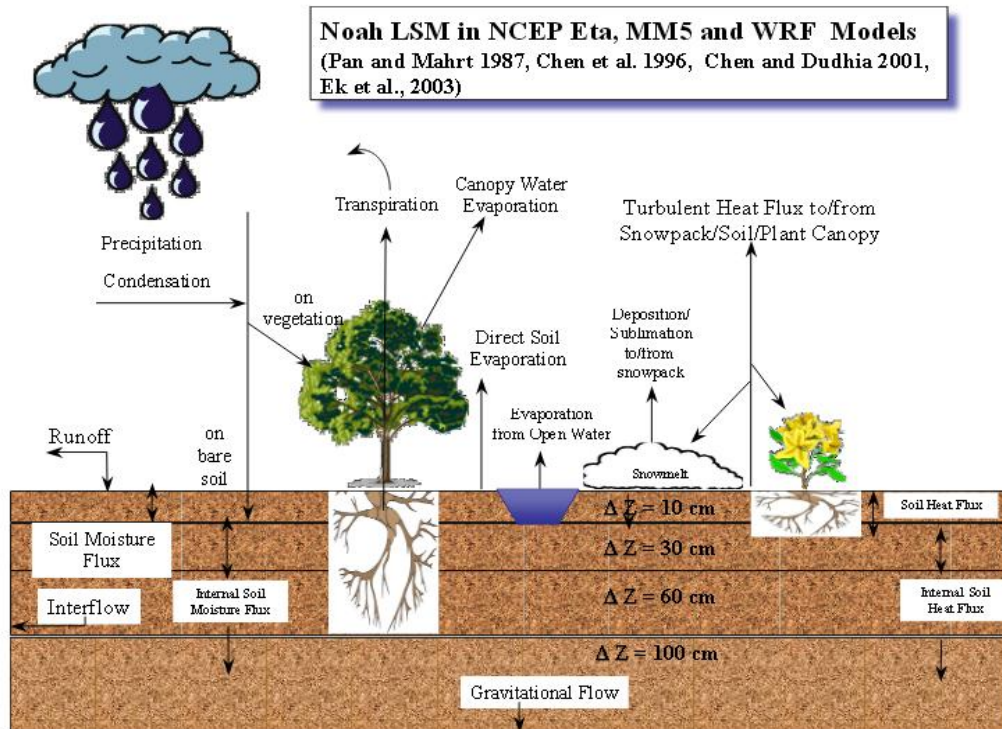
Figure 2.6 Schematic view of the Noah Land Surface Model for various processes involving heat and moisture fluxes, soil, vegetation, snow, and precipitation (Chen and Dudhia 2001).

2.2.7 Land Surface Processes

The land surface model (LSM) determines heat and moisture fluxes over land and water surfaces and is used to account for sub-gridscale fluxes. The fluxes are calculated by a combination of data from the land-use type, soil type, atmospheric information from the surface layer scheme, radiative forcing from the radiation scheme, as well as precipitation from the cloud microphysics and convective schemes. The LSM determines the lower boundary conditions for the WRF/Chem simulation. There are no lateral surface processes considered (e.g. interactions with adjacent grid cells), therefore each WRF grid point is considered an entirely separate one-dimensional column (Skamarock et al. 2008).

A modified version of the Noah LSM (Chen and Dudhia 2001) is used for this study (Fig. 2.6). The LSM considers one layer canopy and four layers for soil temperature and moisture calculations at depths of 0.1, 0.4, 1, and 2 m, respectfully. It predicts frozen ground, soil moisture, and soil heat fluxes using heat diffusion and Richards' moisture transfer equations. The model also considers vegetation, water uptake by roots, albedo, emissivity, soil drainage and runoff, fractional snow coverage, sensible and latent heat fluxes to the atmospheric boundary layer, as well as evapotranspiration. The Noah LSM was developed jointly by Oregon State University (OSU), NCEP, and NCAR, and is also implemented in the North American Mesoscale Model (NAM; Skamarock et al. 2008).

2.3 Chemistry Packages

This simulation with WRF is inline coupled with a chemistry package. In general, chemical packages can be inline ("online") or offline coupled. Inline coupling runs both the chemistry and meteorological data consistently, while offline runs one model, e.g. WRF, stores the data, and runs the chemistry transport model. The offline approach is applied by agencies despite that it is very storage intensive. Although some information is lost during the process (Mölders et al. 1994; Grell et al. 2005), offline calculation saves computational time when hundreds of different emission or sensitivity studies have to be run.

2.3.1 Gas-Phase Chemistry

This study uses the Regional Acid Deposition Model version 2 (RADM2) for the gas-phase chemistry mechanism, as developed by Stockwell et al. (1990). This widely used

mechanism predicts the concentrations of oxidants and air pollutants and the chemical reaction among them. The inorganic chemistry included in the RADM2 contains 14 stable species and 4 reactive intermediates. Furthermore, it also considers three abundant stable species of oxygen, nitrogen, and water. Volatile organic compounds (VOCs) are represented by 26 stable species and 16 short-lived intermediate peroxy radicals, as described by Middleton et al. (1990). Photolysis frequencies are calculated at each grid point for 21 photo-chemical reactions in accordance with Madronich (1987). The Goddard shortwave radiation scheme also considers radiative feedback with aerosols and chemistry (Chou and Suarez 1994).

2.3.2 Aerosols

In order to account for primary and secondary organic aerosols (SOA) in the atmosphere, this study uses the Modal Aerosol Dynamics Model for Europe (MADE; Ackermann et al. 1998) as well as Secondary Organic Aerosol Model (SORGAM; Schell et al. 2001). The packages are collectively known as the MADE/SORGAM aerosol package.

Primary organic aerosols (POA) are directly emitted by natural and anthropogenic sources while SOAs form in the atmosphere by gas-to-particle conversion. The MADE package is an updated version of Binkowski and Shankar's (1995) Regional Particulate Model and assigns sub-micron inorganic aerosols into two overlapping accumulation modes (approximately 0.01 and 0.07 μm diameter for Aitken and accumulation mode, respectively) (Ackermann et al. 1998). There is also no wet scavenging of aerosols or cloud chemistry in the simulation.

The organic aerosol chemistry in SORGAM assumes that SOA interaction forms a quasi-ideal solution (Schell et al. 2001). There is still some uncertainty in how SOAs form in the atmosphere. Model tests from Schell et al. (2001) indicate that biogenic and anthropogenic interacting SOA compounds significantly influence each other, and cannot be treated separately as they have an impact on total simulated SOA concentrations. Moreover, the MADE/SORGAM package considers sea-salt emissions, which is particularly useful in a partial maritime domain, such as Southeast Alaska (Fig. 2.4), with considerable effects from oceans.

2.3.3 Dry Deposition

Dry deposition of trace gases is calculated using Wesely's (1989) surface resistance parameterization with the modifications introduced for specific Alaska surfaces by Mölders et al.

(2011). This scheme is derived from land-surface resistance based on aerodynamic, sublayer, and surface resistances. The estimation of the velocity of dry deposition of atmospheric gases depends on the composition of the surfaces, such as land-use type, soil, and vegetation. Wesely's (1989) parameterization considers 24 land-use types and five seasonal categories for computing dry deposition. Instead of using simple lookup tables, this parameterization calculates a more advanced surface resistance value along upper and lower parts of vegetation canopies, as well as on ground or water surfaces (Wesely 1989). The modifications by Mölders et al. (2011) include modified plant parameters to represent Alaska vegetation, and Zhang et al.'s (2003) parameterization of deposition on snow surfaces.

2.3.4 Biogenic Emissions

Biogenic emissions for this study were calculated based on Guenther et al. (1993; 1994) and Simpson et al. (1995) for isoprenes, monoterpenes, and biogenic volatile organic compounds (BVOCs) from vegetation and nitrogen emissions from the soil. Forest isoprene emissions depend on temperature and the rate of photosynthesis based on solar radiation (Guenther et al. 1993) while monoterpenes and BVOCs depend solely on temperature. The algorithms used can calculate average isoprene emissions within 35%, and account for approximately 90% of the observed isoprene diurnal variability (Guenther et al. 1993). VOC emission rates are estimated from 49 types of United States tree genera (Guenther et al. 1994). No biomass burning is considered.

2.4 Simulations

Along with the parameterization schemes outlined above, WRF/Chem simulations began with analysis data from the 1° x 1° resolution NCEP 6-hour final analyses. Simulations ran for a period of 124 days from May 15 to September 15, 2008 centered at 58.5˚N, -135.5˚W. The output data was in an hourly format, resulting in 2976 hours of simulated meteorological and chemical data. This time frame was selected, as it not only is the peak tourist season in Southeast Alaska with the highest cruise-ship activity, but also covers the peak temperature period (Mölders et al. 2013).

As mentioned in section 2.1.3, idealized vertical profiles of background chemistry typical for Southeast Alaska were used to initialize chemical boundary conditions. In a sensitivity study,

Mölders et al. (2013) determined that increasing background concentrations by 10% produced negligible impacts. This is due to the fact that the background concentrations in Alaska are very low. Meteorology was initialized every five days in the simulations, but the chemical distributions at the end of each day were used as initial conditions for the following day (Mölders et al. 2013). In a broader scope outside this thesis, these simulations were used to model emissions as a function of cruise-ship speed for potential policy control by the National Park Service (NPS), and are published in the paper by Mölders et al. (2013). Four sets of simulations were produced, each pulling data from four separate emission inventories. In this thesis, however, discussion will solely focus on simulations using the original 2008 cruise-ship emissions.

2.5 Emissions

A bottom-up approach (Fig. 2.7) was used to establish an inventory of cruise-ship emissions present during the tourist season (Mölders et al. 2013). A bottom-up design pieces together elements that ultimately result in a more complex system. An Automated Information System (AIS), which stores global positioning system (GPS) locations of ships, cruise-ship names, and speeds, together with the ships' characteristics, was used to create the emission inventory. The AIS included number of engines, power, maximum speed, number of passengers, and fuel type used.
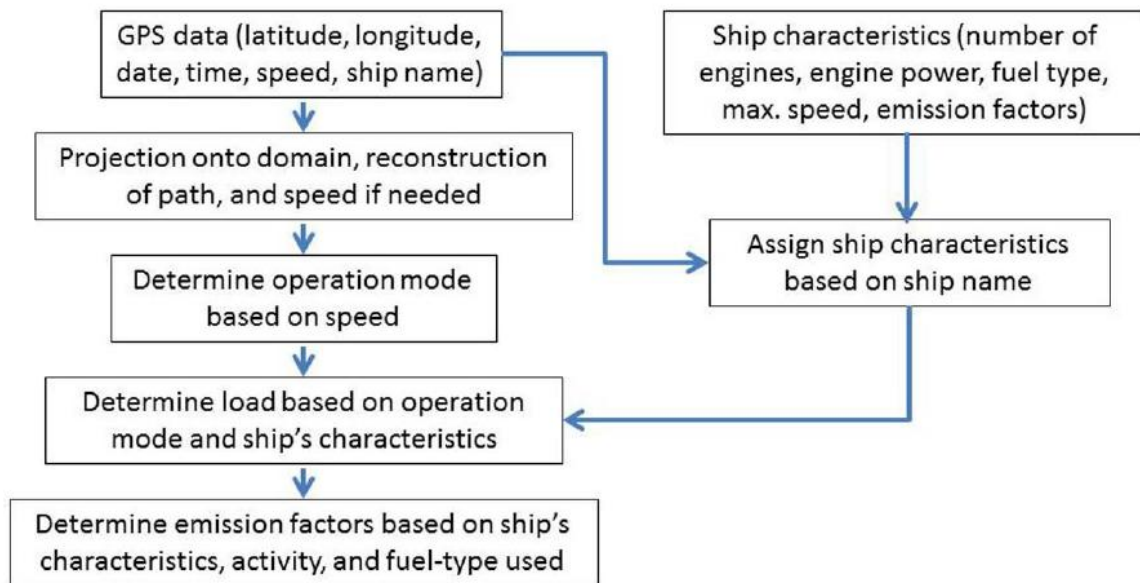
Figure 2.7 Schematic of the cruise ship emission inventory (from Mölders et al. 2013).

Depending on the speed, the operation mode (e.g. berthing, maneuvering, and cruising) was determined. Twenty-nine cruise ships sailed in Southeast Alaska during the 2008 tourist season. The engines aboard cruise ships ranged between 10,400-40,000 kW for main engines, and 8,000-17,700 kW for auxiliary engines. The berthing, maneuvering, and cruising auxiliary engine load was assumed 50%, 30%, and 60%, respectively, while the maximum cruising speed ranged between 20-24.5 knots (Mölders et al. 2013).

It is especially challenging to estimate a cruise ship's emission rate when it is maneuvering and berthing in port. A cruise ship's engine that fires from a cold start produces different levels of pollutants (when considering VOCs and PM), as opposed to one firing from a warm start (Mölders et al. 2013). In addition, speed is one of the primary concerns regarding emission rates, where faster speeds typically exhibit more emissions, except for maneuvering.

In 2010, the International Maritime Organization (IMO) declared all waters up to 200 miles from coastlines off North America as Emission Control Areas (ECAs), and large ships would have to comply by using low sulfur fuel by 2016. The main goal in the paper by Mölders et al. (2013) was to understand how variations of cruise-ship speed and the establishment of an ECA would impact emissions, visibility, and air quality in Glacier Bay.

Thus, four sets of simulations inside Glacier Bay were produced for Mölders et al.'s (2013) study. The first simulation considered the 2008 cruise-ship speeds and itineraries, and was purely based on AIS data on the twenty nine cruise ships (REF). For this thesis, the emissions and data of that simulation are used, if not mentioned otherwise. The average cruise-ship speed in Glacier Bay for REF was 16.7 knots.

The second and third simulations in Mölders et al. (2013) considered a change in speed inside Glacier Bay, as cruise-ship speeds are currently variable. Limiting the speed to 13 knots (S13) could alleviate collisions with humpback whales in Glacier Bay (Gende et al. 2011), but reduce glacier viewing time. Increasing speed to 20 knots (S20) allows further berthing time at glaciers, but demonstrates the potential for higher emission rates. The final simulation (ECA) estimates the reduction in emissions using cleaner burning fuel, as required by an ECA.

2.6 Sources of Data and Data Evaluation

In order to confirm how accurately the WRF/Chem simulations were able to capture what actually occurred, it is necessary to compare the data against meteorological and chemical

observations. With the presence of boundary and parameterization errors, models are not completely correct, but serve as beneficial research tools in understanding complex physical and chemical processes. Simulations that are not compared against observed data loose credibility and are open for speculation (Jacobson 2005). Therefore, our simulations were evaluated using data from numerous meteorological observation stations inside the domain. Their analyses methods are outlined below. Unfortunately, no chemical observation data were available. However, WRF/Chem has been shown to acceptably simulate the chemical fields in Alaska (Mölders et al. 2011; 2012).

2.6.1 Sources of Surface Based Meteorological Data

Hourly surface meteorological data was gathered from four different sources: The Western Regional Climate Center (WRCC[1]), NOAA's National Climatic Data Center (NCDC[2]), including airport, seaplane, and other land-based sites, the National Data Buoy Center (NDBC[3]), and the Alaska Department of Transportation (AK-DOT) Roadway Weather Information System (RWIS[4]) network. There were three sites from the WRCC, eleven buoys, 24 NCDC sites, and seven sites from the AK-DOT. This data resulted in a total of 45 different surface stations throughout the Southeast Alaska model domain. See Fig. 2.4 for locations of the meteorological stations.

Data was downloaded from each sources' respective website, with the exception of RWIS[5]. Six main atmospheric variables were gathered: temperature (°C), dew-point temperature (°C), atmospheric pressure (hPa), relative humidity (%), wind speed (m/s), and wind direction (°). The data was processed on an hourly basis from May 15-September 15, 2008, the same time frame as the WRF/Chem simulations. The collection resulted in 2976 hours of observational data per site. Many sites recorded observations several times per hour. Therefore, data at applicable stations were filtered into an hourly time resolution, as model results were written out hourly due to disc space limitations. Observations located close to the top of an hour were rounded to the nearest hour. Rows of missing hourly data were filled with the appropriate missing data markers

---

[1] Retrieved from: www.wrcc.dri.edu
[2] Retrieved from: www.ncdc.noaa.gov
[3] Retrieved from: www.ndbc.noaa.gov
[4] www.dot.state.ak.us/iways/roadweather
[5] This data was sent directly from the AK-DOT, courtesy of Jack Stickel, RWIS manager.

so data would match up correctly to the model, which was archived every hour. All observations and WRF/Chem data were reported in UTC time. Alaska Standard Time (AST) is nine hours behind Greenwich Mean Time (UTC-9). Time is reported in both AST and UTC in this thesis.

2.6.2 Quality Assurance/Quality Control

Observational data was not always complete. In fact, sections of data were missing in a few locations due to technical malfunctions with the sensors, potentially due to storms, communication issues, or other unforeseeable mishaps. Atmospheric pressure measurements were not available from approximately half of the sites, as many sensors lack barometric pressure gauges. However, it was assured that a station would be chosen for analysis if some part of its record contained temperature measurements. Note that temperature measurements were the most complete in the dataset.

After processing the data, it became obvious that some sites needed to be eliminated that did not pass an established Quality Assurance/Quality Control (QA/QC) check. Each site was examined individually to determine how well the data fit with conditions assumed for that grid cell in the model. In the past, WRF/Chem has underestimated temperatures on land and sea. Thus, we investigated whether the dominant surface type matched between the site and the model. Even though some buoys were so close to land that WRF/Chem assumed them to be land and not water, correlations remained acceptable. Most stations performed well, returning correlations of 0.7 or higher (further analyses on skill scores are outlined in Chapter 3). QA/QC was completed on all 45 sites in the domain. Data was also checked for consistency, as well as for reasonable climatology for that area.

Station data for a given variable were removed from the database if there were less than 20 days of complete data. For example, some sites recorded data sporadically during the 2008 tourist season, but still contained at least 20 days of data. After completing QA/QC, we made the executive decision to remove the three stations from the WRCC. The Hoonah WRCC site only had 24 days of observations, as well as a mismatch in land use types. After plotting the data, extreme diurnal temperature ranges existed between day and night. While not unheard of during the summer time in Southeastern Alaska, WRCC recorded temperatures exceeding 29.5°C several times during the summer. These high temperature values existed at all three sites, which are located in the vicinity of Juneau. According to climatic statistics from the NCDC, the average

33

maximum temperature in Juneau during June, July, and August is 16.8, 17.7, and 17.1°C, respectively. The all time record high was 32.2°C. All three sites are located in an area close to the shoreline on the Inside Passage. These sites are close to the water, where such extreme diurnal courses are very unlikely at these latitudes. The differences in day and nighttime temperatures should not be as extreme due to oceanic influences. The retrieved data reflects climatology of an inland station, such as Fairbanks. Furthermore, the data did not fit into the greater picture of neighboring sites from other data providers. One has to assume that the sensor could have been affected by unexplained errors, human interactions, or errors in keying in the station site code from the dataset.

After removing the data of these three sites, analysis on the meteorological conditions continued, and we were left with 42 surface stations. This is still a very good number of sites, and is statistically useful (n ≥ 30). Observations are typically difficult to find in Southeast Alaska due to low population density and complex terrain variations from land to ocean. It is important to note that many stations are located in small towns, villages, or landing strips close to sea level, with minimal population. Therefore, if a site goes down, it may take some time for crews to repair it. The locations also mean that the observational network is slightly biased, especially towards easily accessible settlements (PaiMazumder and Mölders 2009).

2.6.3 Sources of Upper Air Data

Section 2.6.1 described the method of validating the model's performance at the surface level. However, it is also necessary to evaluate WRF/Chem's ability to accurately simulate the atmospheric profile above the surface. Therefore, we do this by comparing the model data with upper air soundings.

Radiosondes are launched from the Yakutat Airport (PAYA) twice a day at 0000 UTC and 1200 UTC. The balloon launch corresponds to 1500 AST (minus one day) and 0300 AST. The site is located 59.52°N, -139.67°W at an elevation of nine meters above sea level (Fig. 2.4). The airport is a public use, state-owned airport located 6 km from the town center. The airport was once an airfield built in 1940 as part of the United States Army's long-range defense program during World War II[6] (Fig. 2.8). Since then, the state has gained control and now runs

---

[6] For more history, visit: http://climate.gi.alaska.edu/history/SouthCentral/Yakutat.html

Figure 2.8 Approach of Runway 2 of the Yakutat Airport looking northeast towards the St. Elias Range. Photo taken August 26, 1959 by the FAA Photo Lab. Image is used with permission from Alaska Warbird Museum (courtesy of Bob Miller, 2013).

Figure 2.9 Network of radiosonde launching sites in Alaska[7]. There are only 14 sites in the entire state, an area that spans the equivalent distance from the East to the West Coast of the Continental U.S. This map is missing the Shemya Island (PASY) upper air site on the far Western Aleutian Islands. Yakutat (PAYA) is the closest upper air site to Glacier Bay located inside the red circle. Image is used with permission from the NOAA National Weather Service (NWS).

---

[7] Retrieved from: http://www.ua.nws.noaa.gov/nws_upper.htm

commercial and private air service through the airport. It also serves as one of the fourteen weather balloon launching sites in Alaska (Fig. 2.9). In Yakutat, the National Weather Service began using modern Väisälä RS80-56 radiosondes in December 1, 1995, replacing the outdated VIZ-B devices[8].

Yakutat is located on a flat spit of land next to the Gulf of Alaska (Fig. 2.4). The Pacific Ocean is less than 5 km to the south-southeast of the launching site, while Yakutat Bay forms an inlet towards the west-northwest, effectively placing Yakutat on a small peninsula. The St. Elias Mountains stretch from the Alaska mainland south of the Wrangell Mountains and traverse southeast along the panhandle. Extending from sea level to Mt. St. Elias, the tallest peak at over 5,000 m in elevation, the mountain range contains some of the highest coastal mountains in the world. While the mountains are present in all northerly directions from Yakutat, marine influences are also factored into the station's climate.

Although some topographical effects present in Glacier Bay will not be represented at the Yakutat site, Yakutat is the best sounding choice, as radiosonde observations in Alaska are sparse (Fig. 2.4). Depending on any fixed location in Glacier Bay, Yakutat is approximately 175-250 km northwest. In our model domain, the next closest radiosonde launching site is on Annette Island (PANT), situated well over 500 km to the southeast. Annette Island is barely located inside the modeled domain, therefore would not be as valuable as Yakutat due to boundary related effects (Pielke 2001). Thus, it was decided to only use the Yakutat data to evaluate the WRF/Chem model.

2.6.4 Particulate Matter

It is important to note that no chemistry measurements for particulate matter (PM) are available for Glacier Bay. A PM_{10} monitoring site is present in Petersburg, but is not very representative as it is over 250 km away from Glacier Bay, and downwind of urban influences. A closer $PM_{2.5}$ site is located in Juneau, but is not deemed accurate for our studies as it is located in a parking lot and exposed to direct vehicle emissions. Forward trajectories determined by Mölders et al. (2013) concluded that Glacier Bay was rarely downwind of any pollution generated from major cities and towns towards the southeast (e.g. Juneau, Petersburg).

---

[8] See this website for more radiosonde use information: http://www.ua.nws.noaa.gov/Equip.htm

Therefore, these sites are not representative in evaluating WRF/Chem's performance in Glacier Bay.

2.7 Skill Scores

Performance skill scores are used to represent how close simulated WRF/Chem values are from the actual observed values. Calculation of the skill scores was twofold. The first involved comparing surface meteorology outlined in section 2.6.1 to extracted surface WRF/Chem data. Data was pulled at corresponding grid points that matched the meteorological stations' coordinates. The second involved analysis of archived radiosonde data and extracted WRF/Chem simulated data for the same location.

2.7.1 Definition of Skill Scores

The following skill scores were used in this analysis: correlation coefficient (r), mean bias, standard deviation error (SDE), root mean square error (RMSE), and variance. They were calculated in a similar manner as in Mölders et al. (2011) following Anthes (1983), Anthes et al. (1989), von Storch and Zwiers (1999), Zhang et al. (2006), and Zhong et al. (2005). The results from this evaluation of meteorological quantities are outlined in Chapter 3.1 and 3.2.

In the following expressions, S_i and O_i are values of simulated and observed quantities at grid point and time i, respectfully. The total number of data values is denoted by n. The mean quantities for simulated and observed values (as show by von Storch and Zwiers (1999)) are given by:

$$\bar{S} = \frac{1}{n} \sum_{i=1}^{n} S_i \tag{2.2}$$

$$\bar{O} = \frac{1}{n} \sum_{i=1}^{n} O_i \tag{2.3}$$

The correlation coefficient (r):

$$r = \frac{\sum_{i=1}^{n}(S_i - \bar{S})(O_i - \bar{O})}{\sqrt{\sum_{i=1}^{n}(S_i - \bar{S})^2 \sum_{i=1}^{n}(O_i - \bar{O})^2}} \tag{2.4}$$

indicates the statistical relationship of how well the simulated and observed data relate to each other. The correlation value ranges from -1 to +1, where +1 implies a perfect correlation, 0 signifies no relationship, and -1 indicates the data have a very high negative correlation.

The mean bias (MB):

$$MB = \frac{1}{n}\sum_{i=1}^{n}(S_i - O_i) \tag{2.5}$$

measures how far off a model's predicted values are from the observations, and indicates systematic errors, which could be the result of model parameterizations, model parameter assumptions, or discretization errors (Zhong et al. 2005). The bias can also reflect errors in model interpretation of the landscape, such as terrain height and land use. Therefore, if the bias value is negative, the model generally underestimates the observations. A bias of 0 is a perfect score, but can still indicate systematic errors if the summation of negative and positive values cancel out (Mölders 2008).

The standard deviation error (SDE), or simply standard error:

$$SDE = \sqrt{\frac{1}{n-1}\sum_{i=1}^{n}\left((S_i - O_i) - (\bar{S} - \bar{O})\right)^2} \tag{2.6}$$

accounts for random errors that might have occurred due to initialization or boundary conditions, as well as measurement errors (Chang and Hanna 2004).

The root mean square error (RMSE):

$$RMSE = \sqrt{\frac{1}{n}\sum_{i=1}^{n}(S_i - O_i)^2} \tag{2.7}$$

is another method of testing a model's accuracy, and serves to represent overall systematic errors influenced by the accuracy of the dataset (Anthes et al. 1989).

The variance:

$$s^2 = \frac{\sum_{i=1}^{n}(X - \bar{X})^2}{n-1} \tag{2.8}$$

is measure of how far the values of one variable are spread from the mean, where X is the quantity being analyzed. The WRF/Chem simulation and the observation both have their own variance. This measure can be used to determine if simulated and observed quantities have

similar variance. In addition to these skill scores, the standard deviation (SD) is simply defined as the square root of the variance.

2.7.2 Mitsuta Method

In the analysis of wind direction for both surface based sites and radiosondes, the scalar mean wind direction was calculated using the Mitsuta Method (Mori 1986). Yasushi Mitsuta accounted for the discontinuity of wind direction when the northerly component can abruptly change between ≤ 359° and ≥ 1°. This consideration is done by assuming the difference between successive wind direction samples is less than 180°, allowing means and standard deviations to be calculated in a single pass.

2.8 Inversion Analysis Methodology

Since Glacier Bay is remote (Fig. 2.11), there is no extensive meteorological observation network inside the park. The closest settlement is Gustavus, but is approximately 15 km from the entrance of Glacier Bay. Only one station is located within the boundary of Glacier Bay National Park, and is a buoy in Bartlett Cove. Technically, the sensors are positioned at the end of a dock in Bartlett Cove, thus, not a buoy (Joel Curtis, personal communication, 2013). Nevertheless, the NDBC classifies it as a buoy on their website.

As shown in Chapter 3.3, skill scores from comparison of the Yakutat soundings and WRF/Chem vertical profiles are very good. Yakutat is too far from Glacier Bay to understand local inversions. Thus, our best estimate in determining inversions inside Glacier Bay is to use the simulated vertical profiles from WRF/Chem data.

Twenty seven grid cells make up Glacier Bay in the model domain (Fig. 2.10), each with a dominant land use type of water. Each grid cell contains a volume averaged value of WRF/Chem parameters for all 2976 hours in the tourist season. Temperature values exist on each of the 28 eta levels, which are terrain following, pressure coordinates with increasing thickness with height (Fig. 2.3). A modeled inversion was identified in a grid column if its change in temperature with change of height (dT/dz) from one level to the next was positive and greater than or equal to 0.5 K $(100$ m$)^{-1}$. More than one inversion per column, per time was possible, and was also captured. This identification process was repeated for each hour of the tourist season for

all twenty seven grid cells. Therefore, it could now be determined when and where inversions typically occur, and assess how strong they could potentially be in Glacier Bay.
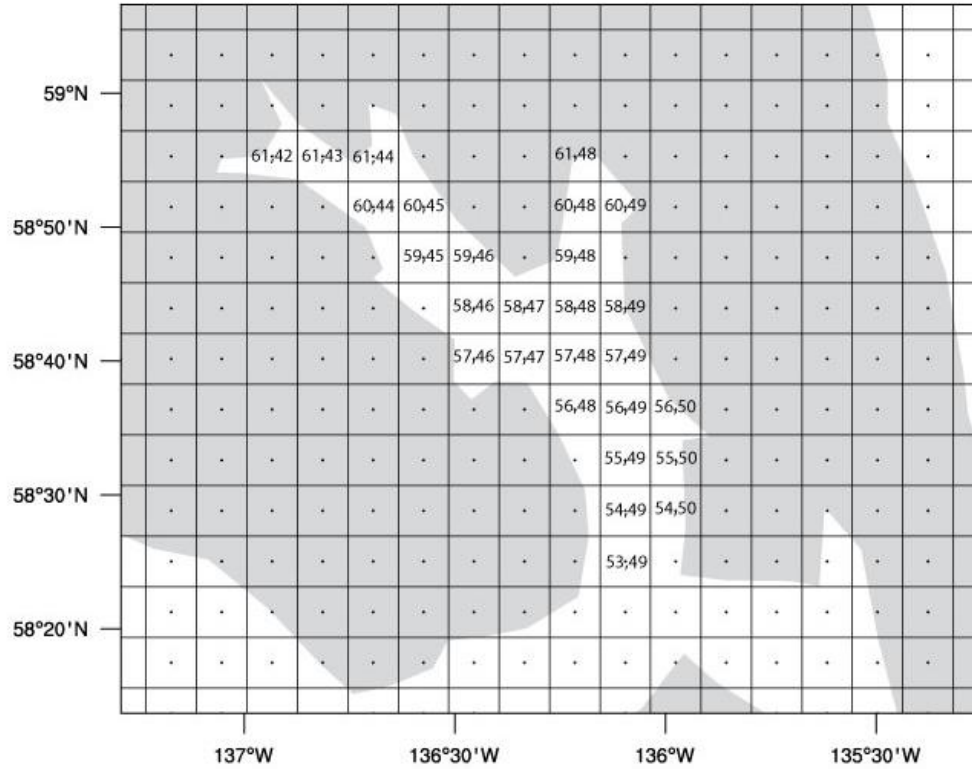
Figure 2.10 Map of the modeled boundaries of Glacier Bay, overlaid with individual WRF/Chem grid cells. The numbers inside each grid cell indicate their coordinates in the domain, and provide a convenient way of identifying their location when described in the text. Twenty seven grid cells are used for analysis, and each cell's dominant land use type is water.
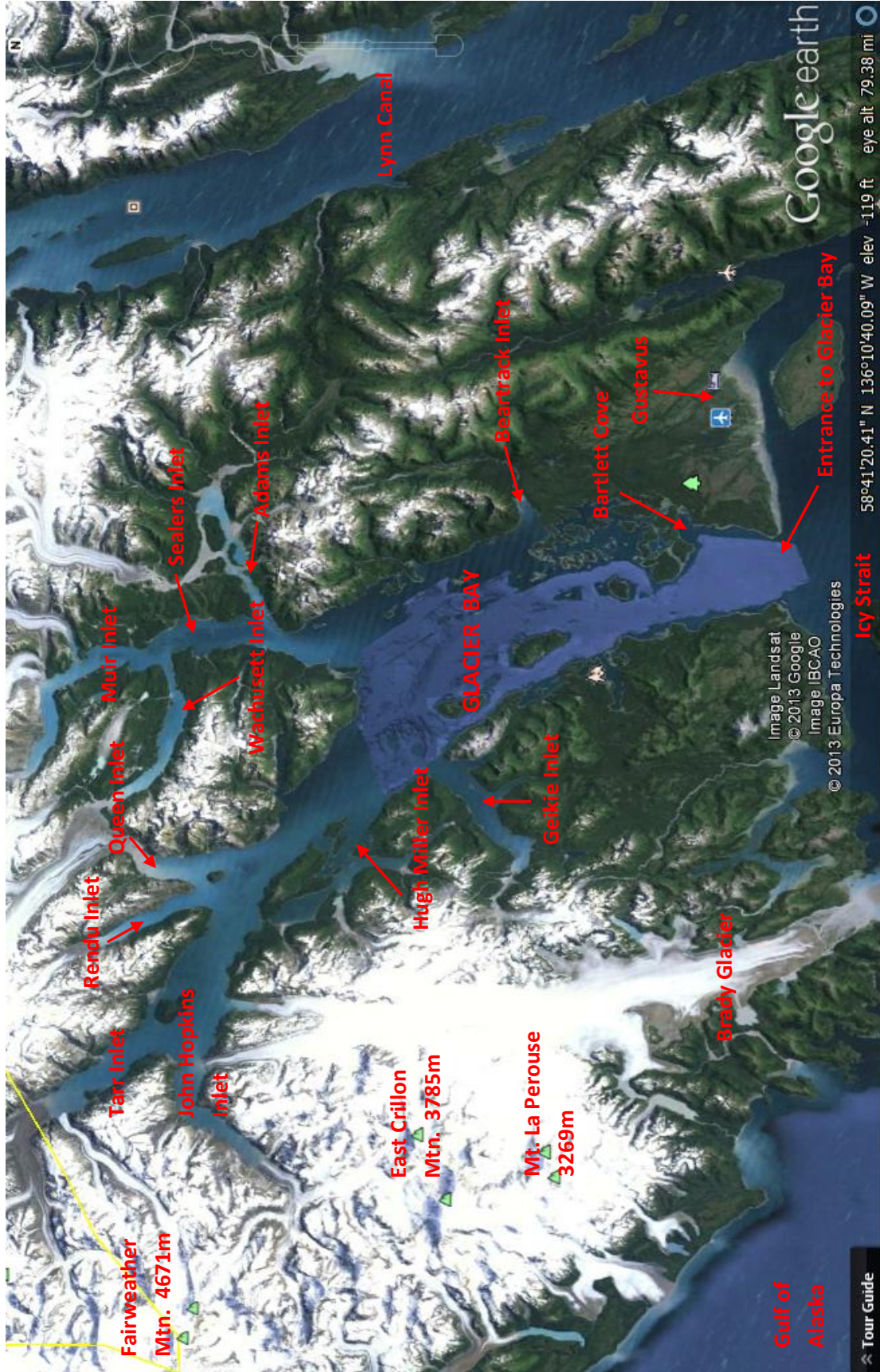
Figure 2.11 Google Earth satellite imagery of Glacier Bay with major geographical features identified (modified from a Google Earth screenshot. Available at: www.earth.google.com).

Chapter 3 Model Evaluation Results

3.1 Evaluation of WRF/Chem and Surface Meteorological Data

WRF/Chem simulations are compared against hourly measurements of air temperature, dew-point temperature, relative humidity, wind speed, wind direction, and sea-level pressure at 42 surface sites (Fig. 2.4). None of the sites recorded precipitation or shortwave radiation observations. The sources of this data are outlined in section 2.6.1. The following sections describe the skill score results from the model evaluation.

3.1.1 Methods

Table 3.1 contains the skill scores associated with the six meteorological quantities. The Taylor diagram in Fig. 3.1 displays the skill scores at different times throughout the tourist season. In general, WRF/Chem does an adequate job estimating surface temperature and dew-point temperature, but tends to slightly underestimate both (e.g. -0.6 K and -0.2 K, respectively). WRF/Chem slightly overestimates relative humidity (2.2%), wind speed (1.75 m/s), and wind direction (6°) by small quantities. Sea-level pressure was simulated the best, with a correlation of 0.996. It is slightly underestimated in WRF/Chem by -0.89 hPa, which is mainly due to topographical issues.

Most of the errors associated with WRF/Chem can be attributed to terrain influences. In Southeast Alaska, terrain is so complex that some regions may vary in elevation from sea-level to hundreds of meters within a short horizontal distance. Latitude and longitude from each surface station was recorded, and WRF/Chem data at the same time frame was extracted from a grid cell that matched the sites' coordinates. Each 7 km by 7 km grid cell contains volume averaged quantities by layer thickness for that region. Dominant land-use type and elevation is assumed to be representative for that entire grid cell.

There are generally two major errors regarding the misrepresentation of terrain in this WRF/Chem simulation. The first issue was that the model sometimes had problems discerning land and sea. Most communities in Southeast Alaska are located in coves, fjords, or valleys directly at the edge of the sea. With the absence of an elaborate road system, the ocean effectively acts as the region's transportation and economic gateway. Many of the meteorological sites are located at the coast, on a beach, or on a buoy adjacent to coastline. Thus,

the measurement network is strongly biased towards easily accessible settlements. Different meteorological results are likely if the dominant land-use type for a land based station is actually interpreted as water in the model, or vice versa. As a result, two or more grid cells are necessary to resolve these problems. A dominant land-use type for a grid-cell identified as water will have a smaller roughness length than one with vegetation. For example, the roughness length of an evergreen needle leaf forest is approximately 50 cm while a water body is 0.01 cm. A water-body grid cell will also have a lower albedo, more available moisture, higher heat capacities, and generally a higher emissivity than most other dominant land-types with vegetation (Chen and Dudhia 2001).
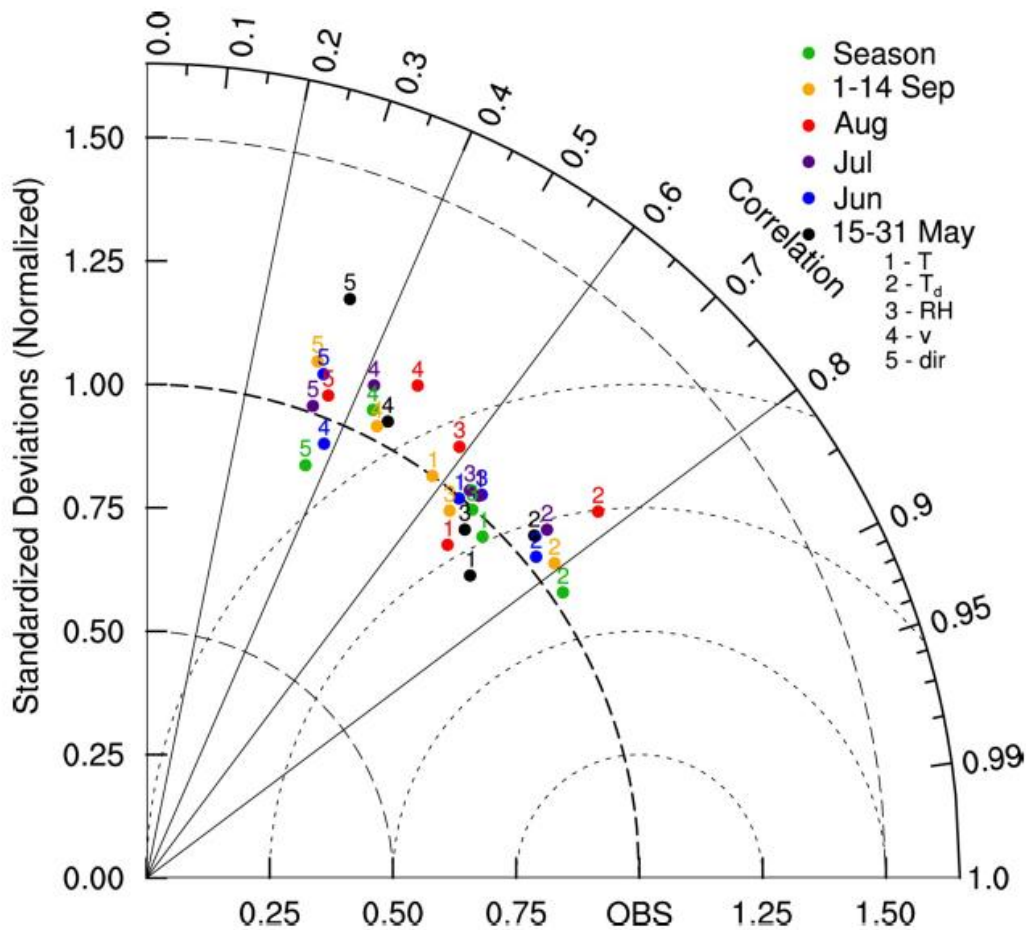
Figure 3.1 Taylor diagram showing WRF/Chem's performance statistics for temperature, dew-point temperature, relative humidity, wind speed, and wind direction for each month, as well as over the entire tourist season. Solid lines indicate correlation, dotted lines are normalized RMSE, and dashed lines are normalized standard deviations. Data close to OBS indicates a perfect forecast, while the scores on the bold-dashed arc have correct standard deviations (Mölders et al. 2013).

More than half (22 out of 42) of the sites were identified as water (0 m). Seventeen are actually on water. Out of the eleven buoys, all but one was correctly identified as water. The buoy for which WRF/Chem assumed land instead of water was given the land-use type of evergreen needle leaf forest due to the buoy's proximity to the land, and the dominance of land in that grid cell. Six stations from NCDC were sea-plane bases with elevations of 0 m. In WRF/Chem, three out of the six were actually treated as ocean sites. Out of the remaining 25 land sites, nine were incorrectly treated as ocean because water was the highest percentage in the respective grid cells. The land-use type for land sites correctly represented as "land" (i.e. not water) were either evergreen needle leaf forest or wooded tundra.

The second source of systematic error is that the model terrain height for an individual station could be higher or lower than in actuality. Most sites' elevations were estimated within relatively good accuracy (less than ± 50 m), but others had very large errors. This discrepancy is common in many models, since an averaged terrain height in a grid cell is assumed. In WRF/Chem, a calculation is done using a geo-grid with terrain values at approximately 30 second, two-minute, five-minute, or ten-minute increments. This simulation used a geo-grid with ten minute data resolution. Thus, the terrain height over a grid cell is averaged and subsequently smoothed. At the 7 km by 7 km grid-cell increment, there are often problems that result in areas of rapidly changing terrain.

In WRF/Chem, a station's actual elevation tended to be approximately 81 m higher on average over all 42 stations than seen in nature. The difference in elevation affects the quality of the model output for some parameters, namely sea-level pressure and temperature. Some higher elevation sites have lower correlation values due to the differences in the model terrain and actual elevation being up to, or surpassing 800 m. Ten sites were about 100 m or more higher in the model than in the real world. Of those ten, four were over 500 m too high, with nothing exceeding 890 m. Ten sites were higher in reality than in the model, but no elevation difference in those sites surpassed 35 m. Fig. 3.2 shows a histogram of the WRF/Chem model terrain heights (solid blue) in comparison to the "nearly" real geo-grid terrain heights (hatched blue) over the entire domain. Terrain heights are binned starting at 0 m (water) and upwards in 100 m increments. The highest terrain in the domain was approximately 4200 m, but the plot was trimmed at 2200 m to show terrain heights that are more frequent. Out of all terrain values in the model domain, 0 m dominated since water is approximately 30% of the domain. WRF/Chem had

a higher amount of grid-cells in the 0 m bin, where they actually may be a few meters above sea-level (this was very common regarding several of our sites that were only a few meters above sea-level). This reason is why the second bin (1-100 m) has a higher frequency of actual terrain height showing up in that range. As Fig. 3.2 shows, the terrain height distribution was acceptably represented in the model, and the observations are strongly biased to represent low elevation. However, this bias in the network is not a disadvantage to the study, as the interest is on the meteorology and air quality over Glacier Bay's waters. Despite these terrain challenges, WRF/Chem had respectable performance in the calculation of the outlined quantities discussed in the following sections.
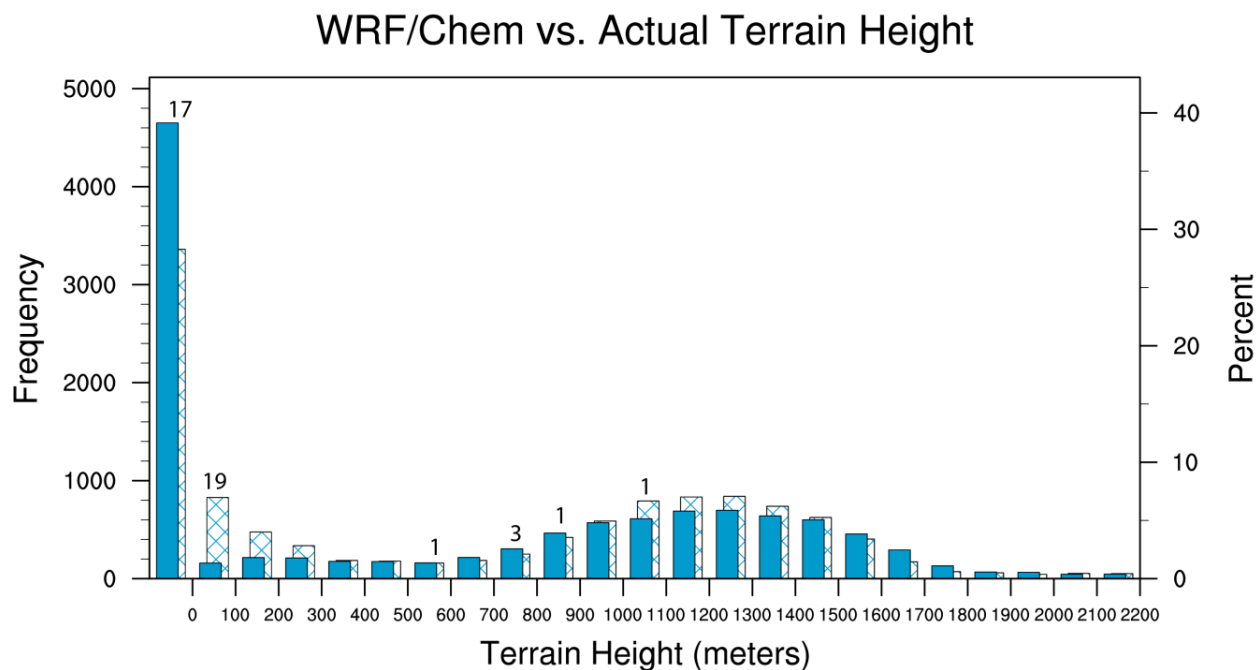
Figure 3.2 Histogram of WRF/Chem and "nearly" real terrain height, as used in the ten-minute geographical dataset over the entire domain. Solid blue bars indicate WRF/Chem grid-cell terrain heights and hatched bars indicate the geodata terrain. High frequencies of terrain height in the 0m bin show nearly 30% of the domain is water. Numbers above each set of bars indicate the number of meteorological sites with actual elevations that fit inside the respective 100 m bins.

3.1.2 Temperature

From May 15 to September 15, 2008, WRF/Chem captured the temporal evolution of surface air temperature well, but tended to underestimate the values by a slight margin (Fig. 3.3). The diurnal cycle of temperatures is evident in Fig. 3.3a, which displays the hourly average

temperature values over all stations in the domain. WRF/Chem dampens this diurnal cycle, but temperatures show good agreement that WRF/Chem is able to capture the progression of temperatures throughout the summer. A small underestimation of temperatures in the model results in a slight cool bias of -0.6 K. Hourly temperatures are well correlated at 0.70, with a RMSE of 2.5°C and SDE of 2.4°C, indicating high random errors. The standard deviation of the simulated temperature was 3.0°C, which is on par with the observed standard deviation of 3.1°C. The statistics are consistent with other studies using WRF or WRF/Chem in high latitude regions (Brown 2008; Hines and Bromwich 2008; Mölders 2008; Porter 2009; Mölders et al. 2011; 2012).

The errors in temperature likely come from a variety of sources, but it appears that random errors slightly outweigh systematic errors. This behavior is most likely due to misrepresentation of land-surface processes or convection. The cold bias could also be the result of an underestimation of incoming shortwave radiation. Unfortunately, none of the stations in Southeast Alaska have radiation measurements for this episode to confirm this hypothesis. Less shortwave radiation reaching the surface could be indicative of high amounts of cloud cover, which tends to decrease surface temperatures. WRF/Chem may have overestimated the cloudiness in the cumulus convection parameterization. Cumulus convection tends to be one of the most difficult items to model, since most clouds are generally sub-grid scale in size. On the other hand, this region of Alaska is constantly exposed to oceanic influences and localized terrain-induced weather.

As stated at the beginning of this section, WRF/Chem terrain height tended to be higher than many of the stations' actual elevations, which could have also led to the cool bias. The mismatch in land-use types for certain stations results in differing albedo, and could cause errors in the surface temperature. Although the temperature errors are minor, they could affect other meteorological fields, including dew-point temperature and relative humidity. As a general property of the Clausius-Clapeyron equation, lower temperatures are needed for saturation to take place. Thus, WRF/Chem may achieve saturation sooner and overestimate cloudiness and precipitation. The latter cannot be examined as no precipitation measurements were available.

Table 3.1 Skill scores summarizing the simulated and observed surface meteorological data. Data compares the average ± standard deviation of modeled and observed quantities, as well as quantitative skill scores: root mean square error (RMSE), standard deviation error (SDE), bias, and correlation. Variables include average temperature (T), dew point (T_d), relative humidity (RH), sea-level pressure (SLP), wind speed (v), and wind direction (Dir). Skill scores are displayed hourly (1 hr) and daily (24 hr) for the tourist season (May 15 to September 15, 2008).

	Hourly Season					
	Modeled	Observed	RMSE	SDE	Bias	Correlation
T (°C)	10.4 ± 3.0	11.1 ± 3.1	2.5	2.4	-0.6	0.70
T_d (°C)	7.2 ± 3.4	7.4 ± 3.3	2.0	2.0	-0.2	0.83
RH (%)	79 ± 16	77 ± 16	13	13	2	0.66
SLP (hPa)	1013.97 ± 6.50	1014.86 ± 6.79	1.11	0.93	-0.89	~1
v (m/s)	4.40 ± 2.74	2.64 ± 2.60	3.34	2.84	1.75	0.44
Dir (deg)	181±83	171 ± 93	97	95	10	0.36
	Daily Season					
	Modeled	Observed	RMSE	SDE	Bias	Correlation
T (°C)	10.4 ± 2.5	11.0 ± 2.2	2.0	1.9	-0.6	0.69
T_d (°C)	7.2 ± 3.3	7.4 ± 3.1	1.65	1.6	-0.2	0.87
RH (%)	80 ± 14	78 ± 12	10	10	2	0.71
SLP (hPa)	1013.97 ± 6.30	1014.86 ± 6.58	1.04	0.87	-0.89	~1
v (m/s)	4.45 ± 2.21	2.69 ± 2.12	2.78	2.15	1.77	0.51
Dir (deg)	182 ± 63	178 ± 67	66	59	2	0.45

a) Hourly Average Temperature

b) Daily Average Temperature

Figure 3.3 a) Time series plots illustrating hourly and b) daily average temperatures from the 42 sites in the domain during the 2008 tourist season. Blue polymarkers indicate the average observed value, red line is the average simulated WRF/Chem value, and the gray shading is the mean standard deviation from the observed mean value over all sites. The diurnal course is evident in plot a). Plot b) also shows spatial standard deviations averaged for all sites.

3.1.3. Dew Point Temperature

WRF/Chem captured the temporal evolution of dew-point temperature second best out of all the meteorological quantities (Fig. 3.4). The hourly values are strongly correlated at 0.83. Daily averages increase this correlation to 0.87, as errors in the range of the diurnal cycle average out. There is a very small dry bias of -0.2 K. The RMSE and SDE are very good and generally consistent, at 2°C and 2°C, respectively. Standard deviation of the observed dew point temperature was 3.3°C, following close behind the modeled standard deviation of 3.4°C.

The SDE indicates small systematic errors, most likely the result of inaccurate surface and moisture fluxes. This error could be due to land-use or land-cover variations, or incorrect sea-surface temperatures. The ocean has a strong influence in this region, since many sites are on the coast. The RMSE indicates the overall errors (Mölders 2008).

WRF/Chem had difficulties simulating the temporal evolution near the beginning of the tourist season, particularly around May 25. Synoptically, this period was generally quiet with clear skies and high pressure. Average surface temperature increased from about 8 to 13.5°C at this time. The model captured the temperature spike, but overestimated the amount of moisture that was present. Despite this difficulty, the observations show the modeled data is still within one standard deviation of the observations. This small spike in modeled dew point temperatures followed with an increase in both modeled and observed relative humidity values. WRF/Chem has been known to be sensitive to abrupt changes in atmospheric conditions (Mölders and Kramm 2010; Mölders et al. 2011). In addition, this episode is also around a time when WRF/Chem modeled inversions occurred. A similar feature regarding a dew-point temperature spike was documented by Porter (2009), where her WRF/Chem study took place off coastal areas of southwestern Alaska.

a) Hourly Dew Point Temperature

b) Daily Dew Point Temperature

Figure 3.4 a) Time series plots illustrating hourly and b) daily average dew point temperatures from the 42 sites in the domain during the 2008 tourist season. Blue polymarkers indicate the average observed value, red line is the average simulated WRF/Chem value, and the gray shading is the mean standard deviation from the observed mean value over all sites. The diurnal course is evident in plot a). Plot b) also shows the spatial standard deviations averaged for all sites.

3.1.4 Relative Humidity

Relative humidity was generally overestimated by a small margin during the 124 day period (Fig. 3.5), but WRF/Chem was able to simulate the temporal evolution of relative humidity well. There was only a 2% wet bias, and the hourly data were adequately correlated at 0.66. Daily averages increase this correlation to 0.71. The modeled and observed data had average values of 79% and 77%, respectively, and both had a standard deviation of 16%. The RMSE and SDE both returned values of 13%, which again, is on par with other studies outlined above (Brown 2008; Hines and Bromwich 2008; Mölders 2008; Porter 2009; Mölders et al. 2012). According to the RMSE, bias, and SDE, the errors were most likely a result of initial and lateral boundary conditions, as well as land-use and terrain errors.

However, it is interesting to note that the wet bias noted in the relative humidity is not present with a wet bias in the dew-point temperature. The likely reason why there were errors in temperature and dew-point temperature is due the overestimation of moisture fluxes, thus a tendency to over-predict relative humidity. WRF/Chem simulates moister conditions better than drier ones, particularly at the end of the tourist season when more storms tend to occur.
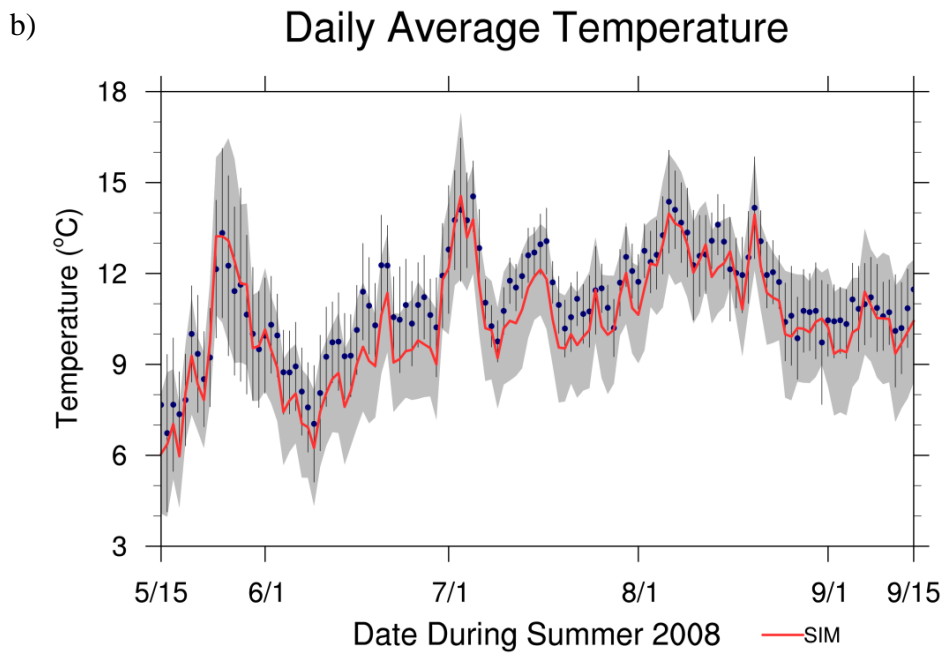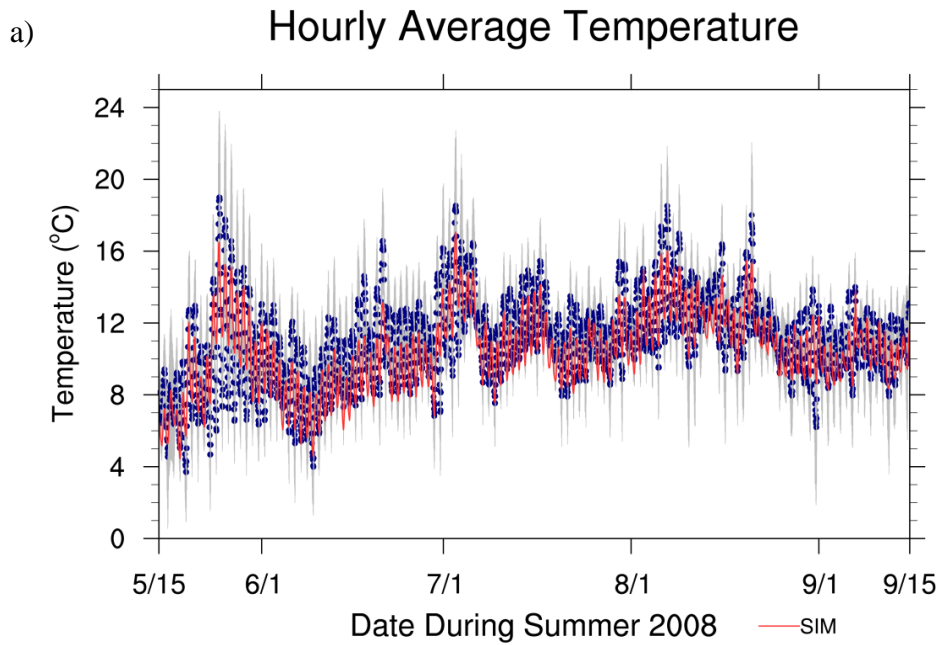
Figure 3.5 a) Time series plots illustrating hourly and b) daily average relative humidity from the 42 sites in the domain during the 2008 tourist season. Blue polymarkers indicate the average observed value, red line is the average simulated WRF/Chem value, and the gray shading is the mean standard deviation from the observed mean value over the domain. Plot b) also shows the spatial standard deviation averaged for all sites.

3.1.5 Wind Speed

During the tourist season, WRF/Chem consistently overestimated wind speed for almost all sites (Fig. 3.6). This overestimation may be due to the fact that terrain is smoothed more in the model than seen in nature. It captured the temporal evolution of the wind speed, especially when observed winds were generally high (> 4 m/s). WRF/Chem had a bias of approximately 1.75 m/s, RMSE of 3.34 m/s, and SDE of 2.84 m/s for the entire tourist season. The hourly data were moderately correlated at 0.44, while daily wind speed averages increased this correlation to 0.51. This indicates slight errors in timing of frontal passages. The average modeled wind speeds were approximately 4.4 m/s, while observed average wind speeds were 2.6 m/s. Both modeled and observed quantities had quite similar standard deviations of 2.7 and 2.6 m/s, respectively.

These trends and skill scores are consistent with other studies using WRF in high latitudes (Brown 2008; Mölders 2008; Porter 2009; Mölders et al. 2012). However, it is important to note that WRF/Chem has a difficult time estimating wind speeds over complex terrain. While Southeast Alaska may contain some of the state's roughest and most abruptly changing areas of terrain, we have to consider our results good for the area they represent.

From the statistical results, systematic errors outweigh random errors due to terrain influences. As previously stated, most of the observation stations are located on the water's edge inside deep valleys, fjords, or on buoys adjacent to land. Thus, channeling effects of low level winds are highly likely in most cases. Local effects cannot be ruled out, such as high turbulence, since almost all sites are located in mountainous and forested regions. Also, many stations are exposed to maritime influences, such as land-sea circulations. Some of these circulations may be sub-gridscale with respect to the 7 km^2 grid resolution.

While the model could pick up wind-speed increases due to synoptic storms, it still tended to overestimate them. Conversely, it had trouble estimating winds when the weather was calm. This behavior has been noted by Mölders et al. (2012) in a study in Interior Alaska where winter near-surface wind speeds are generally very calm. Errors under calm conditions were also shown by Zhao et al. (2011) in California, where a large wind speed bias and RMSE existed for WRF simulations when winds were less than 1.5 m/s.

It is also worthwhile to mention that many anemometers may not record wind speeds under 0.5-1 m/s. During periods of calm weather, an anemometer may register very little, if any
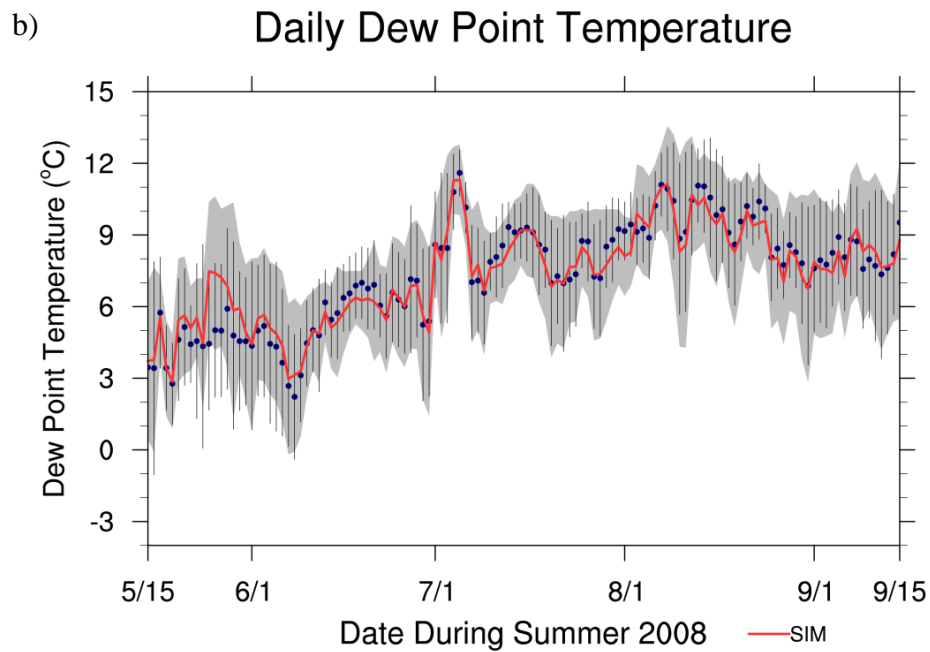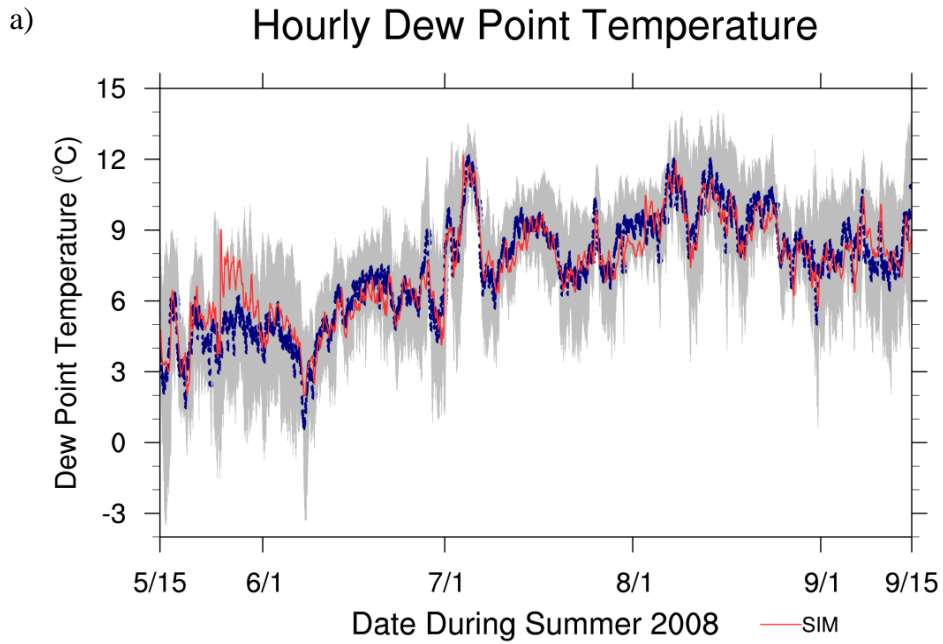
a) Hourly Wind Speed
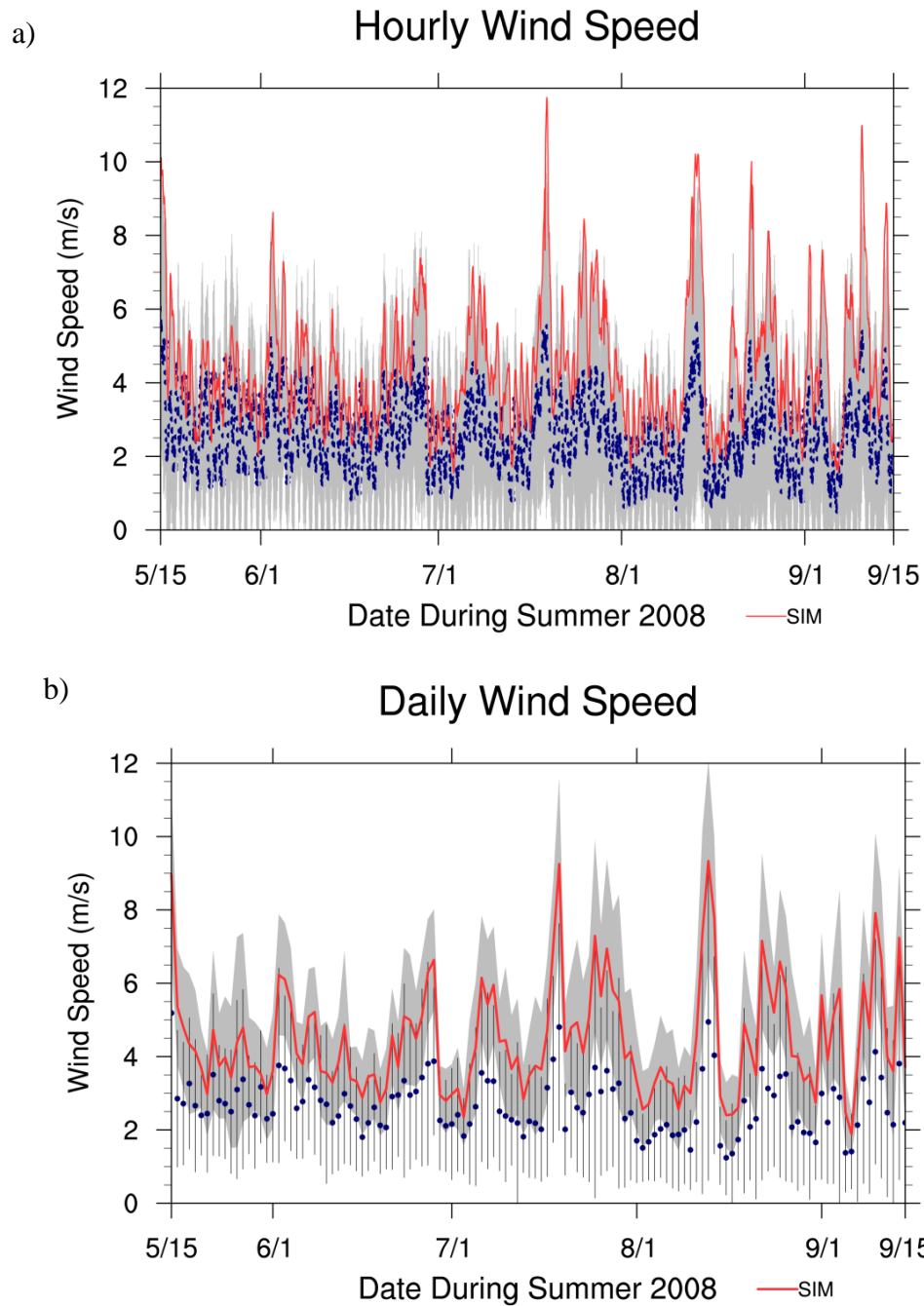
b) Daily Wind Speed

Figure 3.6 a) Time series plots illustrating hourly and b) daily average wind speeds from the 42 sites in domain during the 2008 tourist season. Blue polymarkers indicate the average observed value, red line is the average simulated WRF/Chem value, and the gray shading is the mean standard deviation from the observed mean value over domain. Plot b) also shows the spatial standard deviation averaged for all sites.

actual wind speeds, while WRF/Chem data is reported as low as 0.1 m/s. The model data may be more precise, but will often overestimate the actual wind speed in this case since the anemometer is recording 0 m/s.

3.1.6 Wind Direction

Wind direction is an extremely variable quantity, and a first glance at Fig. 3.7a may seem as though the data span a very large range. However, reducing the hourly wind direction averages to daily averages considerably trims the standard deviation and provides a clearer picture of the mean wind direction for the 124 day period. Despite a low correlation of 0.36 for hourly wind direction, the correlation increases appreciably to 0.45 when reduced to daily measurements, making the temporal evolution of wind speeds quite good when referring to Fig. 3.7b. These findings suggest slight offsets in timing as a source of error.

WRF/Chem can capture general changes in wind direction well, and the winds in Southeast Alaska generally fluctuate between 150-250°, or from the south-southeast to west-southwest. This behavior is to be expected, as weather systems typically approach from the west over the Gulf of Alaska, however, large mountain ranges and islands often divert wind.

There are notable channeling effects to keep in mind. As stated in Section 3.1.5, most observational stations are located at the bottoms of valleys, where topographical effects are likely to dominate. Thus, the mean modeled and observed wind direction for the entire tourist season was 181° and 171°, respectively, resulting in a positive bias of 10°. These statistics are even better for daily data, which reduces the bias to 2°. Hourly RMSE and SDE are 97° and 94°, respectively but 66° and 59° for daily averages.

The model performed better in this study than in Mölders et al. (2011; 2012). One reason is that winds in Southeast Alaska tend to have a more prevailing flow due to oceanic influences than they do in Interior Alaska. Wind direction in the Interior may fluctuate considerably depending on the passing of storms, but is commonly quite calm in Interior Alaska, especially during winter months.

a) Hourly Wind Direction

b) Daily Wind Direction
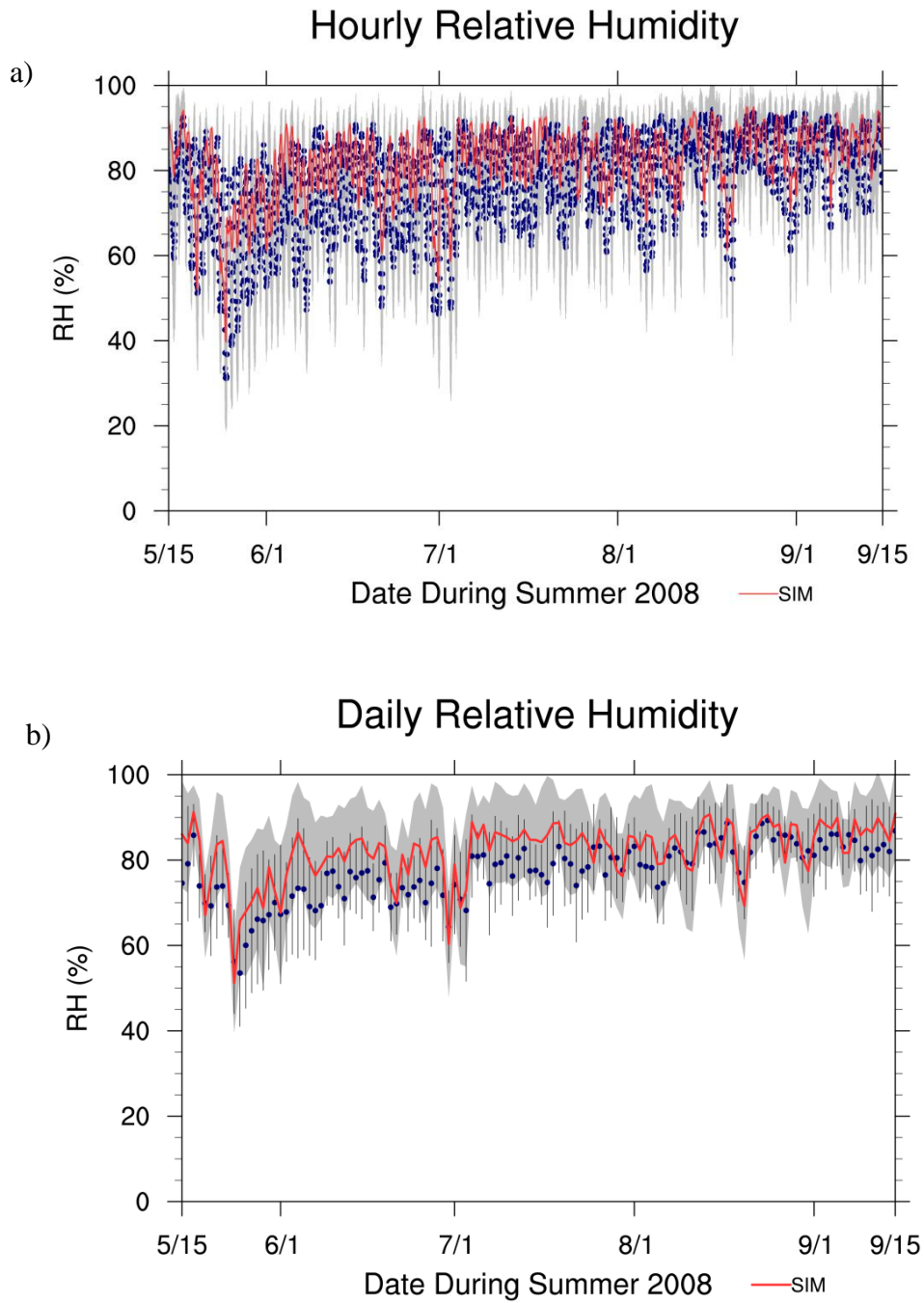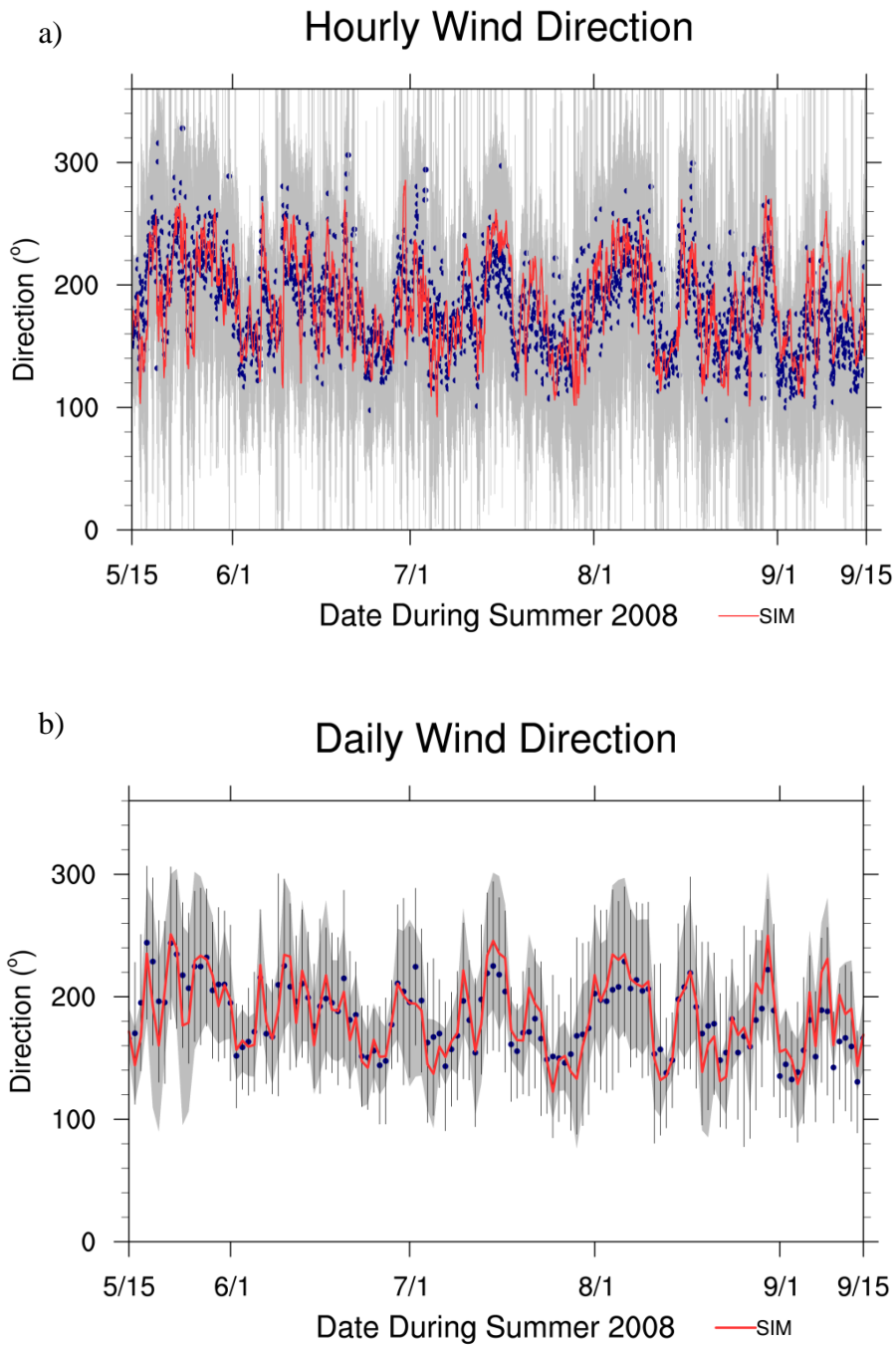
Figure 3.7 a) Time series plots illustrating hourly and b) daily average wind direction from the 42 sites in the domain during the 2008 tourist season. Blue polymarkers indicate the average observed value, red line is the average simulated WRF/Chem value, and the gray shading is the mean standard deviation from the observed mean value. Plot b) also shows spatial standard deviation over all sites. The dominant wind direction is from about 150°-250°, or approximately from the south-southeast to the west-southwest. Discontinuities with the abrupt change in wind direction from ≤ 359° and ≥ 1° were accounted for using the Mitsuta Method (Mori 1986).

3.1.7 Sea-Level Pressure

Although there were some considerable topographical issues when WRF/Chem interpolated the elevation of meteorological sites, sea-level pressures were simulated best out of all quantities (Fig. 3.8). The temporal evolution of the modeled data follows the trend of the observation data well, and WRF/Chem only underestimates the sea-level pressure with a bias of about -0.89 hPa. However, it must be noted that just over half of the sites (24 out of 43) actually recorded sea-level pressure. Therefore, the results discussed here are not completely representative of the entire domain as there are some missing observations.

The hourly mean modeled pressure was 1013.97 hPa ± 6.50 hPa. Conversely, the observed data was 1014.86 ± 6.79 hPa. The data were extremely well correlated, at approximately 0.996 (~1). The RMSE and SDE were low, 1.11 hPa and 0.93 hPa, respectively, resulting in low systematic and random errors. These trends and magnitudes of errors in the simulated and observed sea-level pressure data have also been documented in previous WRF studies, such as in Brown (2008), Porter (2009), and Mölders et al. (2011).

Slight errors could be the result of the hypsometric equation, which is used to convert pressure to sea-level pressure. Porter (2009) noted that WRF/Chem tended to predict sea-level pressure better when terrain heights were overestimated and surface air temperatures were underestimated. This also seems to be the case in this study. Some of the stations that had pressure data were also strongly mismatched in their terrain heights. For example, Skagway's elevation is 14 m, yet the grid cell chosen for that town had a mean elevation of 886 m. Skagway is located at the end of a deep inlet surrounded by tall mountain peaks. In addition, the overestimation of wind speeds suggests that WRF/Chem overestimated pressure gradients.

a) **Hourly Surface Pressure**

b) **Daily Surface Pressure**
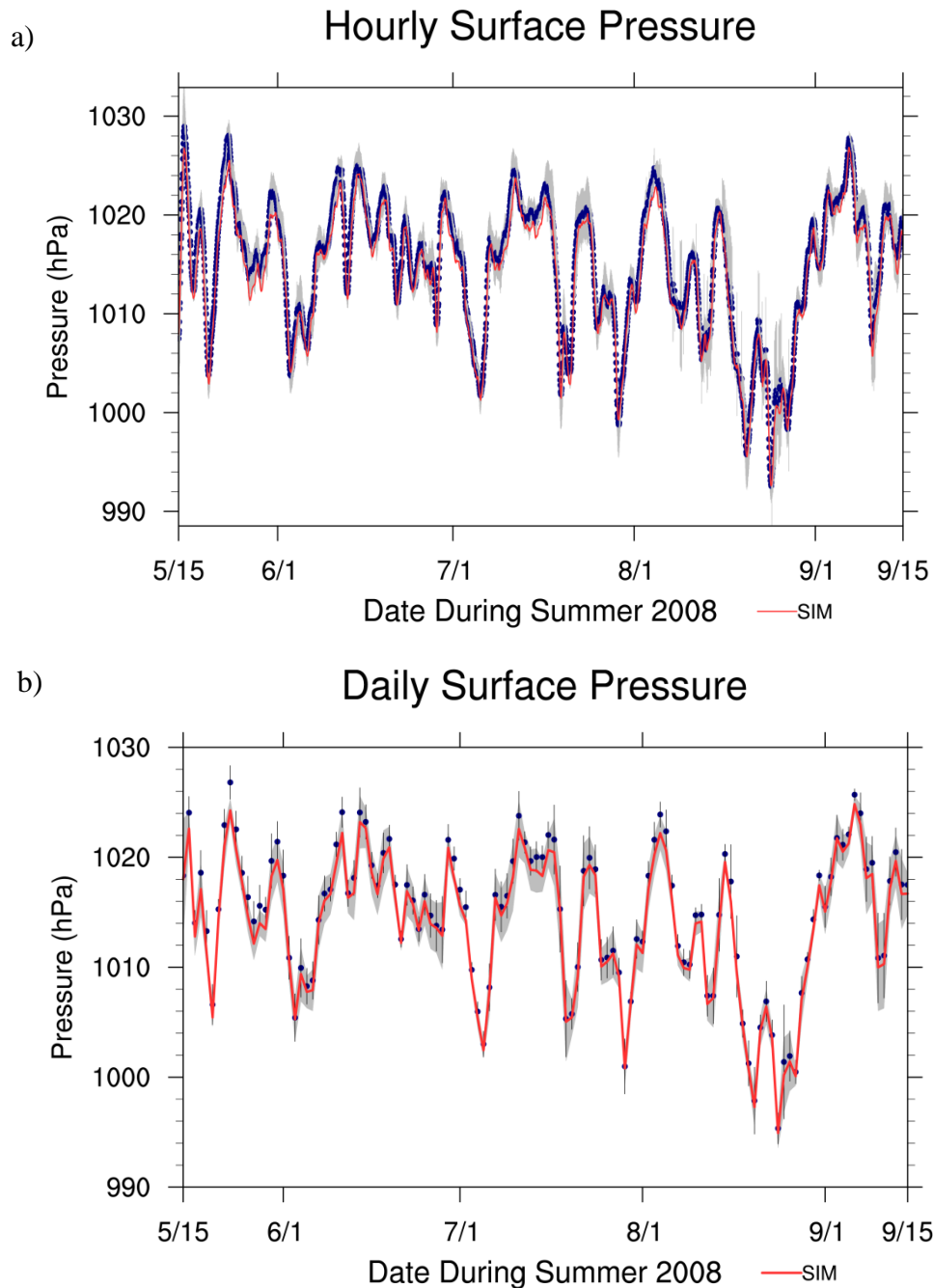
Figure 3.8 a) Time series plots illustrating hourly and b) daily average surface pressure from the available sites in the domain during the 2008 tourist season. Blue polymarkers indicate the average observed values, red line is the average simulated WRF/Chem values, and the gray shading is the mean standard deviation from the observed mean value. Plot b) also shows spatial standard deviation over all sites. The simulated values follow the temporal evolution of the surface observations very well.

3.2 Evaluation of WRF/Chem and Radiosonde Data

The analysis of the WRF/Chem simulation for the 2008 tourist season considers 124 days of observations, which corresponds to a total of 248 radiosonde ascents. The WRF/Chem grid column that matched the latitude and longitude location of the Yakutat radiosonde launching site was assumed to represent the radiosonde profile. Note that the radiosonde tends to move with the wind. However, while ascending above the ABL, the difference due to this fact is marginal.

Twenty seven vertical levels of WRF/Chem data were then used in the analysis for each individual ascent at either 0000 UTC or 1200 UTC each day. The modeled and observed data were plotted on the same skew-T diagram for analysis. Then, WRF/Chem data including temperature, dew-point temperature, pressure, geopotential height, wind speed, and wind direction were extracted for each of the twenty seven eta levels for skill score evaluation. Skew-T diagrams with examples of good, typical, and poor WRF/Chem performance at Yakutat are shown in Fig. 3.9.

3.2.1 Methods

Data below 12,000 m was only considered in this analysis, which is well above the 60°N summer tropopause height of approximately 10,000 m (Hoinka 1998). Generally, the model had difficulty estimating conditions at the tropopause where there are abrupt changes in meteorological quantities. Additionally, sensors on the radiosonde may not be able to accurately take measurements before the weather balloon pops at a critical altitude or drifts as it ascends. Data above the 12,000 m was discarded, which generally truncates the WRF/Chem data at level 23 or 24, typically around 200 hPa.

The data was then interpolated at radiosonde geopotential heights and assigned to corresponding data at matching WRF/Chem levels. The thickness of each model level is generally smaller close to the surface and grows with height. This relationship was outlined in section 2.1.1 (Fig. 2.3). Refer to the equations outlined in that section to understand the terrain-following vertical pressure coordinate system.

Table 3.3 outlines the WRF/Chem and radiosonde interpolated heights. The radiosonde analysis uses mean grid-point centers for its evaluation. WRF/Chem assigned an elevation of six meters for the grid point where the Yakutat radiosonde is launched, which is only three meters

lower than the actual elevation. Thus, terrain discrepancies at the launching site were not an issue.

Missing observation data was one of the downfalls with this analysis. Four ascents were missing from the entire season, i.e. 0000 UTC and 12000 UTC for both June 29 and August 25. In addition, the radiosonde data was not always complete for quantities such as wind speed, wind direction and geopotential heights. This shortcoming may have been the cause of relatively lower overall correlation values (r=0.69 and r=0.66 for wind speed and direction, respectively). However, air temperature and dew-point temperature were best represented in the observational data, with correlation values of r=0.85 and 0.60, respectively. The software used to interpolate raw radiosonde data eliminated data above 12,000 m, as well as data with missing air and dew-point temperatures. Thus, T and T_d were 100% available, with the exception of the four missing ascents. In general, the model well captured most of the observed profile characteristics, especially the general temporal evolution of the entire upper air profiles for the four meteorological variables: temperature, dew-point temperature, wind speed, and wind direction.

The small gap depicted on the lower portion of Figs. 3.10-3.13 is due to missing data at the sixth WRF/Chem interpolated level. The average height of this level, 611.3 m with a range in height from approximately 506 m to 716 m, lacked a sufficient number of observational data. There were only two interpolated observations, which is far too few for a meaningful analysis (von Storch and Zwiers 1999). After eliminating the two data values, the gap in the graph is the result of missing data markers. Statistics were calculated following this QA/QC check, and calculations simply ignore the sixth model level.

Comparison with the evaluation of radiosondes for winter performed by Mölders et al. (2011) showed that WRF/Chem is much more likely to produce more accurate summer simulations than winter simulations. This behavior is because the model has difficulties reproducing sudden temperature changes of more than 10 K per day, or has issues in predicting extremes (Mölders and Kramm 2010; Mölders et al. 2011). The previously mentioned studies were conducted during the winter in Interior Alaska, when temperatures can frequently drop below -40°C. In addition to extreme temperatures swings, strong temperature inversions commonly develop close to the surface. WRF/Chem is able to capture these inversions below 2 km, but often underestimates their strength. As a harbinger to the inversions, the authors also determined that WRF/Chem had problems simulating vertical exchanges of heat due to strong

a) Yakutat at 2008-07-07_00:00:00

b) Yakutat at 2008-06-08_00:00:00

c)
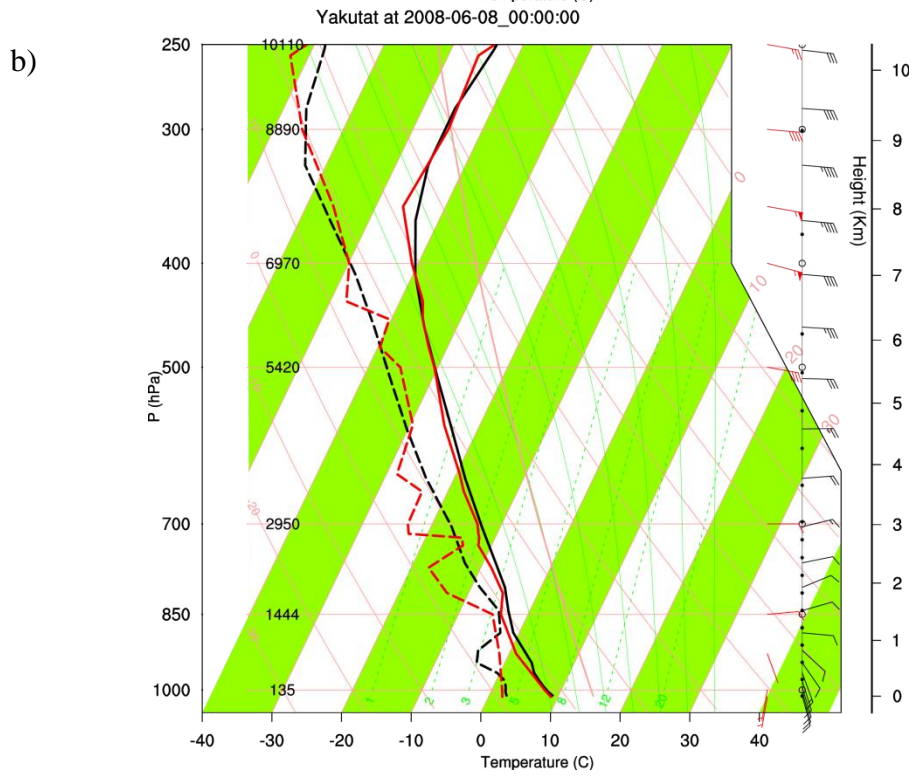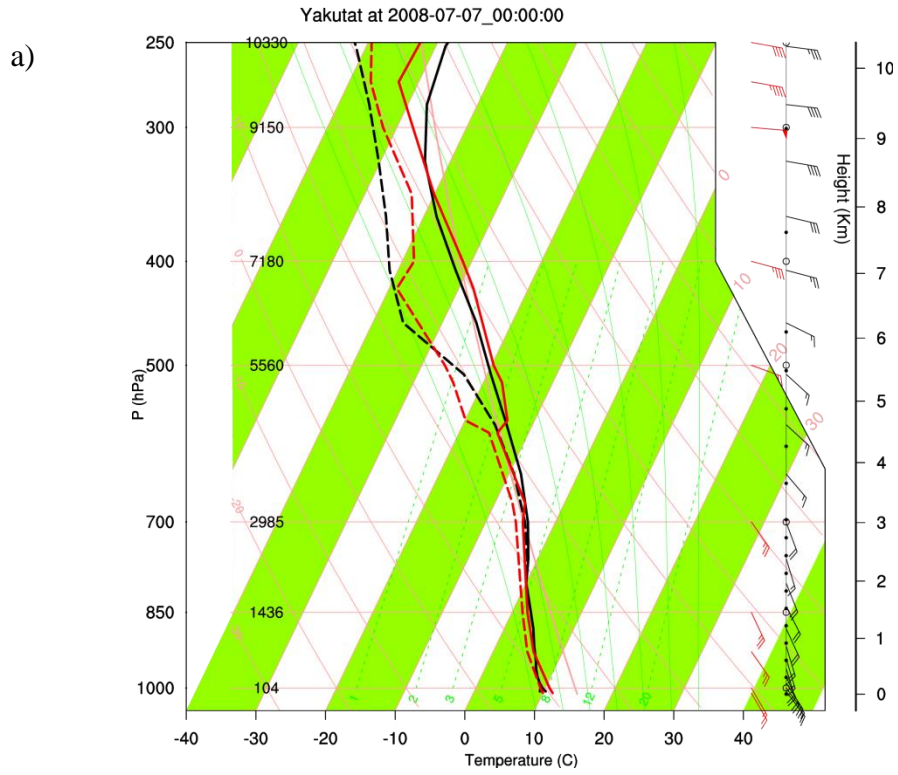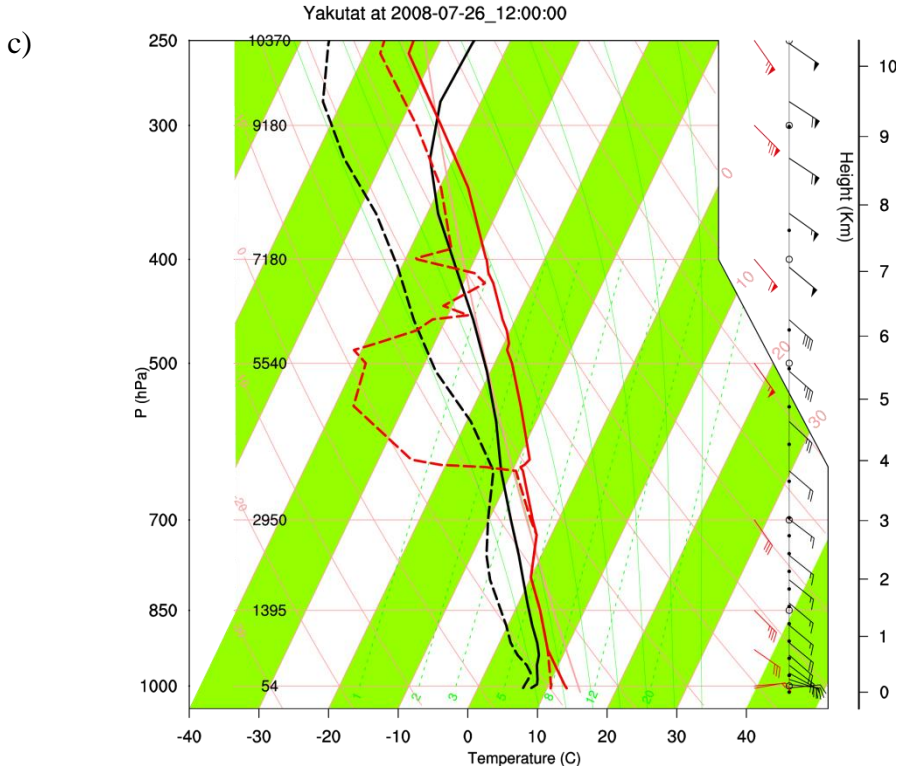
Figure 3.9 a-c Skew-T examples of a) good, b) typical, and c) poor WRF/Chem performance at Yakutat. Black wind barbs, solid, and dotted lines depict the WRF/Chem simulated wind tendency, air temperature, and dew-point temperature profiles, respectively, while the red are the actual RAOB observations from Yakutat. a) WRF/Chem reproduced the temperature, dew-point temperature, wind direction and overall vertical profile very well for 0000 UTC July 7 (1500 AST July 6), a rainy day with a low pressure system off to the northwest. b) WRF/Chem had decent performance for a calm day on 0000 UTC June 8 (1500 AST June 8), but tended to smooth some of the data. c) With a center of low pressure and rapidly changing weather conditions close to Yakutat on 1200 UTC (0300 AST) July 26, WRF/Chem showed slightly weaker performance in estimating the temperature and moisture profile, as it underestimated both.

Table 3.2 Averaged overall skill scores summarizing simulated and observed radiosonde data. The following are averaged overall statistics for temperature, dew-point temperature, wind speed and wind direction from the simulated and observed upper air profiles at Yakutat.

	Temperature (°C)	Dew Point Temperature (°C)	Wind Speed (m/s)	Wind Direction (°)
Mean WRF/Chem	-14.2	-21.1	10.12	194
Mean Radiosonde	-14.3	-21.9	10.12	198
Correlation (R)	0.85	0.60	0.69	0.66
Bias	0.1	0.8	~0	-12
Bias Min	-1.4	-6.4	-1.44	-56
Bias Max	0.8	3.5	1.18	-3
RMSE	1.8	4.6	4.13	9
RMSE Min	1.2	1.6	2.19	0
RMSE Max	2.6	11.3	8.64	20
SDE	1.8	5.0	4.21	9
SD WRF/Chem	1.8	2.2	2.41	9
SD Radiosonde	1.8	2.2	2.38	9
Min Difference	-9.6	-27.1	-32.41	-342
Max Difference	10.4	27.1	29.42	103

Table 3.3 Average height of each model level at the Yakutat radiosonde site. Radiosonde observations were interpolated to the data's corresponding levels. These values are averaged grid midpoint heights and accordingly have ranges of heights with upper and lower limits. Recall WRF/Chem uses a terrain following coordinate system, so these heights vary upon location (section 2.1.1).

WRF/Chem Level	Average Height (m)	WRF/Chem Level	Average Height (m)
1	27.3	15	5404.7
2	91.8	16	6217.4
3	179.8	17	7029.5
4	291.7	18	7840.7
5	432.5	19	8651.6
6	611.3	20	9464.6
7	830.0	21	10285.7
8	1138.2	22	11125.1
9	1524.8	23	11992.5
10	1927.7	24	12892.4
11	2348.5	25	13826.9
12	2968.8	26	14798.4
13	3779.9	27	15809.7
14	4592.0		

stable stratification. Winter in Interior Alaska entails limited sunlight, where there is less than four hours during the shortest days of the year. Thus, summer simulations avoid many of these modeling problems (see also Mölders 2008).

In Yakutat, with long hours of daylight (up to 18 hours and 48 minutes on June 20), moderate high temperatures averaging 15°C, and lower stable stratification than in Interior Alaska, WRF/Chem performs better for this summer simulation than in Mölders et al.'s (2011) during the winter season.

3.2.2 Temperature

WRF/Chem simulated the average summer temperature profiles (Fig. 3.10) best out of the four quantities recorded by the radiosonde's sensor (Table 3.2). The temperature profiles were very well correlated between simulated and observed ascents, at an average of r=0.85. The overall mean simulated profile temperature throughout the column (from surface to 12 km) was -14.2°C. The model had a very small overall warm temperature bias of 0.1 K, and low RMSE of 1.8 K. The profile was generally underestimated by -1.4 K to -0.3 K in heights less than 600 m, and then overestimated by less than 0.8 K up to the tropopause. The surface layer contained the highest bias (-1.4 K) and had the lowest correlation (r=0.68), which may be due to misrepresentation of the surface conditions. However, the modeled data followed the temporal evolution and upper air profile very consistently. The temperature data included low RMSE (1.8 K), and values remained very consistent throughout the entire profile. Temperatures decreased steadily with accordance to the normal atmospheric lapse rate of approximately 6.5 K $(km)^{-1}$. Simulated and observed variance of the radiosonde profiles agreed excellently with values of 3.1 K^2 and 3.2 K^2, respectively.

On average at Yakutat, the WRF/Chem mean temperature profile indicated a very small temperature inversion between the heights of 291.7 m and 432.5 m. The inversion is only an increase of 0.24°C over this distance, or about approximately 0.17 K $(100 m)^{-1}$ between the two levels. Although this lapse rate is very small, the corresponding radiosonde data does not indicate this minor inversion. The simulation of a non-existent inversion could be the result of parameterization errors close to the surface (e.g. see Mölders and Kramm (2010) on the misrepresentation of dominant land-use, soil type, or tropopause features, etc.). If there were

Figure 3.10 Mean WRF/Chem simulated and observed air temperature profiles, correlation (R), bias, and RMSE at Yakutat, AK from May 15 to September 15, 2008. Correlation is scaled by a factor of 10 on this plot, and the legend shows how the plotted value is converted to a traditional correlation from -1 to 1. The small gap present around 500-700 m accounts for missing radiosonde observations corresponding to the height of the 6th WRF level.

observational data for the sixth WRF/Chem level, a more accurate analysis regarding the presence of an inversion layer in the radiosonde data could be made. However, the temperature for both simulated and observed conditions rapidly decreases at a relatively steady rate after the section of missing data.

Another reason for the slight temperature inversion in the simulated data may result from the amount of inversions that were actually simulated. Considering surface inversions, where the temperature at the surface was cooler than the layer(s) above it, the model simulations had 106 ascents with inversions, compared to 97 in the observations. There were also a great number of EI's, 82 ascents, compared to 77 simulated. This difference yields a likely error of 9% for SBIs

and 7% for EIs for all 244 ascents during the 2008 tourist season. In Yakutat, SBIs (EIs) occurred on 40% (32%) of all ascents. This error of false alarm and hit rate is on par with Mölders et al.'s (2011) simulations of winter inversions in Fairbanks. The authors found 103 simulated surface inversions, compared to 97 observed, and found 22 simulated EI's, compared to 19 observed. These occurred over a 120 day simulation during the winter of 2005-2006.

One argument for a greater number of modeled surface inversions is the fact that radiosondes do not have the resolution needed to accurately capture shallow surface inversions. Also, as the radiosonde ascends, it is likely to be pushed outside of the WRF/Chem grid column used in the evaluation and continues its measurements wherever the wind blows it (McGrath et al. 2006). In addition, the veering motion of the winds observed from the surface to approximately 500 m results in warm air advection, where it particularly matches up well with increasing wind speeds up to the height of the inversion (Segele et al. 2013). A study by Levi et al. (2011) using WRF simulations and wind profilers suggest marine boundary level inversions frequently set up on coastal sites.

3.2.3 Dew-Point Temperature

The dew-point temperature profiles (Fig. 3.11) were generally simulated well in levels closest to the ground. The best correlation between simulated and observed profiles (r > 0.7) is below WRF/Chem level 14 (4592 m) and slightly drops off to around r ≈ 0.5 by 10,285 m. The tropopause is evident above this height, and WRF/Chem struggles to accurately simulate the amount of moisture as seen in the discrepancies between simulated and observed dew-point temperature profiles that exist around levels of strong wind shear. This behavior is similar to findings by Mölders et al. (2011) in simulated and observed winter upper air profiles from Fairbanks and McGrath. Wind speed steadily increased up to the tropopause, and then rapidly decelerated above 10,500 m (see next section). Another reason for radiosonde moisture errors could be brought upon by a wet sensor. When the radiosonde travels through a cloud, the sensor could get wet and skew the measurement.[1] Water vapor may also freeze on the sensor as it ascends to higher and colder altitudes. The release of latent heat during freezing warms the sensor, providing higher temperature values.

---

[1]See the following website to identify erroneous data in radiosonde profiles:
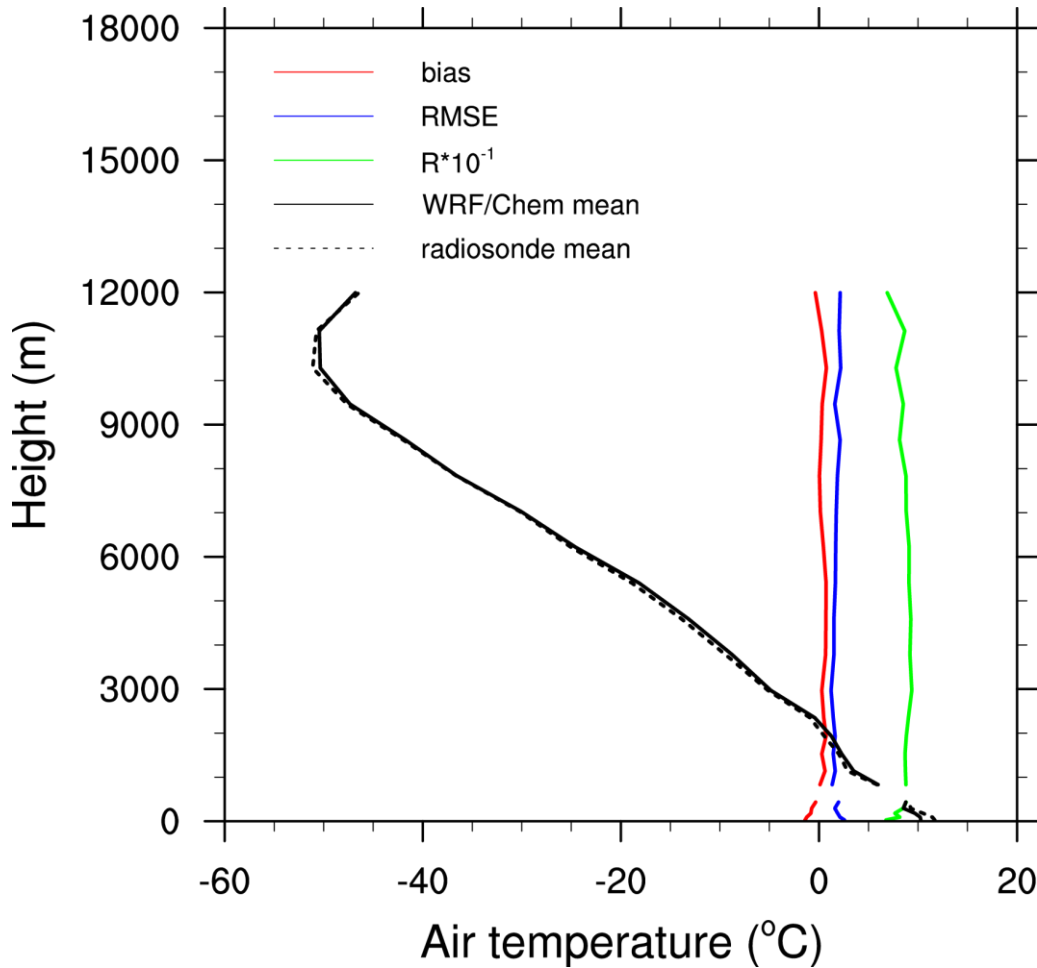http://www.ua.nws.noaa.gov/study2.htm
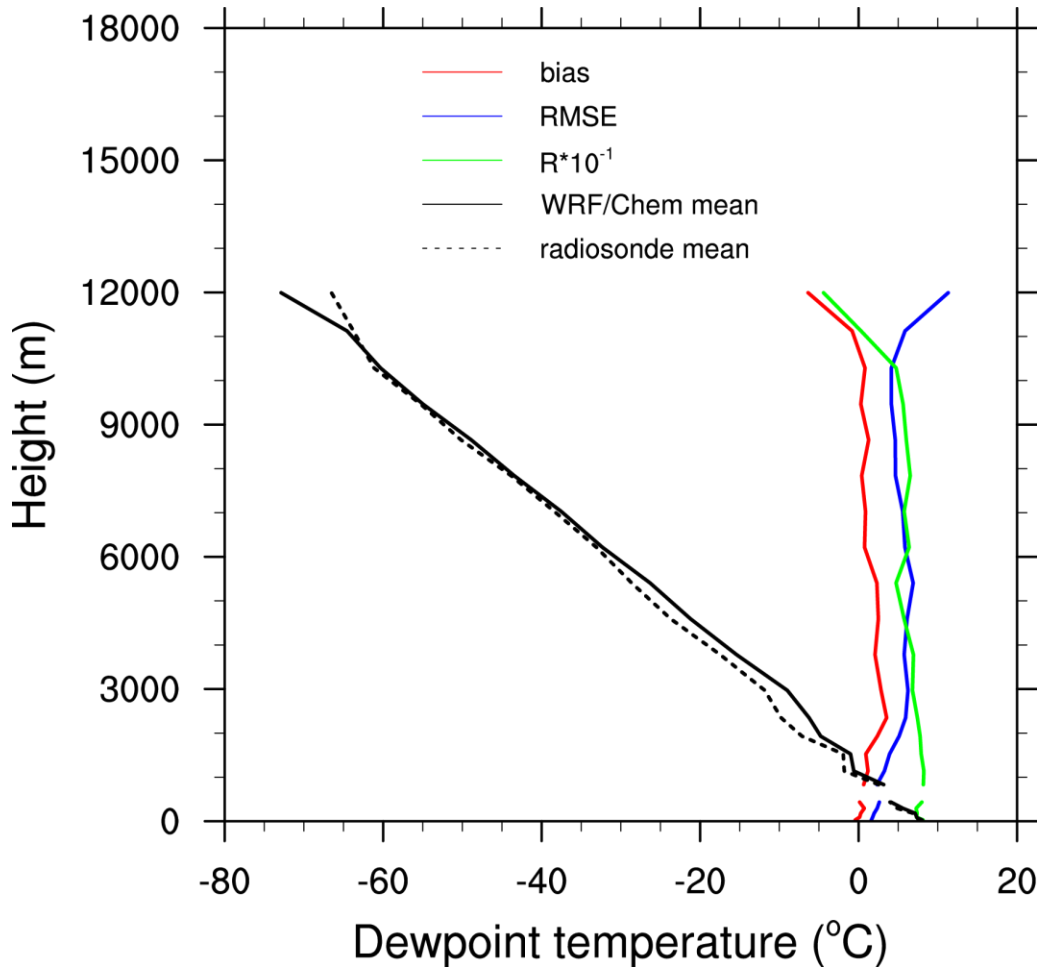
Figure 3.11 Mean WRF/Chem simulated and observed dew point temperature profiles, correlation (R), bias, and RMSE at Yakutat, AK from May 15 to September 15, 2008. Correlation is scaled by a factor of 10 on this plot, and the legend shows how the plotted value is converted to a traditional correlation from -1 to 1. The small gap present around 500-700 m accounts for missing radiosonde observations corresponding to the height of the 6th WRF level.

A region of strong wind shear is evident around 1500-3000 m when wind direction shifts rapidly between south-southeast to southwest (see next section). The model captures the dew-point trend, but slightly overestimates the actual dew-point temperatures around these levels. It tends to point towards a wet bias in this region, where conditions are actually a bit drier.

Mölders et al. (2011) also identified some variations between simulated dew-point temperature profiles around 1-3 km, as well as in the mid-troposphere. The authors attributed these discrepancies to the NCEP Final Analysis Data (FNL) used to initialize the model, since the data is potentially too coarse in vertical resolution. In addition, the low density of observation sites fails to represent many mesoscale features caused by terrain influences, as already pointed

out by PaiMazumder and Mölders (2009). There are only 14 radiosonde launching sites across the entire state of Alaska (Fig. 2.9), which is almost equivalent to the span from the East to West Coast in the Continental United States.

The average simulated dew-point temperature throughout the column was -21.9°C, leaving an overall bias of 0.8 K. WRF/Chem generally overestimated the overall dew-point temperature profile by a very slight amount. Biases ranged from 0.2 to 1.2 K in levels below 1524 m to as high as 3.6 K around levels of greater wind shear. The model had difficulties again at the tropopause, where radiosonde observations pointed to a wetter atmosphere than the model could predict. However, it is to be expected that discrepancies will exist with rapidly changing atmospheric conditions in this region. Above the tropopause, transitioning into the stratosphere, there is typically so little moisture that the sensor will have issues taking measurements. Furthermore, at these heights, the model resolution is very coarse. Variances of the model and radiosonde dew-point temperature also agreed well, with values of 4.9 K^2 and 5.0 K^2, respectively.

3.2.4 Wind Speed

WRF/Chem captured the upper air wind speed profiles (Fig. 3.12) accurately, but had some difficulties simulating wind speeds up to 2500 m. The overall wind-speed correlation between simulated and observed profiles was decent at r=0.69. Highest correlations occurred above 3000 m where there was the least amount of shear and wind speed variability. Correlations remained r ≥ 0.75 above 3000 m as wind speeds steadily increased and became more zonal up to the tropopause. The model tended to overestimate wind speeds by 0.2-1.2 m/s from the surface to about 1138.2 m (WRF/Chem level 8), and then very slightly underestimated the wind speeds above this level to the tropopause. Biases were as high as -1.4 m/s close to the tropopause, but generally less than -0.7 m/s. However, the overall mean simulated and observed wind speeds were exactly 10.1 m/s resulting in a mean bias of nearly zero. WRF/Chem simulated the wind-speed variance well at 5.80 m^2/s^2 versus the observation at 5.67 m^2/s^2. The minimum and maximum differences in wind speed, -32.41 m/s and 29.42 m/s respectively, indicates incorrect position of the jet stream's location between the simulated and observed quantities. The model may place the jet stream slightly above or below its actual location, which results in a large

difference. This error is located high in the atmosphere and does not have any impact on the wind speed results in the ABL.

Discrepancies between simulated and observed data may also be due to differences in terrain, as the radiosonde will actually drift during its ascent. It is very likely that the radiosonde will leave the modeled grid column over the site. According to Laroche and Sarrazin (2013), an average weather balloon will reach 250 hPa, or about 10,000 m at Yakutat, in about 36 minutes (2160 seconds). The height of 10 km was used since it is the approximate tropopause height at 60°N in the summer. Using the average Yakutat simulated wind speed throughout the 10 km column of approximately 9.37 m/s yields a seasonal average balloon drift of about 20.23 km during each launch. This distance is consistent with results found by Laroche and Sarrazin (2013) at that latitude. However, this is assuming the balloon gets blown in a constant direction for the entire ascent, which is usually not likely. A balloon may change direction several times in its ascent depending on the wind direction at various altitudes. Weather balloons have been known to drift as far as 200 km from their launch site (McGrath et al. 2006). Regardless, the balloon may still drift out of the 7 km^2 grid-cell and pass through three (or more) grid-cells.

The overestimation of WRF/Chem wind speeds close to the surface could also be the result of model resolution. At 7 km grid spacing, the model may have lost accuracy due to its proximity to the ocean and resultant onshore flow. The land-use category at Yakutat is classified as wooded tundra. WRF/Chem assumes the dominating land-use category is representative for the entire grid cell, which is not always true and can cause notable error (Dalu et al. 1991; Mölders et al. 1996). Even though the model is parameterized for surface layer physics and roughness length, the model still has a bias towards faster wind speeds (Zhang et al. 2009; Mölders et al. 2012).

3.2.5 Wind Direction

Regions of wind shear match well between the wind speed and wind direction plot (Fig. 3.13). The first section of mean wind shear is present around 290 m with a shift from south-southeast to southwest around 4 m/s. The wind shifts back to south-southeast just above the section of missing data around 830 m and increases to about 6 m/s. Again, the mean wind shifts back southwest around 1138m and decreases to 4 m/s. A similar pattern of mean wind shearing
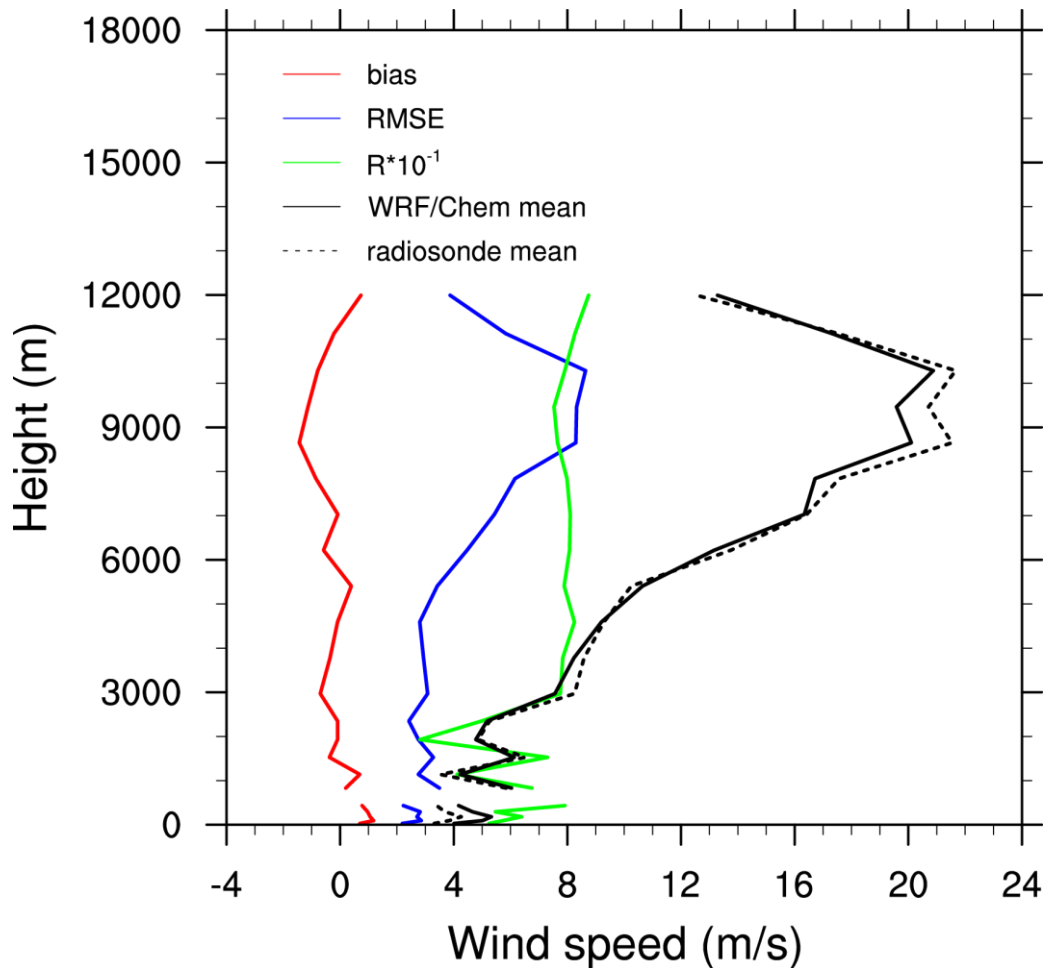
Figure 3.12 Mean WRF/Chem simulated and observed wind speed profiles, correlation (R), bias, and RMSE at Yakutat, AK from May 15 to September 15, 2008. Correlation is scaled by a factor of 10 on this plot, therefore the legend shows how the plotted value is converted to a traditional correlation from -1 to 1. The small gap present around 500-700 m accounts for missing radiosonde observations corresponding to the height of the 6th WRF level.

occurs two more times between 1500-2000 m before remaining relatively consistent for the rest of the profile.

The overall mean radiosonde-reported wind direction was 194° (south-southwest), very close to the mean WRF/Chem value of 198°. The south-southwesterly flow of the prevailing winds makes sense due to the onshore flow from the Gulf of Alaska. Most meteorological disturbances impacting Yakutat are the result of low pressure systems approaching from the ocean (Shulski and Wendler 2007). The St. Elias Mountains act as effective blocking agents, and winds from the north or northeast are not typically common, unless there is a downsloping wind event.

71
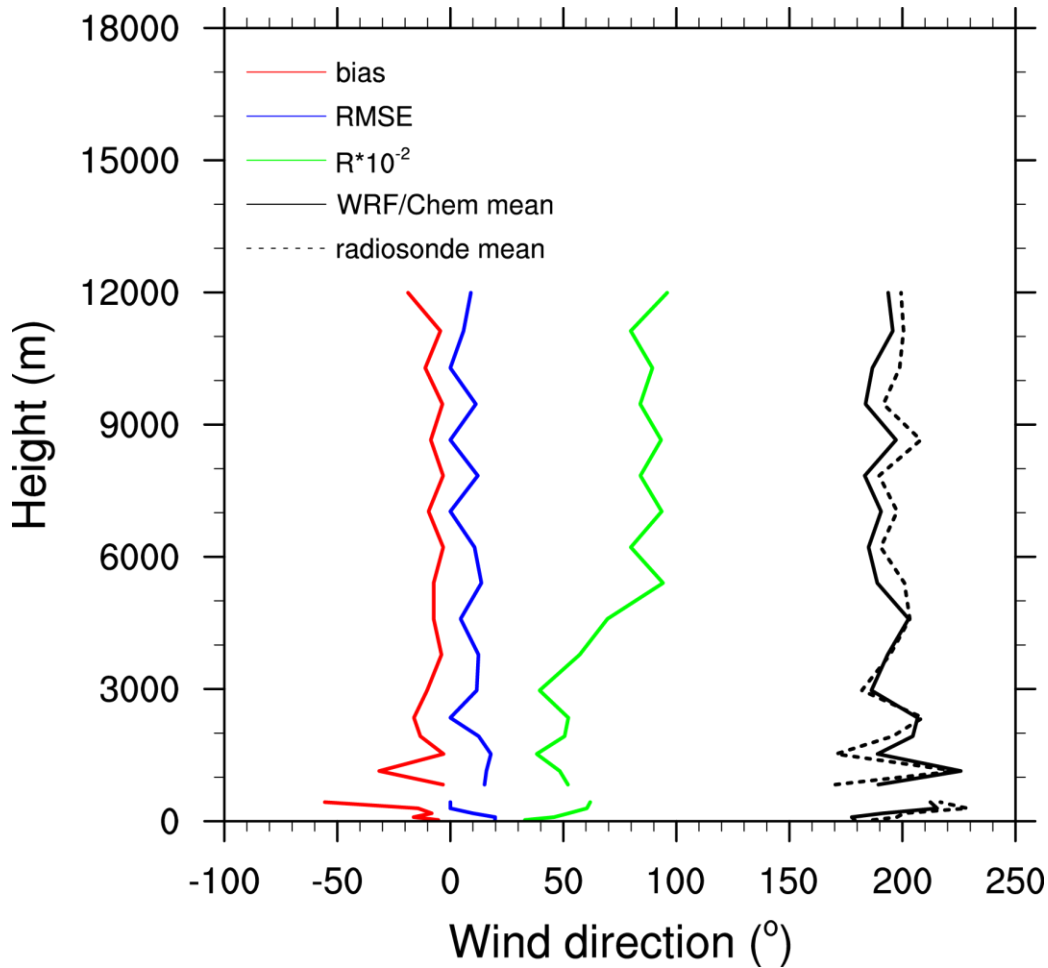
Figure 3.13 Mean WRF/Chem simulated and observed wind direction profiles, correlation (R), bias, and RMSE at Yakutat, AK from May 15 to September 15, 2008. Correlation is scaled by a factor of 100 on this plot, therefore the legend shows how the plotted value is converted to a traditional correlation from -1 to 1. The small gap present around 500-700 m accounts for missing radiosonde observations corresponding to the height of the 6th WRF level. Discontinuities with the abrupt change in wind direction from $\leq 359°$ and $\geq 1°$ were accounted for using the Mitsuta Method (Mori 1986).

The temporal evolution of simulated and observed data with respect to direction and height was good. The model responded well to wind direction changes, but the model data often fell short by a few degrees. The simulated and observed wind direction had a good correlation value of r=0.66. Areas with high wind shear and rapidly fluctuating directions were where correlation values were poor. The model tended to be biased towards lower values of wind direction, especially above 5000 m. Closer to the surface, the model tended to underestimate the wind direction by a few degrees. The wind-direction bias reached up to -56°, however the

72

average bias was only -12°. WRF/Chem was able to capture the variance in wind direction well at $84°^2$ compared to the radiosonde variance of $73°^2$.

3.3 Conclusions from the Evaluation

After comparing surface observations at 42 meteorological stations with the same WRF/Chem simulated quantities, as well an entire season of radiosonde ascents at Yakutat with the WRF/Chem profiles, it can be concluded that the model is able to reproduce meteorological conditions in Southeast Alaska well for the 2008 tourist season. Thus, the model serves as useful tool in understanding inversions in Glacier Bay where observations are non-existent.

While there are errors in the results, WRF/Chem showed a respectable performance in modeling the temporal evolution of surface meteorological fields most of the time. It tended to slightly underestimate the surface temperature and dew-point temperature by -0.6 K and -0.2 K, respectively. It slightly overestimated relative humidity (2%), wind speed (1.75 m/s), and wind direction (6°). Sea-level pressure was simulated the best, with a correlation of 0.996 (~1), although it was slightly underestimated in WRF/Chem by -0.89 hPa.

WRF/Chem seems to perform better for upper air data than for surface sites. It overestimated temperature and dew-point temperature by very small margins (0.1 K and 0.8 K, respectively). There was a very little, if any, overall wind-speed bias, and a small negative wind directional bias of -11°. Correlations tended to increase with height. WRF/Chem showed an excellent performance modeling the temperature and dew-point temperature profiles. In all cases, it was able to follow the vertical profiles of all meteorological quantities.

The sources of error are mainly due to topographical discrepancies, land-use type mismatches due to the assumption of dominant representative land-use, and boundary and/or initialization errors. As in all meteorological models, average terrain heights are used across an entire cell. As a result, terrain smoothing occurs in some regions and can skew results, especially when data is averaged in a place that is so dynamic and exposed to microscale weather events like Southeast Alaska. Regarding the radiosonde data, a wet sensor and/or balloon drift can skew observations.

As with any simulation or model, results are not perfect and some errors will always exist. However, the model serves as an excellent tool to understand atmospheric processes that we cannot otherwise quantify. WRF/Chem has proven to be able to simulate surface and upper

air meteorological parameters to a decent accuracy, or better. Therefore, these model simulations can be used to further determine the occurrence and climatology of inversions, the impacts of ship emissions on accumulations of particles trapped under inversions in Glacier Bay, as well as their frequency, formation, and depletion mechanisms.

Chapter 4 Results of the Inversion and Particulate Matter Analysis

The following chapter outlines the synoptic situations during the 2008 cruise-ship season, discusses WRF/Chem modeled inversions throughout Glacier Bay, and assesses particulate matter (PM_{10}) concentrations in Glacier Bay produced in response to cruise-ship emissions.

4.1 Synoptic Situation and Comparison to Climate

Surface analysis charts were gathered from the National Weather Service, courtesy of the Anchorage Weather Forecast Office (WFO). The NCEP/Marine Prediction Center (MPC) issues four daily surface products (0000, 0600, 1200, and 1800 UTC) that show the best projection of Alaska, Northwest Canada, and much of the Northern Pacific Ocean. In addition, plots were gathered from the NWS/NCEP Ocean Prediction Center (OPC) that display most of the Eastern Pacific Ocean and coastlines extending from California to Alaska.

Southeast Alaska is exposed to maritime influences, where frequent storm systems track from west to east across the Gulf of Alaska. These disturbances keep the climate moist and air temperatures moderate. The state's highest yearly precipitation totals are located at points along the Alaska Coastal Ranges, where skies can be cloudy for approximately 70% of the year (Shulski and Wendler 2007). Due to the mountainous topography, weather conditions and prevailing flow may vary substantially, even in areas that are in close proximity to each other (Shulski and Wendler 2007). This difference can be attributed to elevation, or leeward and windward topographical effects caused by orographic lifting. Onshore winds force air to rise over the extensive coastal mountain chain, which can exceed 5,000 m in some locations. Air cools as it rises, and then condenses to form clouds.

Fall through early spring (September through about March) is generally the most active period of time for low-pressure systems in Southeast Alaska, and corresponds to the largest recorded precipitation totals. September and October are the months with the highest precipitation in Juneau. One reason for this higher precipitation is the stronger temperature contrasts between the atmosphere and ocean. Ocean sea-surface temperatures (SSTs) are still low at the end of spring (about 7°C at the beginning of May) due to the melting of sea ice and overall cold winter temperatures. Water has a higher heat capacity than the air, so it takes longer for the SST to increase than air temperature. As a result, SSTs increase to about 14°C by August. Higher

temperatures induce the evaporation of water, which can result in cloud formation and precipitation. The active weather pattern in the North Pacific is related to the semi-permanent Aleutian low, which acts as a region of intensification for storms affecting southern Alaska coastlines (Shulski and Wendler 2007). During the late spring and early summer, low-pressure systems are present, but are typically weaker than their fall counterparts. The Aleutian low significantly weakens or is not present during the summer months, and may be replaced with high pressure events due to the larger temperature contrast between land and sea (Shulski and Wendler 2007). In addition, the subtropical high usually expands northward.

In the broad scheme (compared to the 30 year climatological average of 1981-2010), 2008 experienced a generally typical summer season (Table 4.1). Overall temperatures were slightly lower than normal, and precipitation was a bit higher than usual. The average daily mean temperature was approximately 2 K cooler for June and July, but generally equivalent (around one degree or less) for the remainder of the summer. High and low temperatures were lower than normal, with the exception of the September average low, which was less than 1 K higher than normal. Precipitation values were also generally on average for May and August. June experienced almost half of the normal monthly precipitation than it usually receives, with a deficit of 39 mm. July received nearly double the average rainfall, with 93 mm above normal. September was also 57 mm wetter than average.

Table 4.1 Thirty year average (1981-2010) and 2008 average monthly temperatures and precipitation at Juneau International Airport (PAJN). Blue (pink) shaded boxes indicate that the 2008 monthly temperature was cooler (warmer) than the 30 year average. Green (orange) shaded boxes indicate that the monthly precipitation was higher (lower) than the 30 year average.

Month	30 yr Mean High Temp (°C)	2008 Mean High Temp (°C)	30 yr Mean Low Temp (°C)	2008 Mean Low Temp (°C)	30 yr Daily Mean Temp (°C)	2008 Daily Mean Temp (°C)	30 yr Mean Precip (mm)	2008 Mean Precip (mm)
May	13.7	13.5	4.8	4.3	9.2	8.9	86	99
June	16.8	14.4	8.3	6.6	12.6	10.5	82	43
July	17.7	14.4	10.0	9.1	13.8	11.8	117	210
August	17.1	15.0	9.4	9.2	13.3	12.1	146	135
Sept	13.2	12.0	6.9	7.5	10.0	9.7	219	276
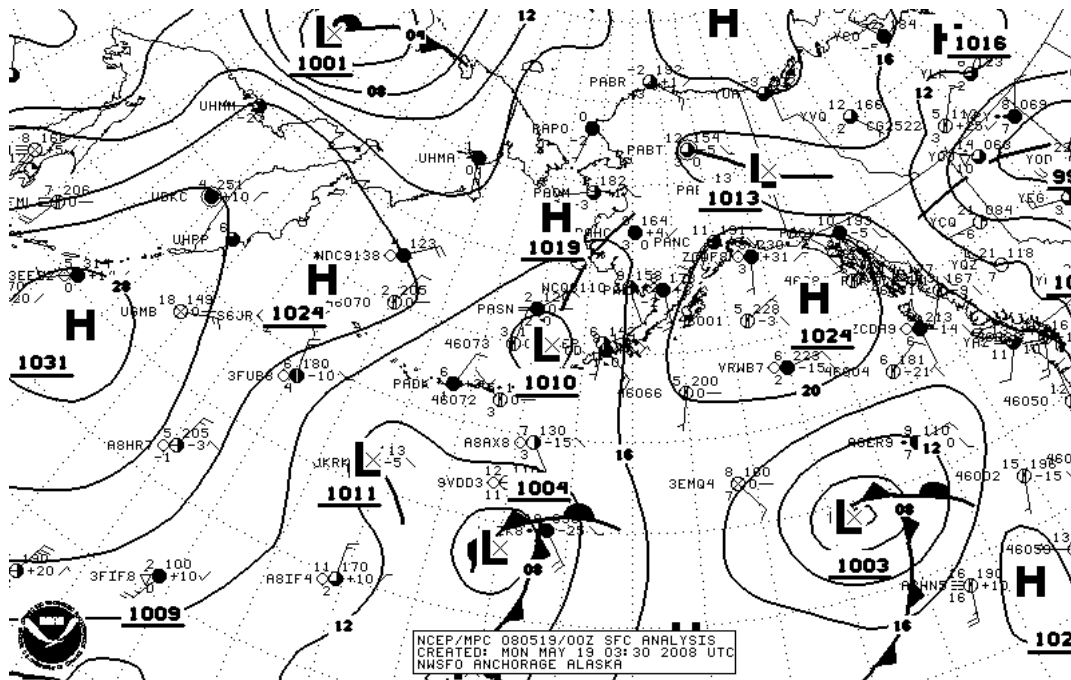
Figure 4.1 Synoptic chart from 0000 UTC May 19, 2008 (1500 AST May 18, 2008). A 1024 hPa high pressure system dominated in the Gulf of Alaska, resulting in calm conditions and inversions. All low pressure systems were relatively weak this time of the year.

The period of study began on May 15, 2008 with a 967 hPa occluded low-pressure system in the Gulf of Alaska centered south of Kodiak Island. Southeast Alaska was located along the cold frontal zone, so the storm likely brought cloudy skies and precipitation. The storm dissipated as it moved inland towards South Central Alaska by the following day. A deep 1033 hPa high slid further northward from Victoria Island and kept weather quiet until early in the day on May 19 (Fig. 4.1). A weak low (996 hPa) drifted into the southern part of the Panhandle on May 19-20, but appeared to stay distant from Glacier Bay. The remaining part of May was generally clear, with dominant high pressure in place until June 2. Due to the relatively clear nature of the start of the 2008 tourist season, Glacier Bay likely received clear skies and calm winds, which are favorable conditions for inversions to develop. As a result, WRF/Chem did simulate a notable number of inversions during the first 18 days of the study period.

Conditions remained clear until June 3 when a 985 hPa low tracked over the Gulf of Alaska. However, the low moved north and dissipated over Prince William Sound, but likely brought precipitation to Southeast Alaska along the storm's frontal zone. Conditions cleared by June 4-6, and then a weak low tracked into the northern Gulf of Alaska. The storm appeared to be blocked by the Coastal Ranges, where it stalled until dissipation on June 9. The next few days

included two weak lows that tracked to the south of the Alaska Panhandle as they dissipated. High pressure built from June 17-21 until a series of two small storms tracked over the north Pacific. Skies cleared and high pressure dominated again from June 29 through July 4 (Fig. 4.2). June saw a low accumulation of rain in Juneau (almost half the normal), and even though there were several storms, most were weak and likely brought more cloudiness than precipitation. Many storms tracked to the south of Glacier Bay, and the coastal mountains acted as successful blocking obstacles.
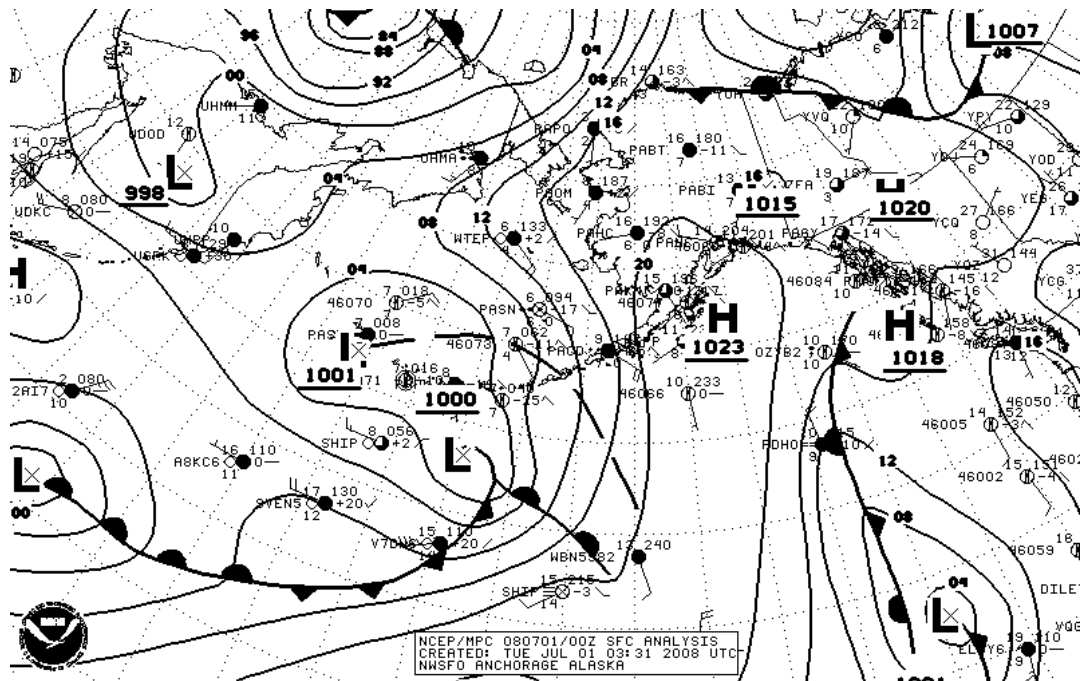
Figure 4.2 Synoptic chart from 0000 UTC July 1, 2008 (1500 AST June 30, 2008). A series of high pressure systems over Southern Alaska and the Gulf of Alaska resulted in calm conditions and inversions. This surface map shows another example of favorable synoptic conditions for inversions in Glacier Bay.

Climatologically, July was cooler and wetter than normal. The month began quiet until a 991 hPa storm tracked northeastward from the North Pacific on July 5 and lingered until dissipation, which likely brought rain. High pressure built July 10-12 until another small low tracked into the area and weakened. Much of the North Pacific saw a dominant high pressure system from July 14-17, but it was forced southeast by an advancing 997 hPa low, which developed off the Eastern Aleutians, strengthened, and finally impacted Southeast Alaska by July 19. After dissipation, ridging developed, and conditions stayed clear until July 24. A 999 hPa

low arrived by July 28, becoming trapped by the topography until it dissolved, and set the stage for a clear early August.
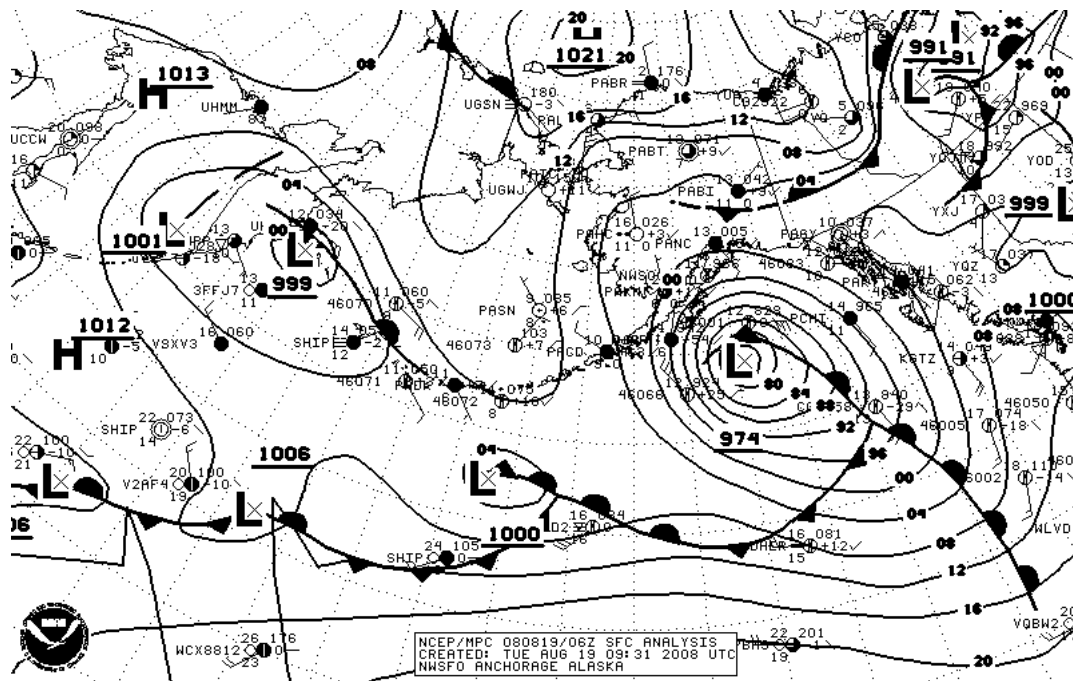
Figure 4.3 Synoptic chart from 0600 UTC August 19, 2008 (2100 AST August 18, 2008). While there was a relatively strong 974 hPa low over the Gulf of Alaska, station plots near Glacier Bay registered calm winds and clear skies. Interestingly, this period, along with the subsequent two days, resulted in many modeled inversions. Even though there was a storm in the vicinity, this example demonstrates the fact that topography strongly controls local scale weather. The storm missed Glacier Bay entirely as it drifted to the southeast and eventually degenerated as it reached coastal British Columbia.

Aside from a few minor shortwave troughs, July 30 to August 11 was very quiet and dominated by calm weather. As a result, there were modeled inversions in early August. However, the calm pattern broke by August 12 with a 994 hPa closed low tracking eastward from the North Atlantic. The weaker storm was followed by the first larger autumn low of the year. A 979 hPa low developed off the Aleutians and strengthened, bringing stormy weather until dissipation on August 14. Quiet, high pressure began building until August 18 with the presence of another strong Aleutian Low (Fig. 4.3). The latter portion of August remained unsettled as a series of frontal systems tracked from the Aleutians towards Victoria Island. Beginning in mid-August, it is evident that a more active weather pattern was setting up for the Panhandle. The

Aleutian Low spawned new storms every few days bringing rain that increased monthly precipitation averages.
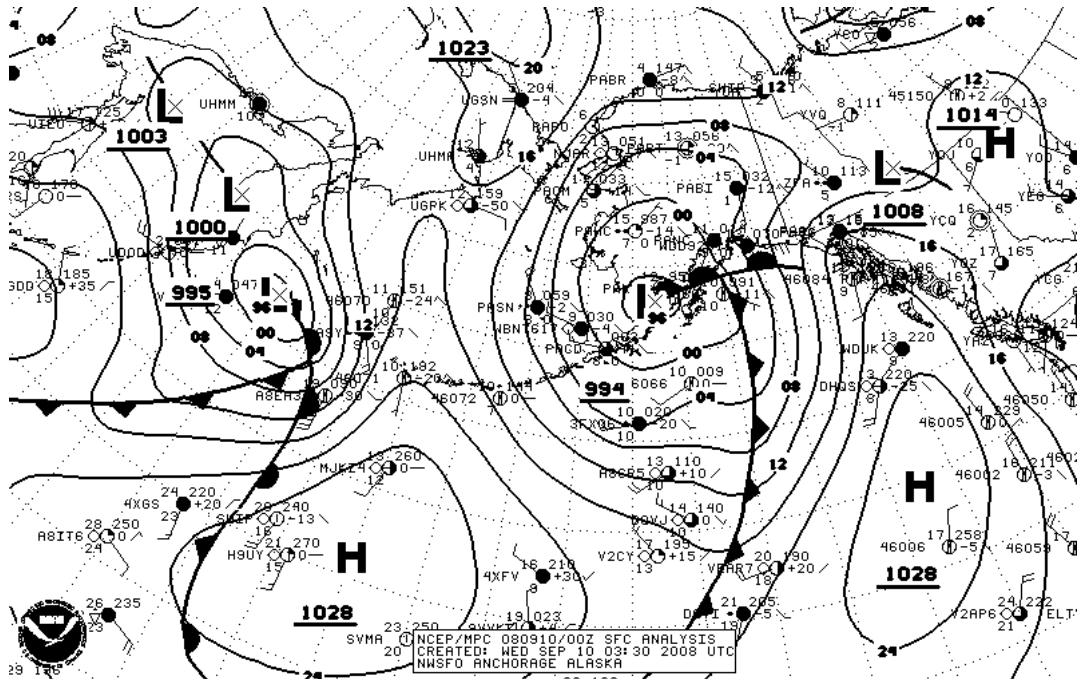
Figure 4.4 Synoptic chart from 0000 UTC September 9, 2008 (1500 AST September 10, 2008). This example shows the increased strength and frequency associated with low pressure storms later in the tourist season. Onshore winds with counterclockwise flow around the storm were likely enough to create turbulent conditions inside the fjords of Glacier Bay and prevent the formation of inversions.

As the tourist season came to a close, the first seven days of September experienced calmer weather and some weak high pressure. On September 9, a new 986 hPa low developed and tracked inland over southwest Alaska, bringing rain to the southeast along a cold front (Fig. 4.4). A similar situation developed as the tourist season ended on September 15. September was the second wettest month in 2008 (aside from October), and it is clear that storms gained intensity and prevalence towards the end of the study period. With that in mind, September generally experienced a small number of inversions inside Glacier Bay.

4.2 Inversion Analysis

The following section discusses the modeled WRF/Chem inversions for the 27 grid-cells in Glacier Bay. Inversion occurrence, quantity, strength, frequency, and mechanisms are discussed. Four individual case studies are also presented for representative points in Glacier

Bay. In addition, the relationship between concentrations of PM_{10} is linked to the inversions and their prevalence, as ship emissions may become trapped if an inversion is present.

4.2.1 Inversion Statistics

All simulated inversions less than 0.5 K $(100 \text{ m})^{-1}$ were eliminated from this analysis, as they were too weak to make reasonable conclusions. Thus, after reducing the dataset, we were left with 9796 instances of inversions that were stronger than $\geq$ 0.5 K $(100 \text{ m})^{-1}$. This value contains all of the inversions over 2976 hours of the tourist season, (124 days times 24 hours a day), and over all 27 grid-cells in the Glacier Bay. Thus, an inversion could be present for each hour of the tourist season over all grid-cells in Glacier Bay. Most of the inversions fell within a weak range, with 5206 from 0.5 K $(100 \text{ m})^{-1}$ to < 1 K $(100 \text{ m})^{-1}$. There were 3430 moderate inversions from 1 K $(100 \text{ m})^{-1}$ to < 2 K $(100 \text{ m})^{-1}$. Finally, there were 1160 strong inversions greater than 2 K $(100 \text{ m})^{-1}$.

In section 3.2.2, WRF/Chem simulated surface based inversions, SBIs (elevated inversions; EIs) on 40% (32%) of all 244 ascents at Yakutat. The model overestimated (underestimated) SBIs (EIs) by 9% (7%). Thus, we can conclude for Glacier Bay that this inversion prediction accuracy may be on par with those in Yakutat, with a likely overestimation in low level inversions by less than 10%. These values are also on par with what Mölders et al. (2011) found in Interior Alaska. (See section 1.2 for definitions of SBIs and EIs).

There were instances of inversions throughout the 27 grid-cells from 23 to 85 days of the 124 day tourist season. Inversions occurred on average 52 days across the entire bay. The average inversion height and strength across the bay was 92.5 m and 1.19 K $(100 \text{ m})^{-1}$, respectively. The strongest inversions of 6.7 K $(100 \text{ m})^{-1}$ occurred in grid-cell 54-50 (throughout this chapter, grid-cells will be identified by their specific coordinates in the WRF/Chem model domain for simplicity; see Fig. 4.6 or 4.7 for their locations), which is located towards the entrance of Glacier Bay. It occurred on 2200 UTC (1300 AST) May 24. The inversion remained stronger than 5.7 K $(100 \text{ m})^{-1}$ at a height of 64.4 m from 1900 UTC to 0000 UTC May 25 (1000-1500 AST). This location also had the highest average inversion strength throughout the tourist season of 1.63 K $(100 \text{ m})^{-1}$. The lowest average inversion strength of 0.86 K $(100 \text{ m})^{-1}$ occurred in Muir Inlet at grid-point 60-49.

These results are consistent with a study by Benson et al. (1978), who took observations in Goose Cove and Muir Inlet over two summers in 1976-1977. Through direct observations via thermograph and balloon launches, the authors concluded thermal mixing was minimal, and inversions, with gradients as great as 2.5 to 3 K (100 m)$^{-1}$ were present in the first 100 to 200 m. Through these results, it was evident that Glacier Bay's tolerance for pollution was extremely low. During the period of June 13 to July 21, Benson et al. (1978) concluded inversions occurred on at least one-third of all days. During the same 39 day period in this study, inversions were present throughout Glacier Bay on average of 46% of all days. The average number of inversion days across all grid-cells during the 124 day tourist season in this study was 52 days, or 42%. Inversion days occurred from 23 days in some grid-cells, to up to 85 days in others, resulting in inversions occurring from 19% to 69% of all days, respectively.

Table 4.2 Number of modeled inversion hours by strength per month over the twenty seven grid-cells of Glacier Bay.

Month	Number of days in month for which simulated data exist	Weak 0.5 to < 1 K (100 m)$^{-1}$	Moderate 1 to < 2 K (100 m)$^{-1}$	Strong ≥ 2 K (100 m)$^{-1}$	Total number of simulated inversions
May	17	1682	1304	612	3598
June	30	860	533	82	1475
July	31	1208	743	239	2190
August	31	1229	734	190	2153
September	15	227	116	37	380
	124	5206	3430	1160	9796

Approximately 62% of the simulated inversions occurred between 2100 AST to 0700 AST (Fig. 4.5a). Inversion frequency began to increase around 1700 AST since the radiation balance may start to change as the sun's angle shifts behind steep mountains. In addition, the sun is already quite low in the sky at these latitudes. Radiation inversions are common in the nighttime and morning hours when outgoing longwave radiation exceeds incoming solar radiation. Most of the inversions were shallow and very close to the surface (Fig. 4.5b). More than 80% of the inversions occurred at the lowest WRF/Chem level, which is approximately 64 m in thickness. No inversions occurred above the seventh WRF/Chem level of approximately 1,100 m.

The month with the most inversion occurrences was May (see Table 4.2). Note that we only considered the second half of May (seventeen days), as the tourist season typically does not start until then. During this time, weather conditions were calm and favorable for inversions to develop. The number of inversions was relatively similar in July and August, with 2190 and 2153, respectively. As storm systems became stronger and more apparent by the end of the tourist season, inversions rarely occurred. September (only 15 days) saw the least amount, at 380.

Strong inversions show the propensity to significantly trap cruise ship emissions, and the implications associated with pollution in Glacier Bay is highly contingent upon these inversions. Table 4.3 displays the approximate number of days of the tourist season with strong inversions present at each grid cell. It also shows the percentage of all inversions over the entire tourist season classified as strong (≥ 2 K $(100$ m$)^{-1}$). On average throughout Glacier Bay, WRF/Chem simulated 9 days with strong inversions; however this value was up to 26 days in some locations. On average, approximately 9.2% of all inversions were strong classified as strong, with some locations up to 27%.

Table 4.3 Days of the 124 day tourist season with strong inversions occurring in each grid cell, as well as the percentage of the inversions in that grid cell that are classified as strong.

Grid Cell	Days of the season with strong inversions	Percent of all inversions that are **strong** (%)	Grid Cell	Days of the season with strong inversions	Percent of all inversions that are **strong** (%)
53,49	18	17	58,48	3	4
54,49	13	12	58,49	3	3
54,50	26	27	59,45	6	4
55,49	17	14	59,46	5	9
55,50	23	21	59,48	3	6
56,48	1	4	60,44	2	2
56,49	22	14	60,45	3	7
56,50	18	13	60,48	2	2
57,46	16	13	60,49	1	1
57,47	5	10	61,42	1	1
57,48	12	12	61,43	1	5
57,49	11	14	61,44	12	19
58,46	3	4	61,48	4	8
58,47	3	3	Bay Ave:	8.7	9.2
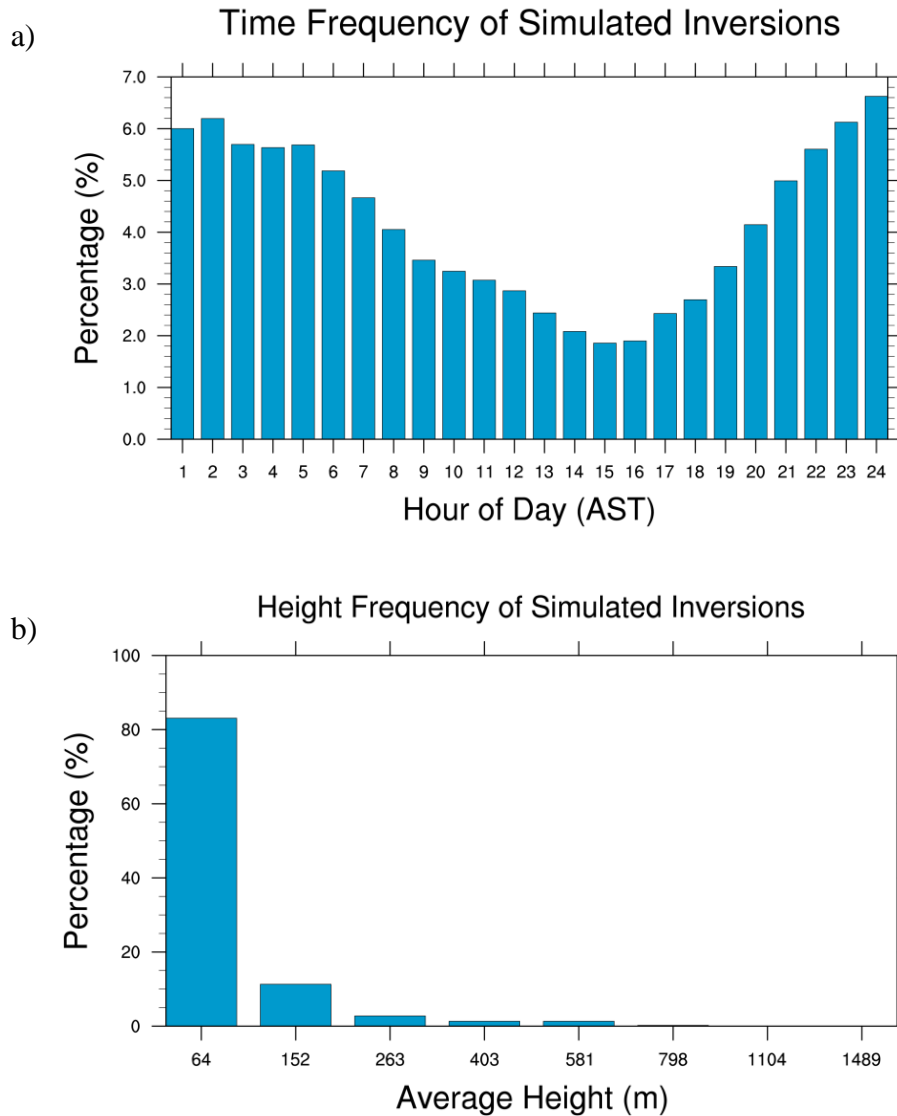
Figure 4.5 a) Temporal frequency of simulated inversions throughout Glacier Bay, and b) frequency of simulated inversion height.

The frequency of modeled inversions was generally not consistent in all locations inside Glacier Bay. In fact, areas that showed the most inversions were located towards the entrance of the park, as well as halfway through the bay, with about 60-85 days with inversions present out of the 124 day tourist season (Fig 4.6). Inversion frequency dropped in the upper reaches of Glacier Bay since the inlets are narrower, and more complex terrain surrounds the water. The variation in inversion frequency may be due the way the model analyzes topography. It may more accurately predict conditions where Glacier Bay is the widest due to more uniform surfaces

away from the presence of steep slopes. It may also be the cause of topographically related microscale weather events influenced from neighboring grid-cells.

WRF/Chem simulated the least amount of inversions where Glacier Bay was narrowest, especially in Muir Inlet towards the northeast fork, where the transition between steep mountain slopes and sea is very fast. The actual width of Muir Inlet is approximately 6 km towards the entrance and drops well under 3 km further inside. While the inlet is actually sub-grid scale, water is still the dominant land-use type.

Fig. 4.6 shows the modeled grid-cells and the approximate number of days inversions occurred throughout the tourist season. Inversions occurred most frequently in grid-cells 57-46, located approximately halfway through the bay near the entrance of Geike Inlet, and 56-49, near the middle of the bay north of Willoughby Island. For size comparisons, Glacier Bay is approximately 8 km wide at the entrance, but expands to well over 22 km in width in the middle of the water body near Geike Inlet.

Number of Days with Inversions By Grid Cell
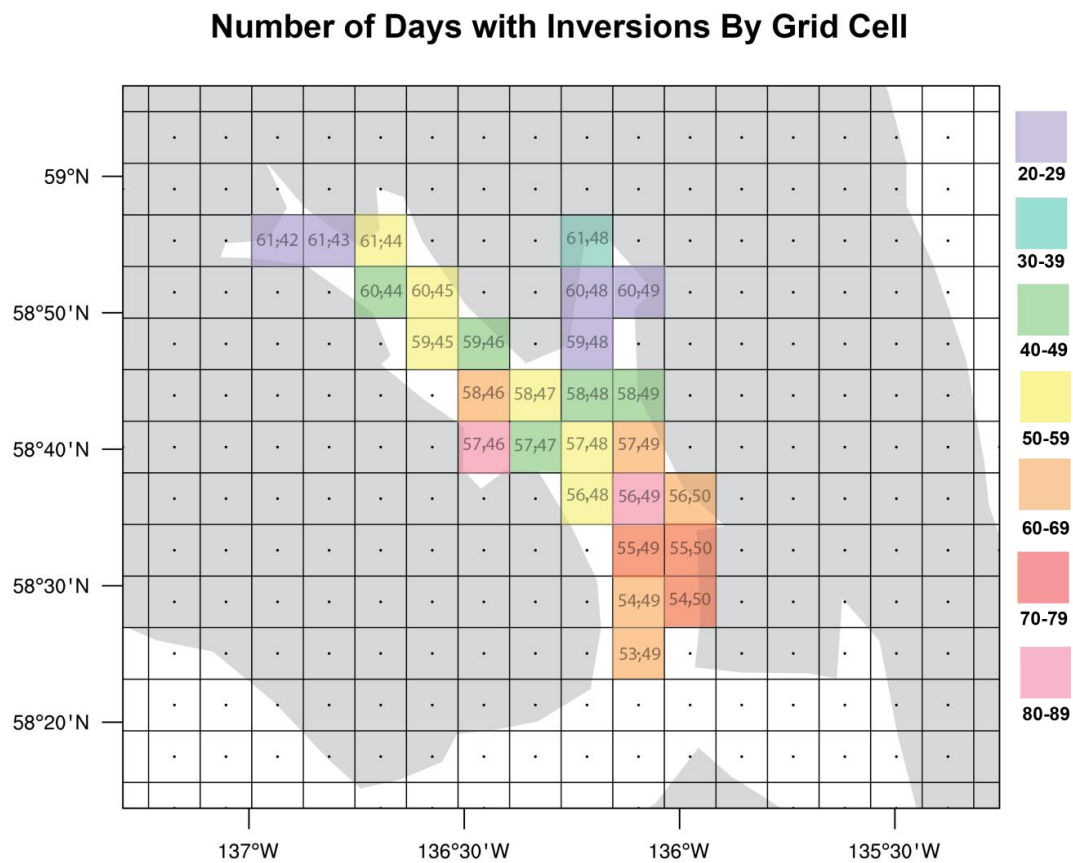
Figure 4.6 Approximate number of days with inversions in each of the 27 grid-cells overlaid on a zoomed in plot of Glacier Bay, as simulated by WRF/Chem during the 2008 tourist season.

Figure 4.7 WRF/Chem grid-cells in Glacier Bay plotted with modeled terrain heights. The red triangle is the Bartlett Cove buoy and the black dot is the Gustavus meteorology site. The terrain heights do not exactly match the coastlines as it is an artifact with the plotting program. Each grid-cell has a modeled terrain height, and the height contours become smoothed when plotted. Nonetheless, each identified cell's land-use type is water at sea-level. The red circles indicate grid-cells selected for further analysis. The red line is the region of PM_{10} cross-sections shown in later figures.

4.2.2 Inversion Case Studies

We have decided to pinpoint four grid-cells (54-50, 57-46, 60-49, and 61-44) for specific analyses (Fig. 4.7), as there are some differences between them. By choosing these four grid-cells, we get an idea of the frequency and strength of inversions at four main locations inside Glacier Bay, as reporting for each grid-cell would be impractical and often redundant. The chosen points also provide a representative analysis of different areas inside Glacier Bay.

We decided to choose 54-50 because of its location at the entrance of Glacier Bay, and also because it contained the highest average inversion strength. 57-46 was chosen because it is located in the central region of the Bay, and also had the second highest number of days with inversions (80) throughout the study period. The third location, 60-49, was chosen because it is located in the northeast fork of Glacier Bay, and also contained one of the lowest inversion frequencies, at 26 days. The final grid-point, 61-44, was selected because of its location in the northwest fork of Glacier Bay. This area is a popular region for cruise-ship traffic while viewing the Grand Pacific, Margerie, or John Hopkins Glacier. This location also showed more modeled inversion activity than its surrounding grid-cells. The average inversion length for the entire tourist season at each of these four locations: 54-50, 57-46, 60-49, and 61-44 was approximately 9.1, 8.6, 8.3, and 9.8 hours, respectively. Note that the average inversion length throughout the entire bay was 9.0 hours.

When examining the temporal evolution of the inversions over the season, there were three main modeled inversion episodes that WRF/Chem simulated throughout all grid-cells in Glacier Bay. Case #1 consisted of the period between May 18 and May 28. Sporadic inversions existed during these ten days. Case #2 occurred between June 30 and July 3, and Case #3 spanned August 19 to 20.

The percentage of inversion occurrence throughout Glacier Bay for the entire tourist season is plotted on the Hovmöller plot in Fig. 4.8. The three inversion events can also be identified in the Hovmöller plots for the individual grid cells in Fig. 4.9 a-d. While there are more inversions at cell 54-50 (a), the cell 60-49 (d) shows that inversions are basically limited to these three events. Hovmöller diagrams, while commonly used to plot meteorological data by latitude or longitude, are particularly useful in depicting the temporal evolution of inversion occurrence and height. The x-axis is the hour of day, from 0100-2400 UTC, while the y-axis

counts the day-number of the tourist season from 1-124. For example, day 50 would correspond to July 3, which is 50 days from May 15.

The first inversion event occurred between May 18 and May 28. The first few days of the tourist season were meteorologically quiet, as a series of highs and weak lows impacted further south and east of Glacier Bay. The larger period, rather than a specific inversion occurrence, was of particular focus since this span of days was one of the most active inversion periods of the season. On 0000 UTC May 19 (1500 AST May 18) (Fig. 4.1), a 1024 hPa high pressure system was present over the Gulf of Alaska and slowly drifted further north and west by the following day. Inversions developed for the first time in the 2008 tourist season in most grid-cells throughout the bay (25 of the 27 grid-cells). With the exception of 60-49, it can be seen on Fig. 4.9 a-d that the inversion lasted for most of May 18 into the entirety of May 19 (days 5 and 6).
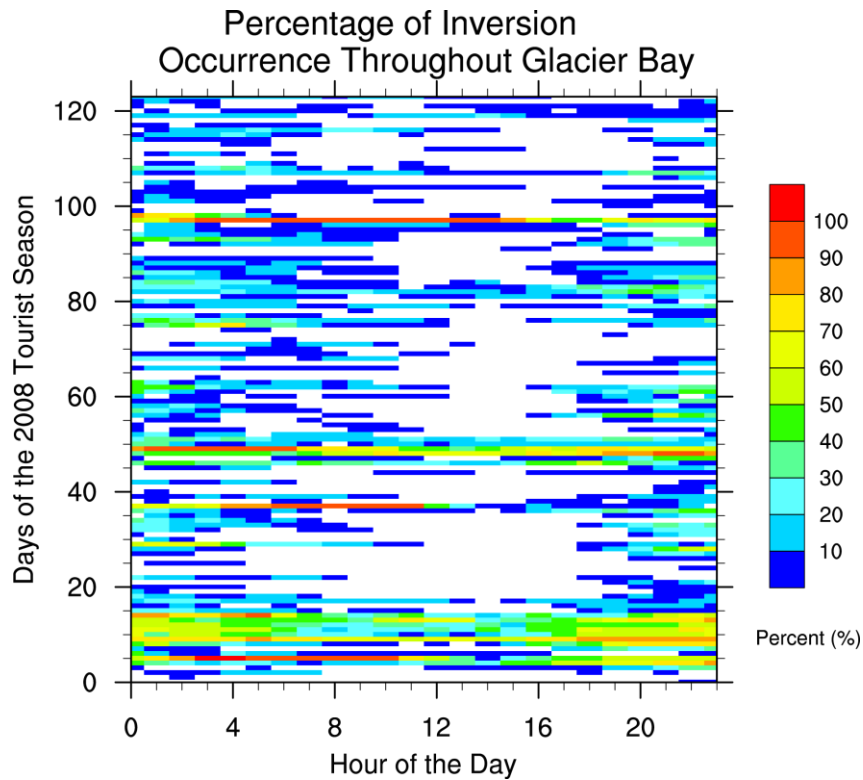

Figure 4.8 Hovmöller diagram with the percentage of modeled inversion occurrence and frequency throughout the entire tourist season in Glacier Bay. There were spatial variations of inversion occurrence over the 27 grid cells. The warmer colors on this plot indicate episodes of inversions that were common in most locations of the bay.

The station plot on the surface analysis in Haines, about 70 km northeast of Glacier Bay, showed clear skies and calm winds. By May 20, a weak low passed to the south and east of Juneau, but increased the wind speed to around 5 knots in Haines, to up to 20 knots later in the day. This wind was likely enough to create enough instability for the inversion to decompose for a short period of time on May 20 and May 21. Besides a few minor disturbances, high pressure remained in place from May 23 until May 28. As mentioned earlier, the strongest inversion event occurred from May 24 to May 25 until a cold front increased wind speeds to around 5-10 knots. For pollution concerns (as discussed later), only one ship entered the park during these two days.

Towards the entrance of Glacier Bay, a period of about ten hours of wind was enough to weaken the inversion. However, the inversion quickly redeveloped as winds reduced, and another high began developing over the Gulf of Alaska. By May 27, inversions were present. Two ships entered the park, while three others were in the vicinity or passed by Glacier Bay in Icy Strait. From May 18-28, the mean inversion strength and height over Glacier Bay was 1.34 K $(100 \text{ m})^{-1}$ and 91.7 m, respectively. While the inversions stayed present for an entire day or more in most locations (Fig 4.9a-d), inversions occurring from 0400-1500 UTC (1900-0600 AST) showed abundance, which points towards radiative cooling as their cause.

Numerous inversions were present for the period of time between the first and second studies, but none lasted for more than a day. June 20-21 had several inversions with strengths above 3-4 K $(100 \text{ m})^{-1}$ in some grid-cells, but the inversions did not occur everywhere throughout the bay. The next case study event (June 30-July 3) was chosen due to the impressive quasi-multi-day inversion presence practically throughout the entire park. Especially visible in the Hovmöller diagram at grid-point 54-50, a consistent four-day inversion pattern exists with slight breaks in the inversion on July 2 0100-1000 UTC (1600-0100 AST). The surface analyses clearly show a dominant 1023 hPa high located directly over and stalled in the Gulf of Alaska (Fig 4.2). Then, high pressure shifted slightly towards the south as a weak shortwave trough moved through Interior Alaska and Yukon Territory. Wind speed increased to 10 knots, and skies became cloudy for a brief period on July 2 at 0000 UTC (1500 AST), which is why the inversion may have broken for a few hours. However, the inversion quickly reestablished itself, lasting until early in July 4 when a new low pressure system broke the quiet pattern.

Inversions developed during this case since conditions were extremely favorable for their formation. WRF/Chem was able to predict the presence of these inversions. The mean inversion

Modeled Inversion Height at Grid Point 54-50

a)

Modeled Inversion Height at Grid Point 57-46

b)

Modeled Inversion Height at Grid Point 61-44

c)

Modeled Inversion Height at Grid Point 60-49

d)
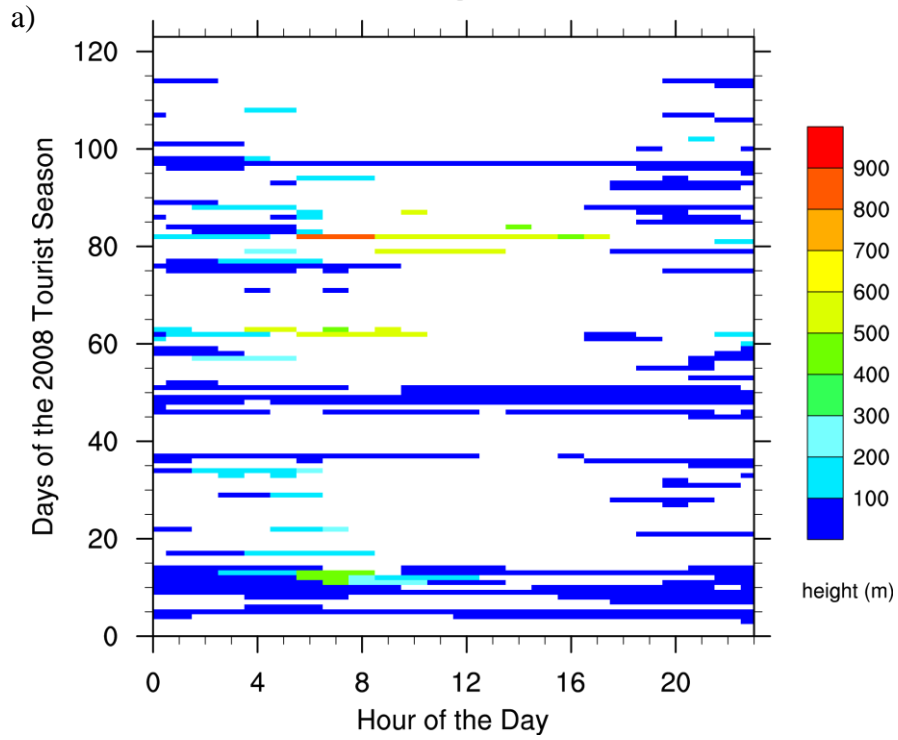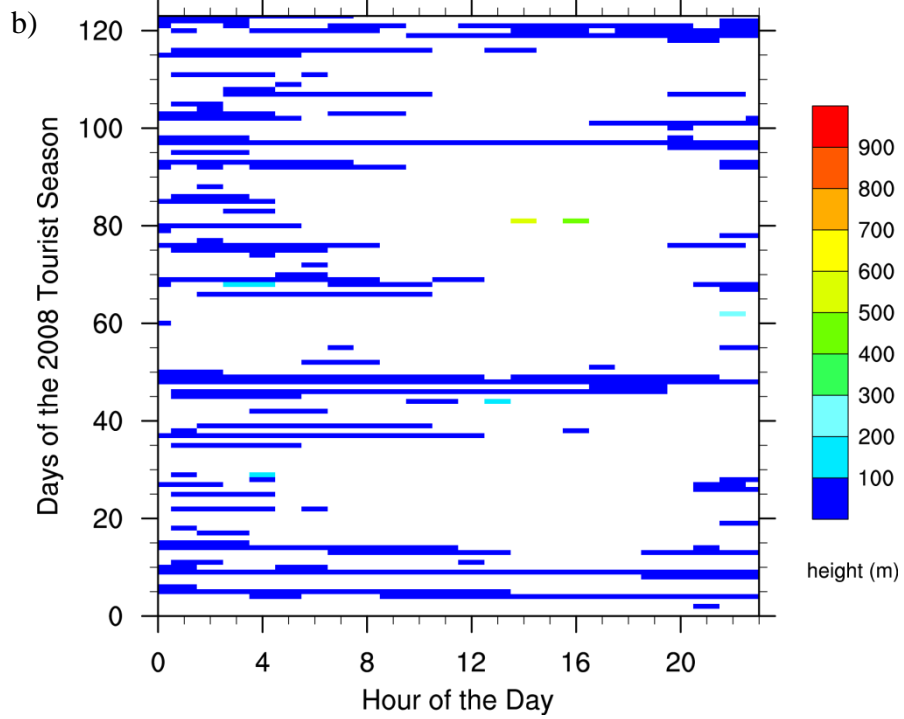
Figure 4.9 a-d Hovmöller diagrams of modeled inversion heights and frequency for the four selected grid-cells. Refer to Fig. 4.7 for the grid-cell's actual location inside Glacier Bay. For reference, May 15 is day 1, June 1 is day 18, July 1 is day 48, August 1 is day 79, September 1 is day 110, and September 15 is day 124.

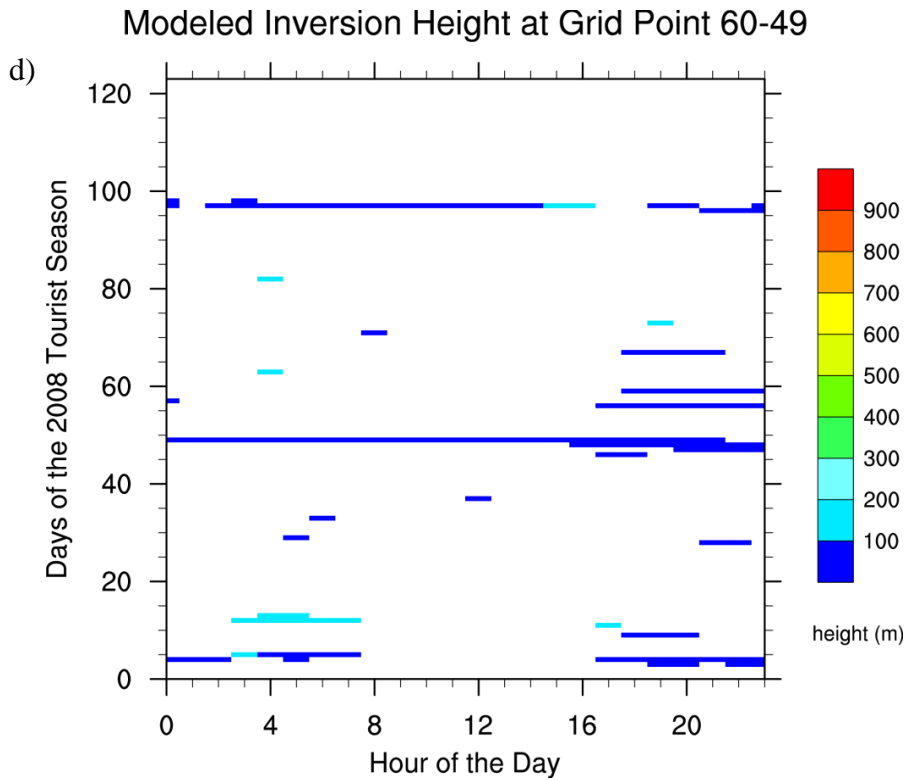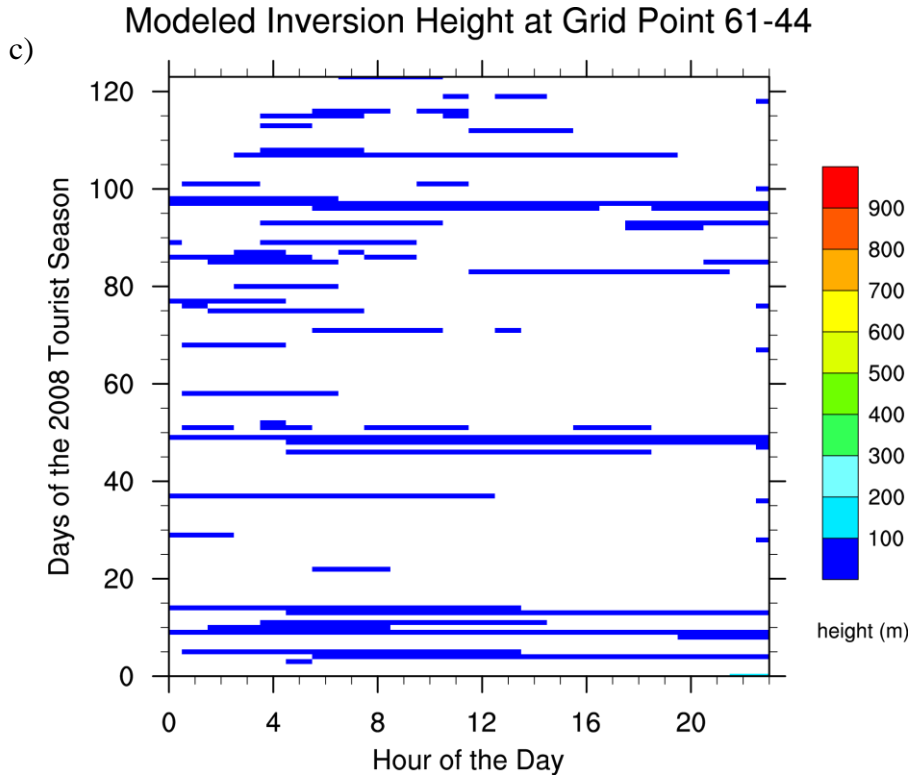strength and height was 1.33 K (100 m)$^{-1}$ and 67.8 m, respectably. With the exception of July 3 when there was only one ship in the bay, the maximum allowable number of ships (2) was inside the park each day. The strongest inversion occurred again at grid-cell 54-50 with a strength of 6.3 K (100 m)$^{-1}$ on July 2 2300 UTC (July 1 1400 AST). The inversion remained stronger than 5 K (100 m)$^{-1}$ from 2000 UTC July 2 to 0300 UTC July 3 (1100-1800 AST July 2). Strengths reached approximately 4 K (100 m)$^{-1}$ as far inside the bay as grid-point 60-44.

The final case study focuses from August 19-20. This time frame is an interesting event since day-long or longer inversions occurred at all grid-cells throughout Glacier Bay, even with a strong 974 hPa low in close proximity (Fig 4.3). The storm system narrowly missed Glacier Bay, and mostly impacted far Southeast Alaska and Vancouver Island, Canada. Inversions developed in most places late in the day on August 19, as the center of low pressure was directly to the south. Station plots indicated clear skies in the park's vicinity by 0600 UTC August 20 (2100 AST), with calm or 5 knot wind speeds. This case is a good example of strong contrasts between observed weather in areas that are in close proximity to each other. As the low moved further to the south and east, winds increased to 10 knots from the north-northwest, which is to be expected with the cyclonic flow of winds around a closed low. The shift in wind direction and speed was enough to break the inversion, and its later reformation was hindered by a subsequent storm.

During this event, the average inversion strength and height was 1.46 K (100 m)$^{-1}$ and 78.3 m, respectively. The strongest inversion occurred deep inside the Glacier Bay at grid-point 61-44 at 4.4 K (100 m)$^{-1}$ on August 20 0900 UTC (0000 AST). The particularly strong inversion remained stronger than 3.5 K (100 m)$^{-1}$ from August 20 0700-1700 UTC (2200-0800 AST). Inversions of this magnitude were also present near the entrance of the park at 54-50. Two ships were present in Glacier Bay during August 20-21, with up to two additional ships passing by the park's southern boundaries through Icy Strait.

4.2.3 Conclusions and Uncertainty

Inversions simulated by WRF/Chem appear to be consistent with the expectations related to synoptic situations in Southeast Alaska. Periods of calm weather, especially with the presence of high pressure systems and low wind speeds, are the most favorable conditions for inversions to develop, and WRF/Chem is able to capture this. However, it is difficult to evaluate the accuracy, as there are no direct observations inside Glacier Bay to confirm inversion frequency

and strength. Discrepancies regarding differing results at each grid-cell could be due to a grid-cell being very close to the side of the fjord, as WRF/Chem uses a terrain-following coordinate system. The mountains around Glacier Bay are very high, and grid-cells with little inversion activity may be impacted by advection or downsloping winds at a neighboring grid-cell. In addition, too strong advection caused by smoother than actual land-use types (Fig 4.10) could cause faster winds than in reality. Rougher surfaces than those seen in nature could lead to more turbulence, mixing, and less advection.

Certain land-uses have differing roughness lengths, thus differing modeled wind speeds. It was already shown that WRF/Chem consistently overestimated wind speeds at all surface meteorology stations in Southeast Alaska (Fig. 3.5). This overestimation is also consistent with other WRF/Chem studies (Zhang et al. 2009; Zhao et al. 2011; Mölders et al. 2012; Ngan et al. 2013; Wyszogrodzki et al. 2013), and it has been suggested to increase roughness over mountains to alleviate some of these errors. However, this overestimation of wind speeds may likely lead to an underestimation in the number and strength of simulated inversions.

It is also important to note that land cools on the side of the valleys much faster than in the middle of the bay, since water has a higher specific heat than land surfaces. Water is a good absorber of heat; however, water's response to heating is relatively slow compared to the land. It continues to emit even when solar heating has stopped, and largely controls the air temperature (Joel Curtis, personal communication, 2013). The water inside Glacier Bay tends to remain relatively cold as glaciers constantly add ice to the surface. The water is also extremely deep, with an average depth of 240 m, and a maximum depth of 430 m. The cold, deep water acts as a heat sink, and on a density basis, cold and saltier water tends to stay towards the bottom with lesser concentrations of saline water near the top (Joel Curtis, personal communication, 2013). Thus, Glacier Bay's marine climate contains numerous microscale processes that play a role in inversion formation. Furthermore, if WRF/Chem was coupled to an ocean model, it would not necessarily perform better, as SSTs would need to be initialized through observational data. The buoy network that measures ocean temperatures in Southeast Alaska is far too sparse.
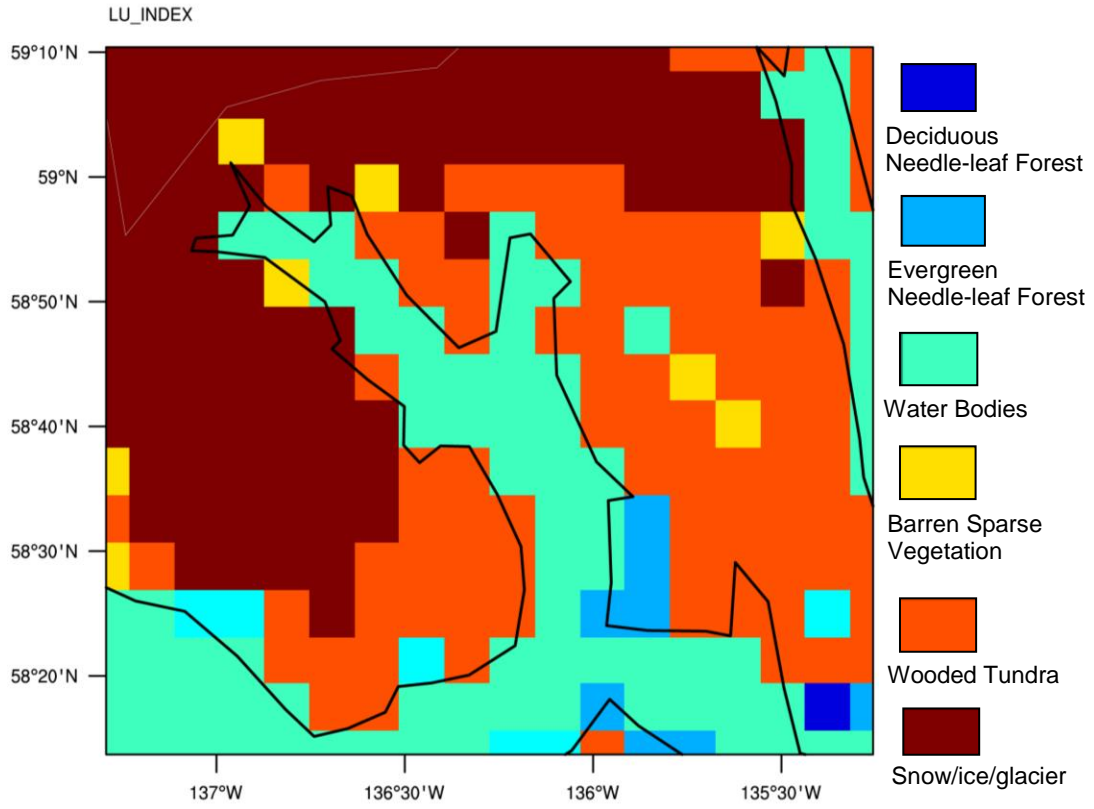
Figure 4.10 Land-use indices for the Glacier Bay area.

4.3 Types of Inversions

We can conclude from analysis of the synoptic situation and simulated inversions that many of the inversions documented in Glacier Bay are radiation inversions. They are caused by a net radiation loss as the surface cools during the short night time period. To illustrate, Fig. 4.11 shows a time series plot of daily average shortwave radiation plotted with daily average longwave radiation. The downward shortwave flux at the surface, as a result of incoming radiation from the sun, is archived every hour by WRF/Chem. This time interval is standard with most of the other meteorological data. Each day has twenty-four hourly values, thus this value results in the average daily shortwave radiation (in W m^{-2}). The same procedure was repeated for the outgoing longwave (terrestrial) radiation flux. Values are averaged to account for changes in incoming and outgoing radiation throughout the day, such as the effects of cloudiness or sun zenith angle. The values were extracted from WRF/Chem at grid-point 54-50, located close to the entrance of Glacier Bay at Starkaday Narrows. Pulling radiation data from three other locations in Glacier Bay yielded almost the same results. Thus, this location is quite representative for the entire bay regarding incoming shortwave and outgoing longwave radiation.

A diurnal cycle is evident from hourly data, and approximately five to seven hours of the day received very little, if no solar radiation due to short increments of high-latitude nighttime. This behavior is also due to the fact that the sun's rays are hitting the surface at oblique angles. Although the sun is above the horizon for many hours of the day, it is relatively low in the sky, and the sun's radiation has to travel over a longer distance and cover a larger area, as opposed to regions closer to the equator where insolation is more direct.

The averaging of hourly data also accounted for cloudy days, or days that were partially cloudy. Thus, days with less average incoming shortwave radiation were likely cloudy or foggy, some corresponding to higher amounts of average outgoing longwave radiation. Average shortwave radiation peaks at approximately day 37 (June 20) which is the summer solstice, or the day in which the sun is above the horizon for the longest period of time. Solar radiation drops rapidly as the tourist season progresses, and becomes about half of the solstice value by the middle of September. Outgoing longwave radiation remains relatively steady, only changing with apparent synoptically driven events.
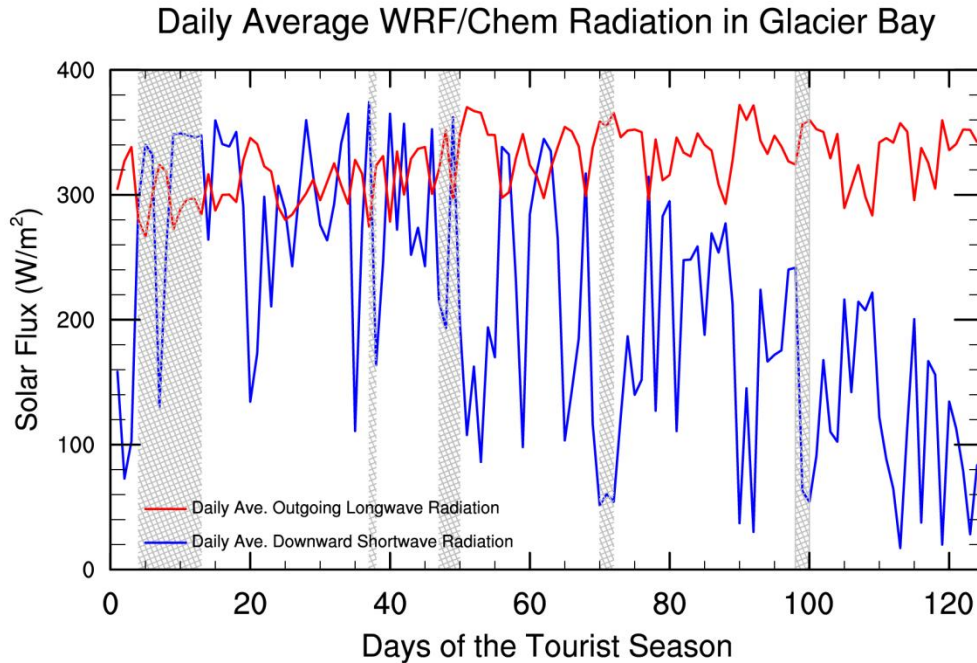
95

Figure 4.11 Time series plot of WRF/Chem simulated average daily radiation in Glacier Bay. Hourly radiation values at the surface were averaged into 24 hour daily values. The data was extracted from a grid-point near the entrance of the bay. Radiation plots at other parts of the bay were relatively similar, as the area of focus is not spatially large compared to the entire domain. The solid blue line indicates daily average incoming shortwave radiation, while the solid red line indicates daily average outgoing longwave radiation. Hatched bars indicate periods of extensive inversion events in Glacier Bay.

Most of the inversions modeled in Glacier Bay can be explained by the loss of radiation. The beginning of the tourist season is the most active time for inversion formation because the period is synoptically quiet, with the exception of a handful of storms. Towards the end of the season in August and September, the frequency and intensity of storms increase. Although the average longwave radiation leaving the surface is higher later in the season, which results in a radiative loss, a more active cyclone pattern effectively causes increased wind speed and more turbulent conditions. The increased windiness circulates air inside Glacier Bay and helps mix the air, making an inversion less likely to develop. In the absence of wind, radiation inversions are typically very common because insolation is low and outgoing radiation is high. Thus, the surface cools quicker than the air above it by radiative cooling.

In the evening hours when skies are clear, radiative cooling causes colder air to flow down into a valley since it has a higher density than warmer air (Shulski and Wendler 2007). This drainage of cold air is particularly common in Glacier Bay where the land surfaces on the

steep fjords (some of which are minimally covered with vegetation) cools as the solar radiation decreases. To further aid in cooling, most of the high peaks are capped with snow year-round. The model considers most of the mountains surrounding Glacier Bay to have a dominant land-use type of snow/ice (Fig. 4.10), which may be the dominant land-use by certain grid-cells, although in actuality there is more exposure to bare rock or some vegetation. See Fig. 4.10 to compare the model land-use type with actual satellite imagery in Fig. 2.11. In addition, a phenomenon called katabatic winds may occur as radiative cooling causes the higher density, cooler air to flow down a slope. Katabatic winds can flow down mountains, hills, or glaciers, but may be strong enough to cause turbulence and mix out an inversion (Ahrens 1985).

4.4 Particulate Matter

The primary pollutant emitted from cruise ships that causes visibility and aesthetic issues is PM_{10}, or coarse particulate matter with a diameter 10 μm or less. These particles are not only detrimental to visibility, but also to a person's health. When inhaled, particles smaller than 2.5 μm can penetrate the deepest parts of the lungs and reach the alveoli, although larger sized particles, such as PM_{10}, are commonly filtered out in the nose and throat by mucus or cilia (EPA 2012). PM_{10} is commonly sourced from dust and through the combustion of coal and diesel combustion. The heavy bunker fuel burned by cruise-ships may remain trapped between the fjords of Glacier Bay if there is no wind to recirculate the air, and/or vertical mixing or convection. The following sections will discuss air quality standards, statistics regarding PM_{10} concentrations during inversions, and document six different PM_{10} situations, starting with the most extreme case and proceeding from beginning to end of the tourist season.

4.4.1 PM_{10} Standards

Currently, there are at least two federally employed methods for monitoring $PM_{2.5}$ and PM_{10} concentrations throughout the United States. Firstly, the US Environmental Protection Agency (EPA) has set standards in order to protect health and welfare across the country. Currently, the 24 hour daily average National Ambient Air Quality Standard (NAAQS) value of PM_{10} may not exceed 150 μg m^{-3} (EPA 2012). The 24 hour average $PM_{2.5}$ exceedance standards are much lower, at 35 μg m^{-3}. It is important to note that none of the PM_{10} concentrations found in this WRF/Chem analysis exceed the 24 hour NAAQS. Occasionally, some hourly

concentrations rise to approximately half of that value, but daily averages are well below 150 µg m^{-3}. Nonetheless, the pollutants still detract from the pristine environment as water vapor attaches to them and they swell.

Another method of monitoring PM$_{10}$ is through the federal government's Interagency Monitoring of Protected Visual Environments (IMPROVE) network. In 1988, a group of Federal Land Managers and the EPA began a program to analyze the spatial and temporal trends of aerosol species through a network of aerosol monitoring sites across the Western US (Malm et al. 1994). The current IMPROVE network consists of 212 sites, of which 170 were operating in 2011 (Hand et al. 2011). The Regional Haze Rule requires air quality monitoring sites to be located in the 156 protected Class I areas, where maintaining visibility is of utmost importance. These sites are commonly located in remote areas in order to track the progression of returning federally protected areas back to pristine conditions (Hand et al. 2011).

Glacier Bay National Park is not a federally mandated Class I region. There are four Class I regions in Alaska: the Bering Sea Wilderness Area, Denali National Park, Simeonof Wilderness Area, and Tuxedni Wilderness Area. There is one IMPROVE site located in Petersburg, AK, although it is at least 275 km away from Glacier Bay. Thus, the data monitored there are not representative for Glacier Bay. Porter (2009) analyzed IMPROVE aerosol data from the Simeonof and Tuxedni IMPROVE sites for a 98 day period during the summer of 2006. She compared WRF/Chem simulated PM$_{2.5}$ and PM$_{10}$ values with the IMPROVE sites, and determined that the model significantly underestimated the actual amounts of particulate matter. At both sites, WRF/Chem simulated an average PM$_{10}$ value of 0.88 µg m^{-3}, compared to the IMPROVE PM$_{10}$ average of 6.72 µg m^{-3} (Porter 2009). These sites are located in very remote areas away from shipping lanes and other anthropogenic sources of pollution, thus WRF/Chem was likely capturing background concentrations of PM$_{10}$ while the IMPROVE sites also captured aerosols from sea-salts that she had not considered in her simulations. However, sea-salt aerosols are natural, thus a value on this order can be considered for Glacier Bay.

Low PM$_{10}$ concentrations at the Denali IMPROVE site have also been documented by Mölders et al. (2011) during a four month period in the winter of 2005-2006. The average PM$_{10}$ value was 1.1 µg m^{-3} with no values exceeding 3.8 µg m^{-3}. Thus, a pristine, wildfire-free day in Denali may have extremely low PM$_{10}$ values. During Asian dust events, the PM$_{10}$ value may increase on the order of 1-2 µg m^{-3}, but is generally still extremely low.

On both June 20 and June 24, no cruise ships were present in Glacier Bay. The average near-water PM_{10} concentrations were quite pristine at approximately 2 μg m^{-3}. The vertically integrated PM_{10} concentrations were approximately 2100 μg m^{-2}. Using the average observed concentration of 6.72 μg m^{-3} at the Class I Simeonof and Tuxedni sites, assuming an ABL height of 1 km, and considering background concentrations of 0.1 μg m^{-3} above 1 km would lead to a vertically integrated value of 5985 μg m^{-2} for pristine air. This is what a satellite would see if it took measurements with a radiometer sensitive to PM_{10}.

In order to propose future policy and air quality management goals, the National Park Service seeks to understand when conditions are no longer considered "pristine" inside of Glacier Bay. Typical background concentrations in WRF/Chem are generally pristine below 1-2 μg m^{-3}. Thus in Glacier Bay, any elevated rise in PM_{10} is likely due to ship traffic. The environmentally pristine air quality above most inversion levels (around 1 km) to the air quality close to the surface is compared later in this chapter to assess the deviation from "pristine" in Glacier Bay. In addition, a comparison between a simulation with and without cruise ships inside Glacier Bay is presented.

4.4.2 Particulate Matter Statistics

Similar to the Hovmöller diagrams used for the analysis of inversions in section 4.2.2, concentrations of PM_{10} between the ground and the top of the model are analyzed as a bay average in Fig. 4.12, and at the same grid-points in Fig. 4.13a-d. The charts show the vertically integrated PM_{10} concentration for each hour of the tourist season at individual grid-cells. In WRF/Chem, there are PM_{10} concentrations for each model level. The thickness of each level was multiplied by its corresponding concentration and summed. Thus, the integrated value from surface to the top of the model (in μg m^{-2}) eliminates one dimension. These units yield an absorption cross-section through the model's vertical profile. Most of the particulates are concentrated towards the ground level, as cruise-ships act as the only point source of pollution. Subsequent aerial-view plots with PM_{10} concentrations in the remainder of this chapter depict the actual pollution occurring in the ABL, as upper level concentrations are typically background concentrations.

The four grid-points selected for inversion analysis are also helpful for understanding how deep pollutants get injected into the fjords of Glacier Bay. High pollution events, with

vertically integrated concentrations ≥ 9000 μg m^{-2}, occur in all locations at similar time frames, indicating the presence of a cruise ship and dispersal through the bay. The grid-cell 54-50 appears to experience the most amount of pollution, as cruise-ships will pass directly through this area, and possibly again as they leave the park. In addition, PM$_{10}$ from ships passing by Glacier Bay through Icy Strait may waft through Starkaday Narrows and inject pollutants, even though a cruise ship does not enter the park. It is especially evident at the start of the tourist season, where concentrations are typically ≥ 5000 μg m^{-2} for the first fifteen days, even though no ships entered on day 1 and day 3.
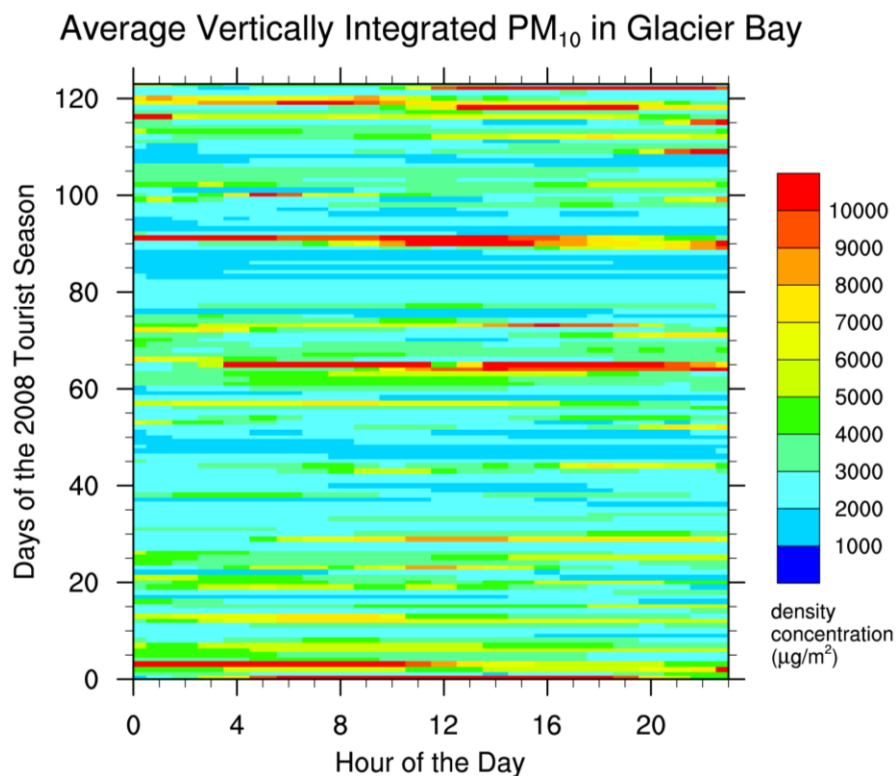
Figure 4.12 Average Hovmöller diagram of WRF/Chem vertically integrated PM$_{10}$ absorption cross-sections (μg m^{-2}) throughout all grid-cells in Glacier Bay. Each WRF/Chem level has a PM$_{10}$ concentration. The plotted values are the integrated amounts calculated by summing the product of thickness and concentration in μg m^{-3} at each of the 27 levels. This eliminates one dimension in the data.

The red stripes shown on Figs. 4.12 and 4.13a-d occur when two ships, the maximum daily allowance, enter Glacier Bay. Most of these days also have up to three additional ships sailing by Glacier Bay, but not actually entering. PM$_{10}$ levels in Glacier Bay not only depend on the synoptic situation, but also the type of ship. Cruise ships of varying sizes enter Glacier Bay,

and the amount of pollution depends on passenger load, type of fuel, and/or presence or use of exhaust scrubbers. For confidentiality reasons, the data containing cruise-ship type, fuel used, engine power, etc. was stripped, and we focused on whether a ship was there or not, rather than which ship was there.

During the twelve days of the tourist season when no cruise-ships entered Glacier Bay, SO_2, NO_x, PAN, $PM_{2.5}$, and PM_{10} concentrations were 23%, 15%, 3%, 15%, and 18% lower than on other days with ships present (Mölders et al. 2013). The lower percent difference in $PM_{2.5}$ than PM_{10} is due to the stronger sedimentation and removal of the larger PM_{10} particles.

Over the entire season and throughout all grid-cells in Glacier Bay, the average near surface PM_{10} concentration without inversions was approximately 3.1 µg m^{-3}, and with simulated inversions was 3.3 µg m^{-3}. This resulted in about a 6% increase of PM_{10} concentration when there is an inversion present. It is important to remember that high concentrations of pollution do not always mean there was an inversion present in Glacier Bay. Inversions could have also occurred when there were no ships in the bay. In addition, a ship may emit high amounts of PM_{10} as it passes through a particular grid-cell, but not an adjacent one (since it may not go through that grid cell). The grid-cell 54-50 experienced the highest increase in PM_{10} concentration when there were inversions, as ships likely pass through this section of the bay twice. Its average inversion free concentration was 4.2 µg m^{-3} compared to 5.2 µg m^{-3} when inversions were present, leading to an increase of about 20% with inversions. In addition, WRF/Chem favors keeping some of the higher concentrations of pollution from reaching the furthest grid-cells inside Glacier Bay (see section 4.4.6 for an example). When inversions are present, there is hardly any circulation in the bay, and pollutants stay close to where they were emitted. Thus, upper, less traveled fjords remain relatively unaffected even though inversions exist.

PM_{10} concentrations were also calculated based on inversion strength. The three classes of inversions, as documented in section 4.2.1, result in increasing concentrations of PM_{10} with inversion strength. Strong inversions produced an average elevated PM_{10} concentration of 5.4 µg m^{-3} over all grid cells in Glacier Bay for the entire tourist season. This is roughly a 43% increase in PM_{10} levels during strong inversions compared to no inversions. Moderate inversions resulted in an elevated PM concentration of 3.3 µg m^{-3}, or approximately 6% increase over inversion free days. Weak inversions did not lead to notable rises in PM_{10} levels, which may be attributed to the fact that they are too weak to influence the trapping of pollution. Grid cell 54-50 experienced the

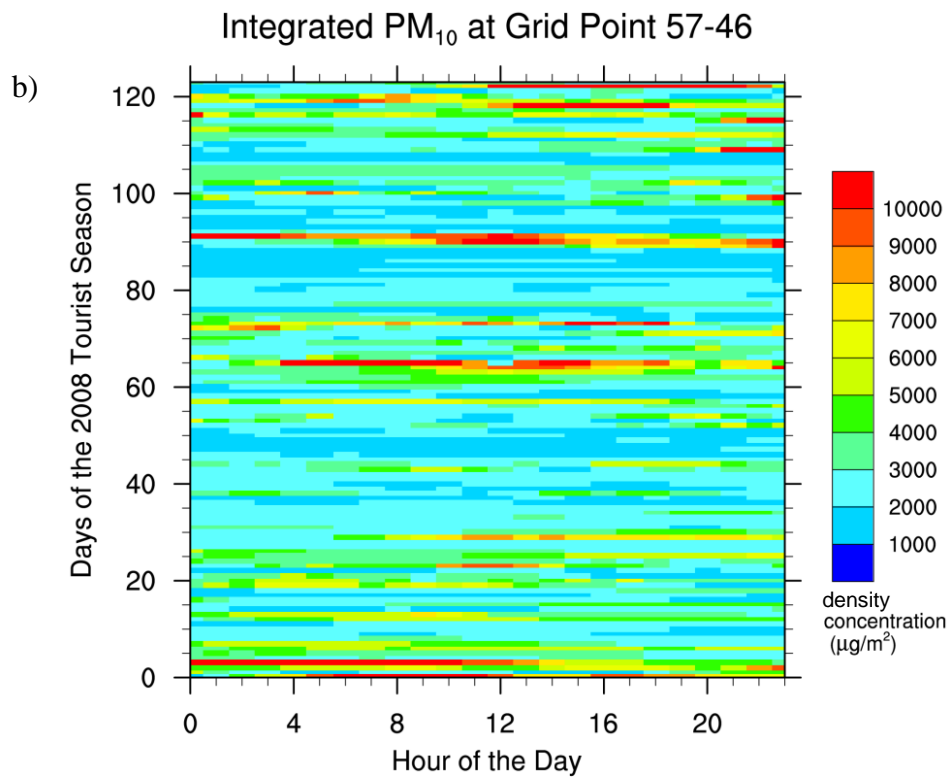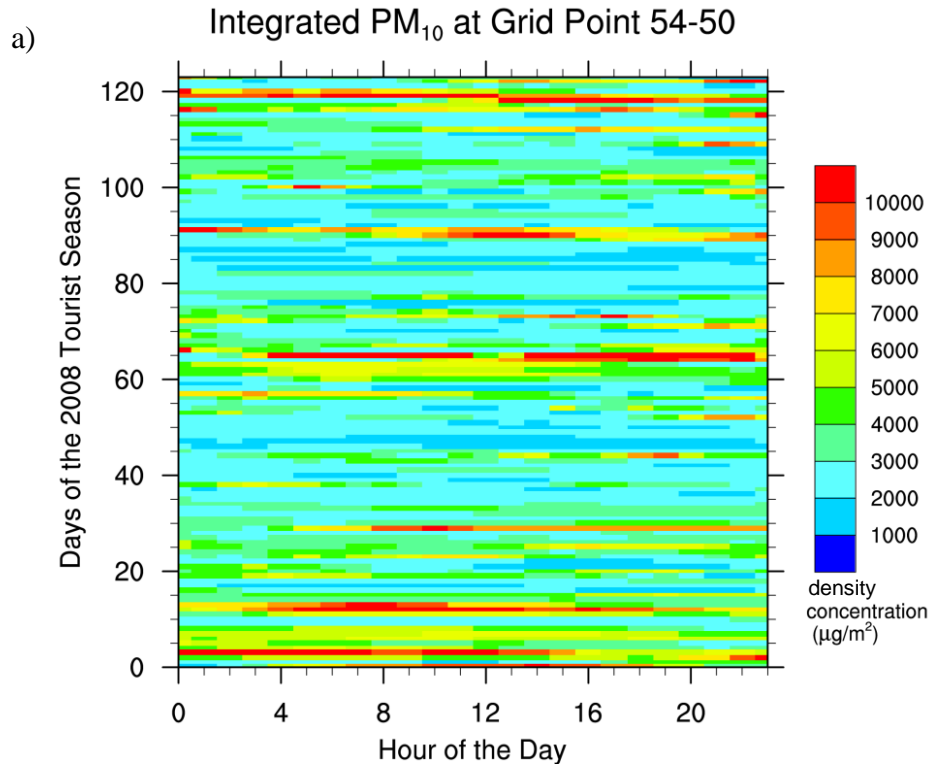a) Integrated PM$_{10}$ at Grid Point 54-50

b) Integrated PM$_{10}$ at Grid Point 57-46
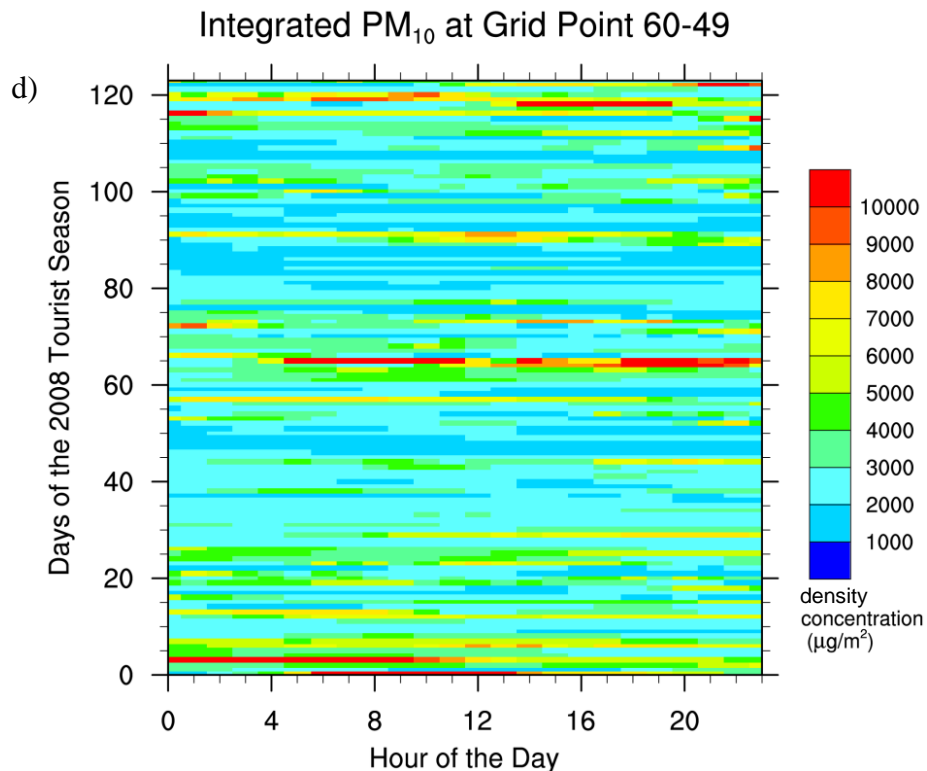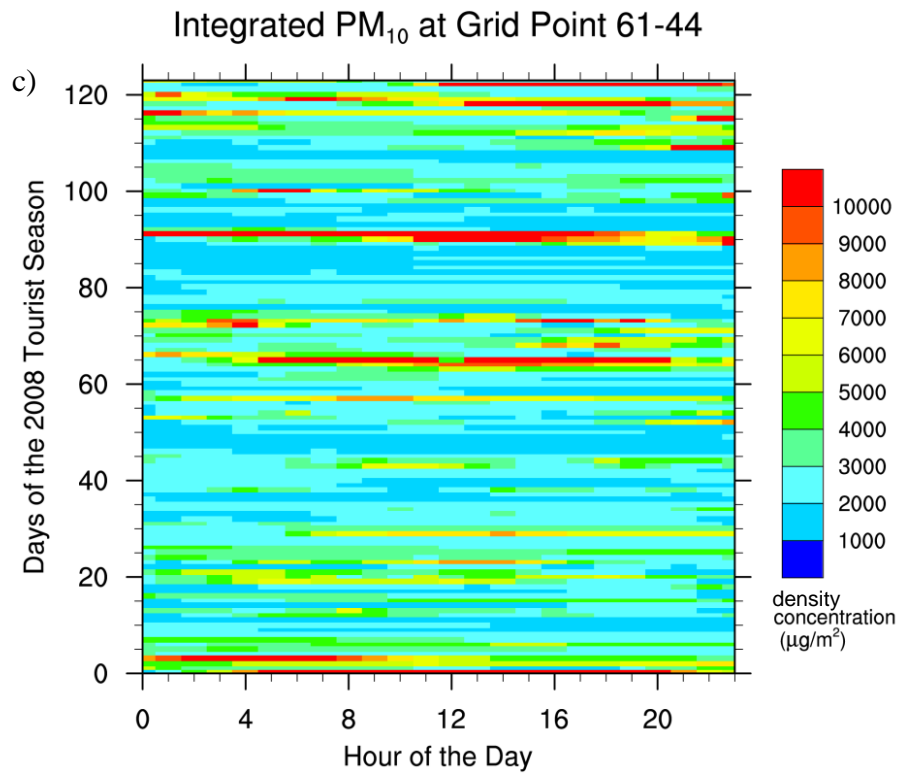
Figure 4.13 a-d Hovmöller diagrams of WRF/Chem vertically integrated PM$_{10}$ absorption cross-sections (μg m^{-2}) at select grid-cells. Each WRF/Chem level has a PM$_{10}$ concentration. The plotted values are the integrated amounts calculated by summing the product of thickness and concentration in μg m^{-3} at each of the 27 levels. This eliminates one dimension in the data.

strongest inversion event and also had the highest average concentration of PM_{10}, with 4.7, 4.7, and 6.5 µg m^{-3} during weak, moderate, and strong inversions, respectively. Furthermore, it is clear that strong inversions of more than 2 K (100 m)$^{-1}$ will trap ship emissions if a ship is present.

4.4.3 July 19 Highest Pollution Event

The most extreme PM_{10} event occurred on July 19 for most of Glacier Bay. Two ships entered the park on this day. Fig. 4.14 shows the 24-hour temporal evolution of PM_{10} and wind throughout the day. A very weak stationary front was located off the coast of southeast Alaska on July 19 0000 UTC (1500 AST July 18). As shown on the series of plots, winds began relatively light (generally less than 10 knots or 5.1 m/s), and slowly increased to about 20 knots (10.3 m/s) from the southeast during the day. The air was fairly clean (< 6 µg m^{-3}), but pollutants were evident by 0500 UTC (2000 AST). High concentrations of PM_{10} in excess of 44 µg m^{-3} were present in the Cross Sound, and over the eastern Gulf of Alaska.

As the stationary front shifted further east throughout the day, wind direction also shifted towards the south and southwest. Advection of pollutants from the shipping lanes elevated PM_{10} concentrations in Glacier Bay to 44 µg m^{-3}. Then, later in the day around 1500 UTC (0600 AST), the entrance of both cruise ships likely kept the PM_{10} concentrations stable at about 18 µg m^{-3} for the remaining nine hours of July 19. Fig 4.15 shows the average PM_{10} concentration throughout the day. The heterogeneity of pollution in the park appears to depend on where the ships travel or do not travel. Especially high concentrations are evident towards the middle of the bay, as well as in the northwest fork, as both ships have to pass though the middle twice and berth in the northwest fork for glacier viewing.

The high concentrations of PM_{10} may also be due to advection from cruise ship and ferry travel on highly traveled shipping lanes, such as those directly off the coast in the Gulf of Alaska, or through Alaska Panhandle's Inside Passage. The Inside Passage is a coastal network of routes for a wide variety of vessels, including cruise ships, freighters, and fishing boats. In addition, the Alaska Marine Highway System operates numerous ferries in this region, which acts as an important transportation corridor connecting harbors throughout Southeast Alaska. One to two ferries each day may pass through Icy Strait to destinations such as Yakutat and the

rest of South-Central Alaska. Other ships may enter the Inside Passage via Icy Strait, and therefore pass within close proximity to the entrance of Glacier Bay National Park.

The daily average PM_{10} concentrations shown in Fig. 4.15 depict high daily concentrations (up to 22 μg m^{-3}) inside Glacier Bay. The slight offset of high PM_{10}, as indicated with the red circles, are examples of the wind pushing pollutants toward the mountains. The daily average cross section in Fig. 4.16 confirms that the highest PM_{10} levels were closest to the surface, although the cruise-ship plumes diffused as high as 1500 m. The cross section is taken from the area noted by the red line in Fig. 4.7.

Most inversions levels in this thesis existed very close to the surface. In order to understand how strongly inversions trap pollutants, a comparison was made between the relative environmentally pristine air (which is typically on the order of about < 1-2 μg m^{-3}) above most inversion levels (around 1 km) to the value close to the surface where the cruise ships travel. On July 19, the daily average PM_{10} concentration close to the surface was 20.5 μg m^{-3}. The concentration above any inversion levels was 6.6 μg m^{-3}. Approximately 400 m above that level, PM_{10} concentrations diminished to 3.1 μg m^{-3}. Thus, areas with weak or no inversions likely allowed the cruise-ship plumes to diffuse higher.

A simulation without cruise-ship emissions (Fig. 4.17) was compared to the one with cruise-ship emissions in Fig. 4.15. This presents the impact that cruise ships have on the air quality in Glacier Bay. Average background concentrations of PM_{10} were extremely low, with nothing exceeding 0.22 μg m^{-3}. Therefore, any elevated levels of PM_{10} are likely due to cruise ship traffic. Background levels of PM_{10} may be due to airborne dust particles or sea salts kicked up by the wind. A subsequent plot showing the difference between cruise-ship emissions and no cruise-ship emissions would not look much different than Fig. 4.15 since the background concentrations are so low. These background concentrations are on par with Porter (2009) and Mölders et al.'s (2009) findings using WRF/Chem in very remote areas of Alaska.

Figure 4.14 Zoom-in plots showing the temporal evolution of PM_{10} on July 19, 2008. The panel plot depicts the "worst case event" of PM_{10} during the 2008 tourist season. There were two cruise ship entrances, the maximum daily allowance. Synoptically, weather was calm with short-lived inversions in some parts of Glacier Bay. All plots have the same color scale.
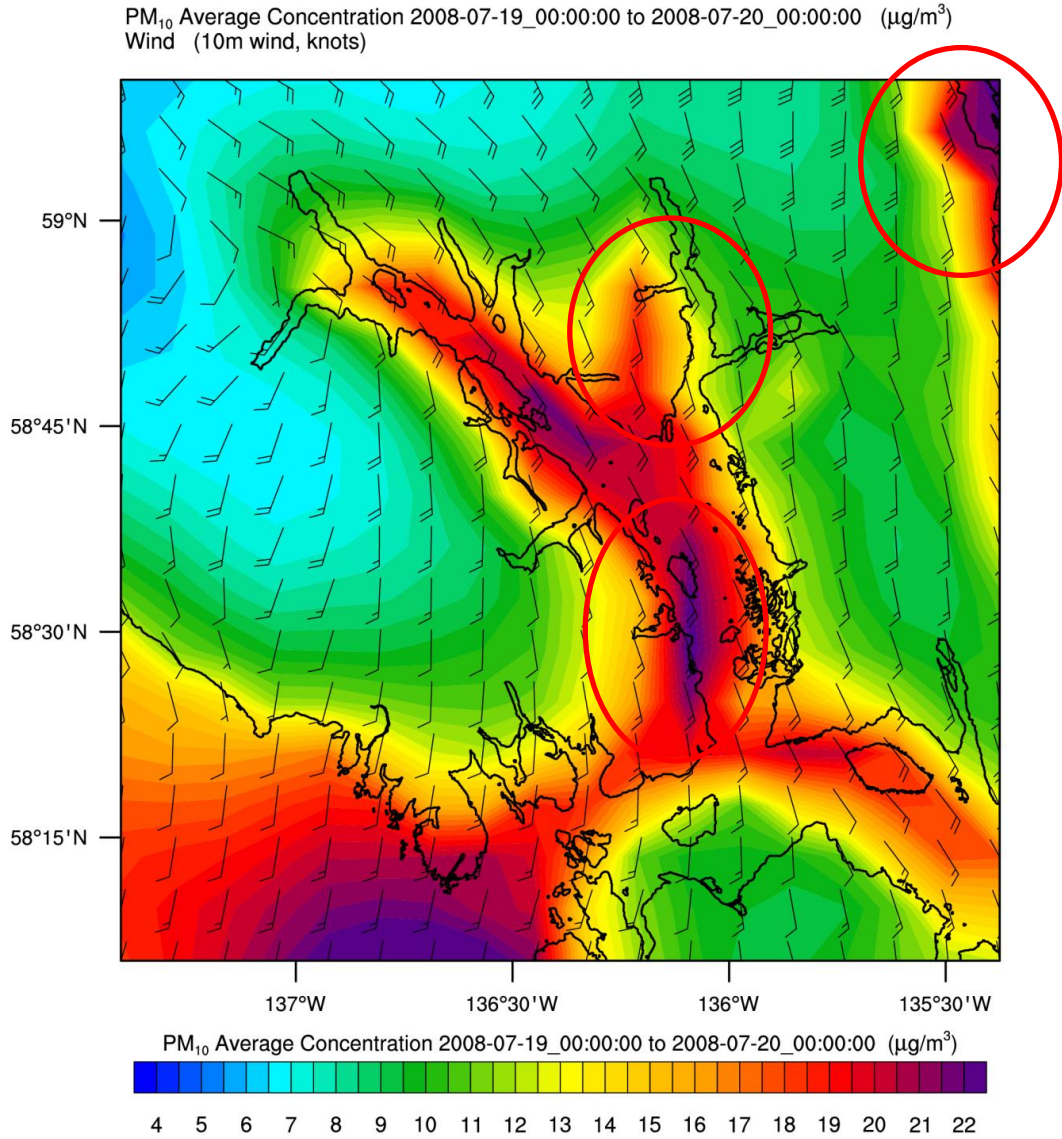
Figure 4.15 Average daily PM$_{10}$ concentrations for July 19, 2008 overlaid on a zoom-in plot of Glacier Bay. Note the change in color scale from Fig. 4.12. The red circles are examples of how the wind pushes pollutants towards the mountains.
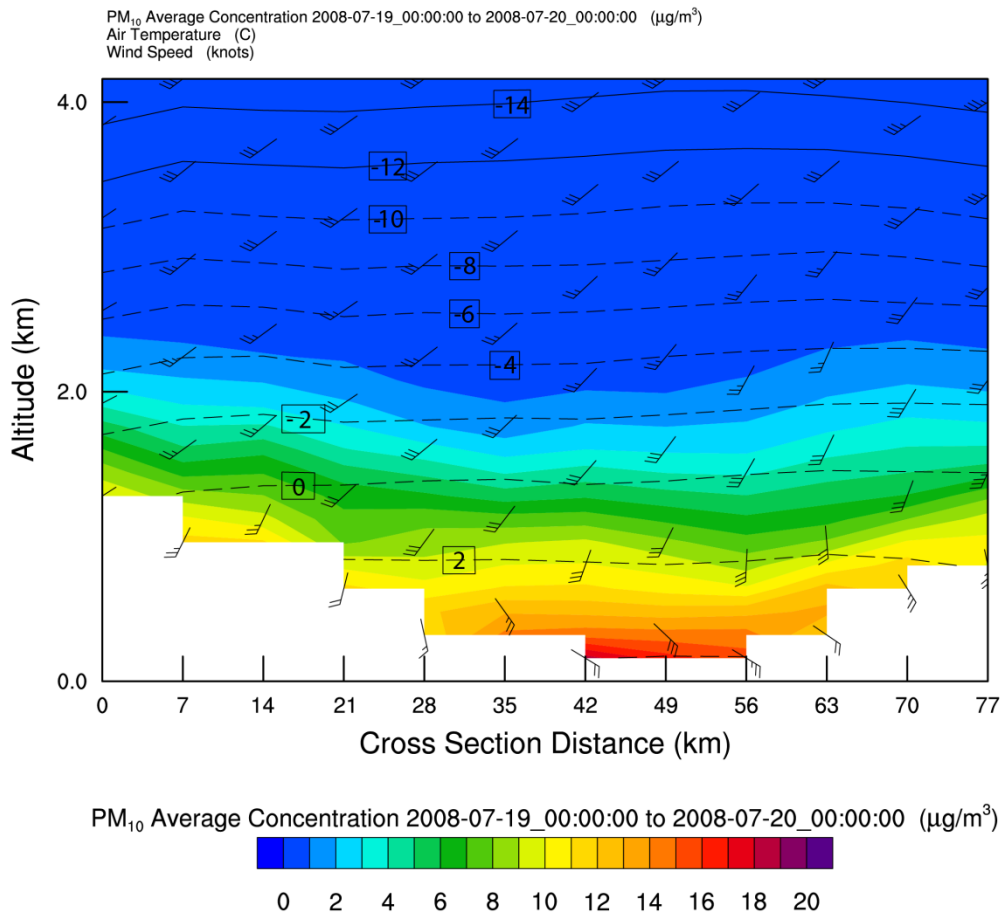
Figure 4.16 Average daily cross section across central Glacier Bay on July 19, 2008 showing air temperature (°C), horizontal wind speed (knots), and PM_{10} concentration (μg m^{-3}). White indicates model average terrain height of the grid-cells.
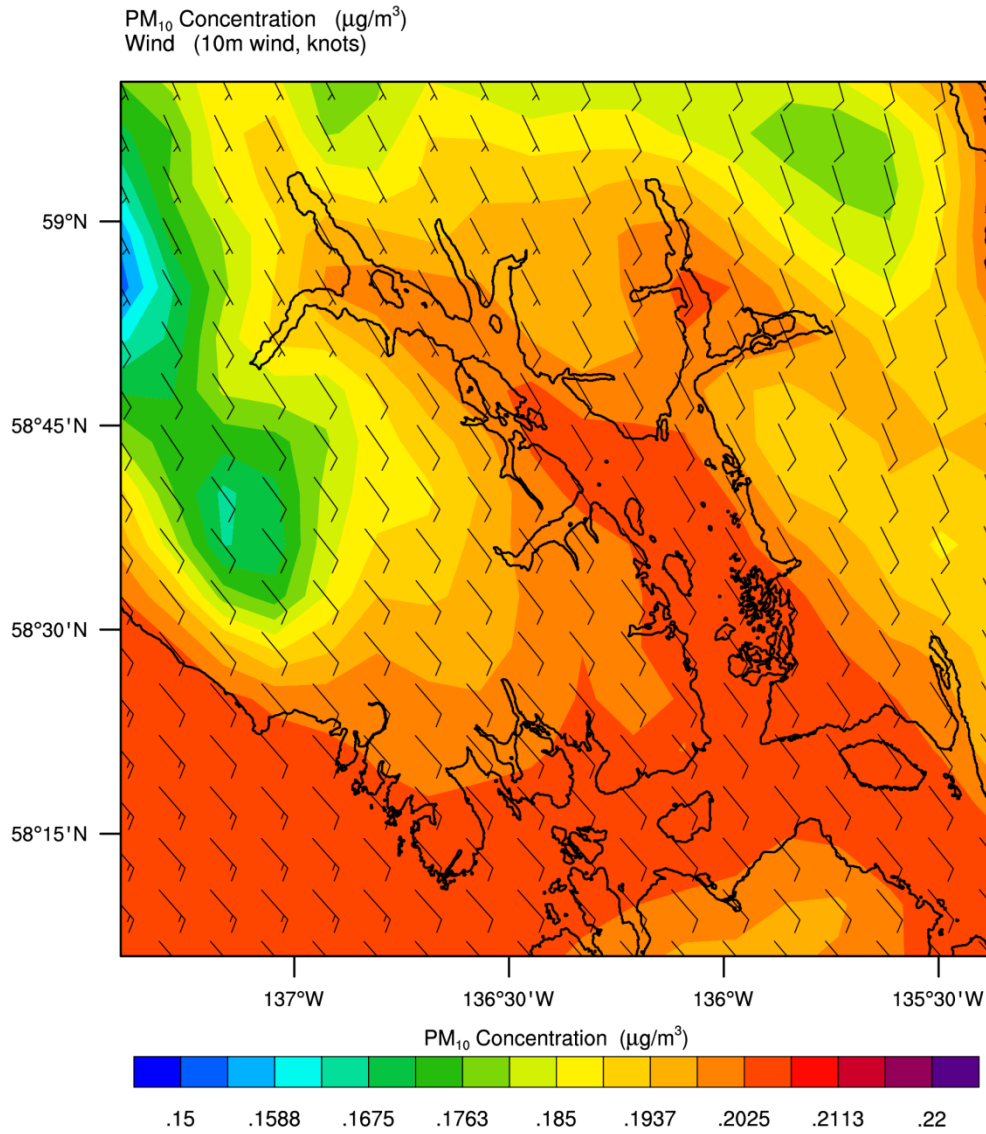
Figure 4.17 Average background PM_{10} concentrations inside of Glacier Bay for July 19, 2008. This simulation considers no cruise-ship emissions, and represents the pristine air quality if there were no cruise ships present. PM_{10} concentrations do not exceed 0.22 μg m^{-3} inside Glacier Bay, and are likely the result of airborne dusts or sea salts.

4.4.4 May 17 Event

May 17 was the third day of the tourist season, and had no cruise ships entering Glacier Bay. The first cruise ship of the tourist season entered the bay the day prior, and any PM_{10} concentration inside the park is likely left over from May 16 (since winds were mostly calm to 5 knots), or gently advected in from the highly traveled shipping lanes outside of Icy Strait. A weak inversion was present in most grid-cells towards the entrance of Glacier Bay. This local feature may be why there are higher average PM_{10} concentrations (around 8 μg m^{-3}) towards the entrance of the park (Fig. 4.18a) than deeper inside. With light winds around 5 knots, slight southeast advection of air with relatively higher PM_{10} concentrations from Icy Strait may have also contributed to the elevated concentrations in the lower bay. The Icy Strait waterway and corridor along the Southeast Alaska coastline is a highly traveled ship lane used by numerous cruise ships, as well as the Alaska Marine Highway ferry system.

The average May 17 PM_{10} concentration close to the surface was 3.8 μg m^{-3}. Above any inversion level, the concentrations reduced to 2.3 μg m^{-3}, and rapidly diminished to pristine conditions of 0.9 μg m^{-3} just 400 m higher.

a)

PM$_{10}$ Average Concentration 2008-05-17_00:00:00 to 2008-05-18_00:00:00 (μg/m^3)
Wind (10m wind, knots)

PM$_{10}$ Average Concentration 2008-05-17_00:00:00 to 2008-05-18_00:00:00 (μg/m^3)

REAL-TIME WRF   Init: 2008-05-17_00:00:00

b)

PM$_{10}$ Average Concentration 2008-05-17_00:00:00 to 2008-05-18_00:00:00 (μg/m^3)
Air Temperature (C)
Wind Speed (knots)

PM$_{10}$ Average Concentration 2008-05-17_00:00:00 to 2008-05-18_00:00:00 (μg/m^3)
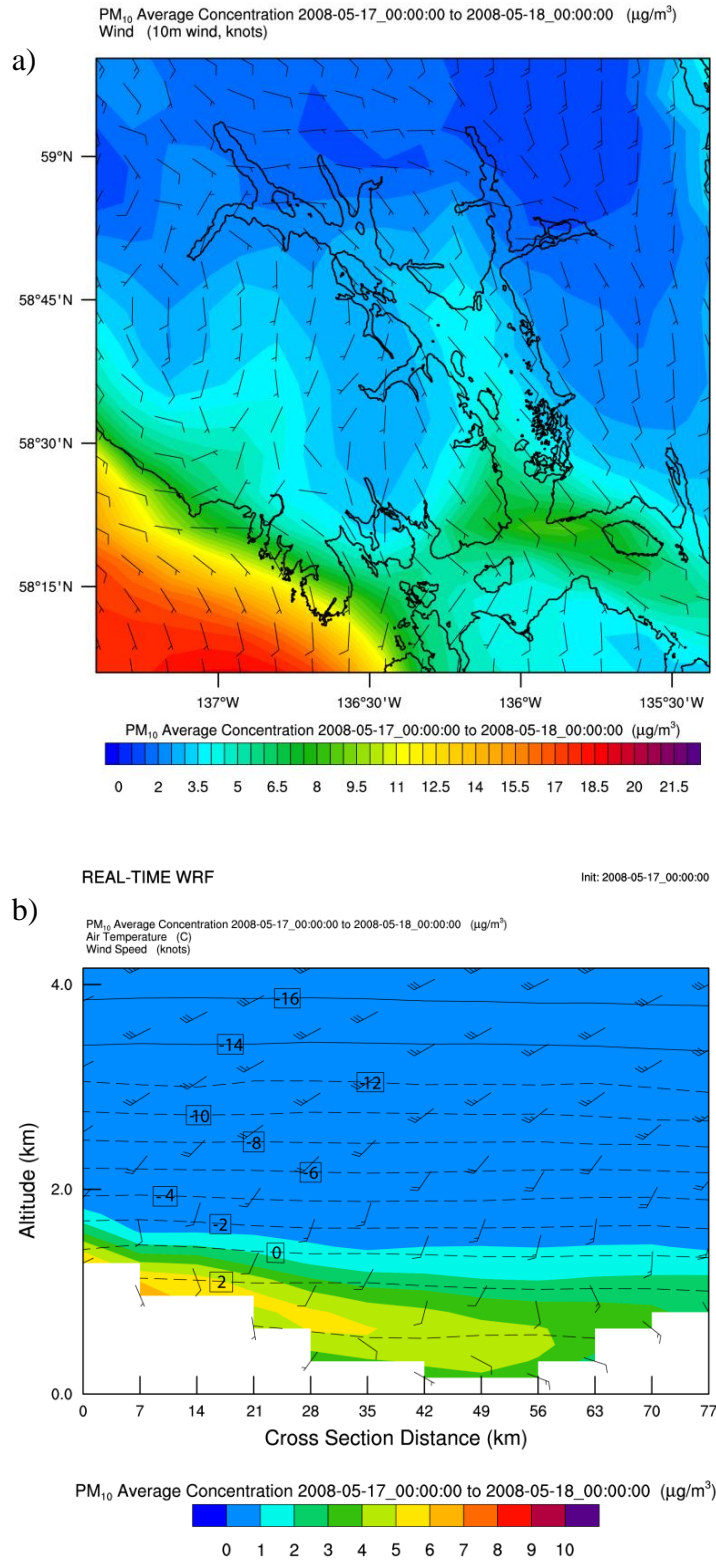
Figure 4.18 a) Average daily contour plot and b) cross section for May 17, 2008 zoomed in on Glacier Bay. There was an inversion present, but no cruise-ship entry on this day.

111

4.4.5 May 19-20 Event

The May 19-20 event is unique in that the model captured the concentrations of two separate cruise ships entering and departing Glacier Bay. Inversions were present at most grid-cells, with some inversions particularly strong at ≥ 4.5 K $(100$ m$)^{-1}$. However, once the ships emitted the pollutants, PM_{10} remained quite close to the original emission source. Elevated concentrations did not penetrate into the deep fjords like they had done for other cases. This finding is potentially due to winds inside Glacier Bay that were blowing from the opposite direction than on most other days. Winds were coming from the north-northwest, i.e. from areas without pollution. Thus, there was no pollutant advection from areas outside Glacier Bay into the park, and PM_{10} from areas of high ship traffic in the Gulf of Alaska was largely prevented from entering Icy Strait. Wind speeds were very low, at approximately 5 knots throughout most portions of the bay, and this synoptic situation kept inversions from breaking. Weather remained quiet in the area, as a storm impacted the far southern portions of the Alaska Panhandle and Northwest United States.

During this event, WRF/Chem simulated a basic mesoscale slope breeze inside of Glacier Bay, which is particularly evident on the cross section plots. Mountain and valley breezes (Fig. 4.19) are common in areas with complex terrain, and develop during calm synoptic conditions during diurnal changes in the radiation balance. During the day, the sun heats the mountain slopes and air at the bottom of a valley. Since warmer air is less dense and more buoyant, it tends to gently flow up the mountain slopes. However, the vertical ascent of the air may be hindered by the presence of an inversion layer, forcing it back to the bottom of the valley. This results in a self-contained circulation. The reverse may occur during nighttime hours, when the land surfaces cool by radiation loss. The denser, cooler air begins to flow downslope, causing a mountain breeze. The air converges at the bottom of the valley, and may be forced upward. The vertical ascent may then become obstructed by an inversion layer, resulting in a self-contained circulation. A similar process occurs during up-valley and down-valley circulations (Fig. 4.20).

During the morning at 1600 UTC (0700 AST), the air inside Glacier Bay was clean (Fig. 4.22), with a slight 1-2 µg m^{-3} concentration of PM_{10} left over from previous cruise-ship entries. However, the first cruise ship was present in the central part of the bay by 1400 AST (Fig 4.23). Pollutants became dispersed two hours later (Fig 4.24), and the next ship entered by 1900 AST (Fig 4.25). By the mid-afternoon hours, a mesoscale slope breeze developed as the sun heated the

mountain land surfaces (Fig. 4.23). At 1600 AST, upslope winds on the westward facing mountains slopes lead to the spreading of PM_{10}, but the vertical ascent was largely restricted by the inversion level, thus trapping the pollutants. A self-contained mesoscale circulation resulted, and WRF/Chem shows the gentle counterclockwise flow of the winds in Fig. 4.24.

As the day progressed, the circulation changed into a more downsloping pattern by 0200 AST (Fig. 4.26) when the radiation balance was likely negative. On the left side of the bay (as seen in the cross section in Fig. 4.26), a sagging of the isotherms indicates the presence of a cold pool building. The wind barbs show that winds were gently flowing down the mountain slopes. Concentrations from cruise-ship emissions during this day peaked around 12-14 μg m^{-3}. The cross section in Fig 4.26 shows how the PM_{10} largely diminished by 0200 AST, but the inversion kept the pollutants from diffusing very quickly, as the inversion held through May 20.

The average PM_{10} concentration close to the surface during this event was approximately 4.8 μg m^{-3}. Above any of the inversion levels around 1 km, concentrations rapidly diminished to pristine conditions of 0.9 μg m^{-3}. Thus, it is clear that during this strong inversion event, inversions trapped the ship emissions from the environmentally pristine conditions above. The mesoscale slope breeze circulation remained contained below the inversion level.
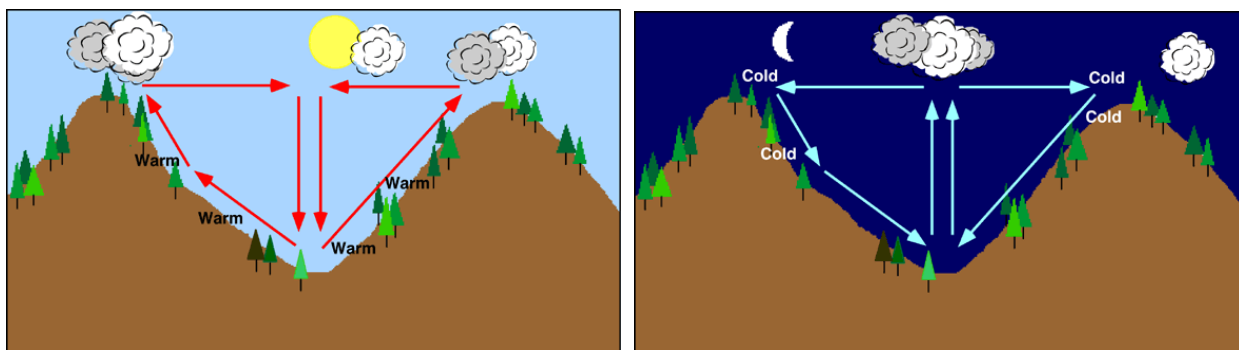
Figure 4.19 Schematics of the mesoscale slope breezes. (Left) daytime development of an upslope valley breeze, and (right) nighttime development of a downslope mountain breeze. Retrieved 03-20-2014 from: http://www.physicalgeography.net/fundamentals/7o.html.

Diurnal Cycle of Up-valley and Down-valley Circulations

Upslope and up-valley midday

Downslope and down-valley midnight

©The COMET Program

Figure 4.20 Diurnal cycle of up-valley and down-valley mesoscale circulations. Diurnal variations in daytime solar heating and nighttime radiation loss lead to a shift in wind directions, similar to those in Fig. 4.19. Retrieved on 03-20-2014 from the MetEd COMET Module: http://www.meted.ucar.edu/tropical/synoptic/trop_meso_circ/print.htm.
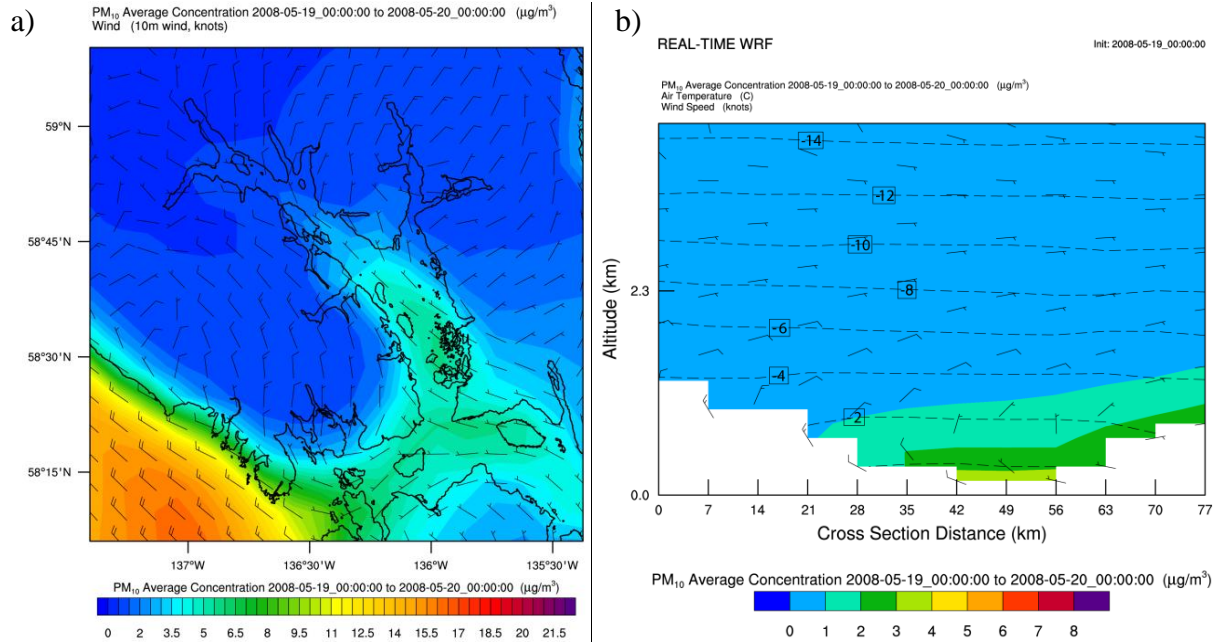
Figure 4.21 a) Daily average contour and b) cross section for May 19, 2008. This event occurs at the beginning of the tourist season. The figure reflects two separate cruise-ship entrances. Weather was relatively quiet with inversions present in most parts of Glacier Bay.

Figure 4.22 a) 1600 UTC (0700 AST) May 19 zoomed-in contour and b) cross section. These plots show the PM_{10} concentration before the cruise-ship entry. There is a slight plume left over from previous ship entries, but very low in concentration (2 μg m^{-3}).

115
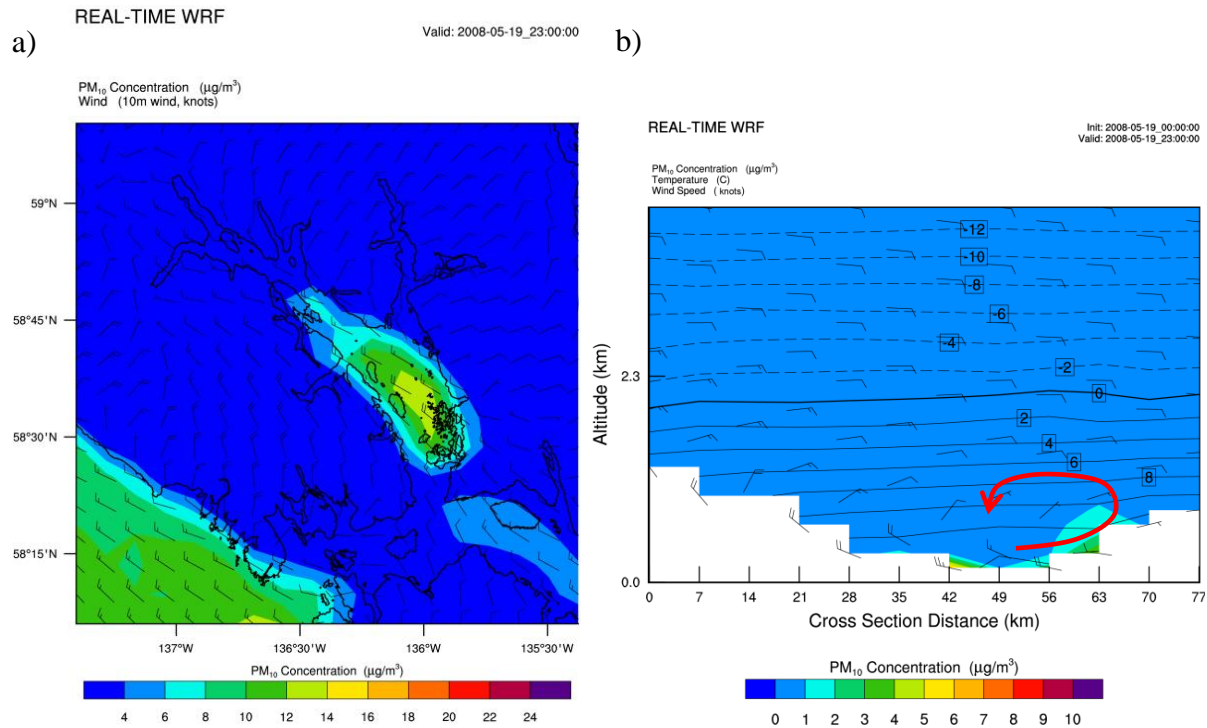
Figure 4.23 a) 2300 UTC (1400 AST) May 19 zoomed-in contour and b) cross section. These plots show PM_{10} concentrations during the first cruise-ship entry. A mesoscale upslope breeze begins to develop with daytime heating, leading to a gentle counterclockwise turning of the winds.

Figure 4.24 a) 0100 UTC May 20 (1600 AST May 19) zoomed-in contour and b) cross section. These plots show the PM_{10} concentration before the second cruise-ship entered Glacier Bay. Vertical ascent of the polluted air within the mesoscale circulation is limited by the presence of inversion layer, effectively trapping the PM_{10}.

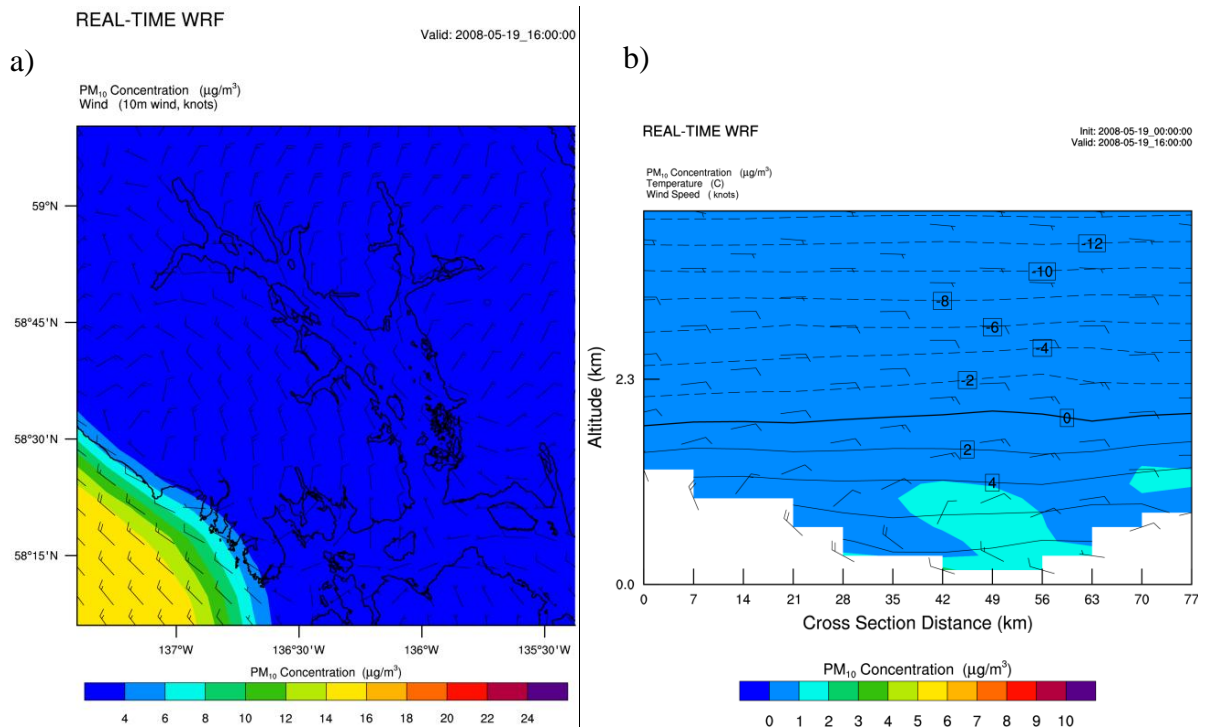Figure 4.25 a) 0400 UTC May 20 (1900 AST May 19) zoomed-in contour and b) cross section. These plots show the PM_{10} concentration during the second cruise-ship entry, with continued mesoscale circulation and pollutants being trapped close to the surface by inversion.
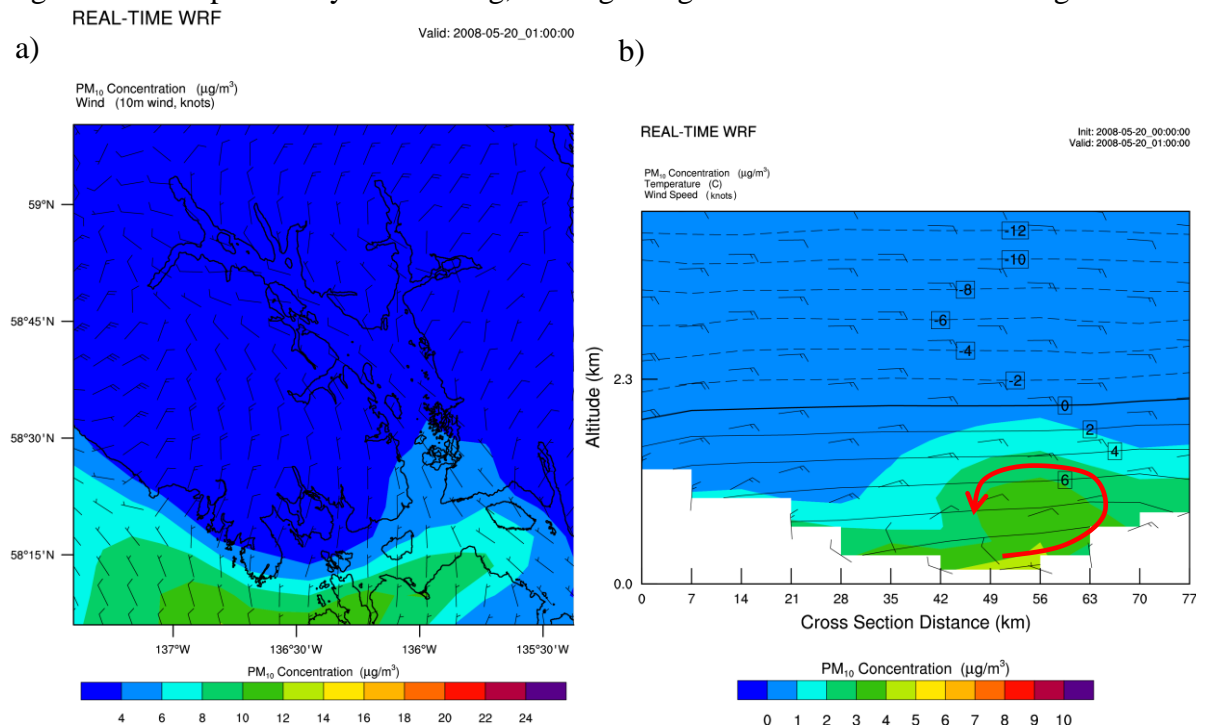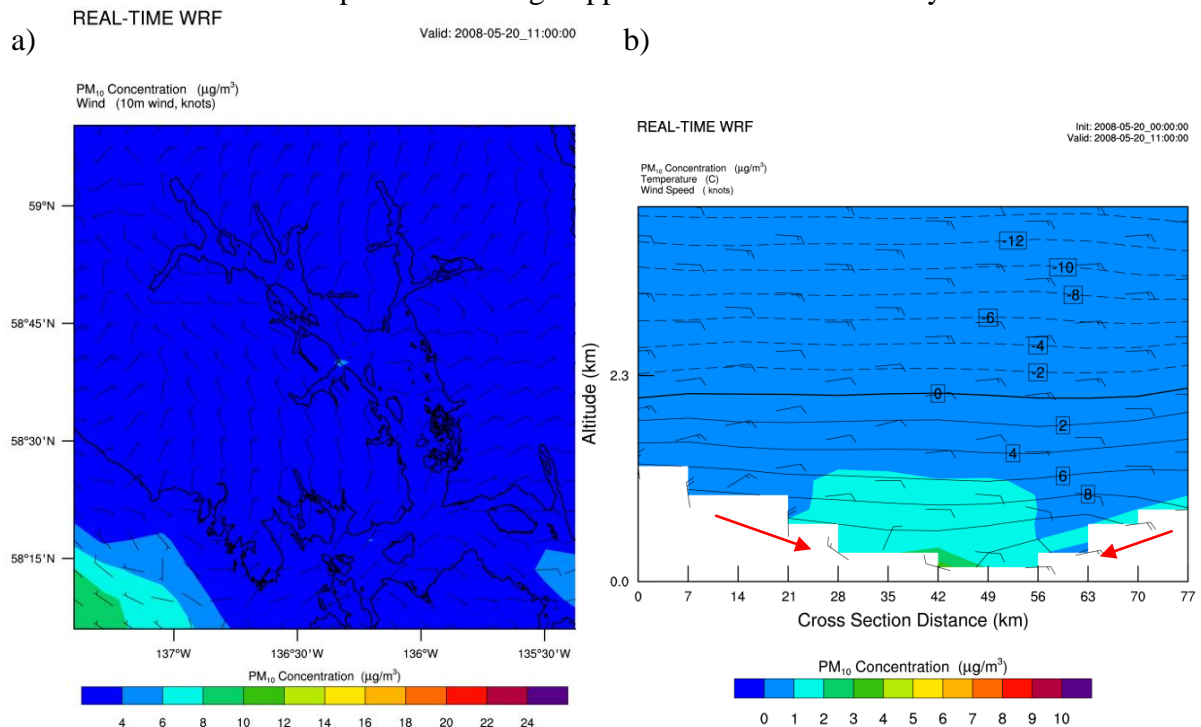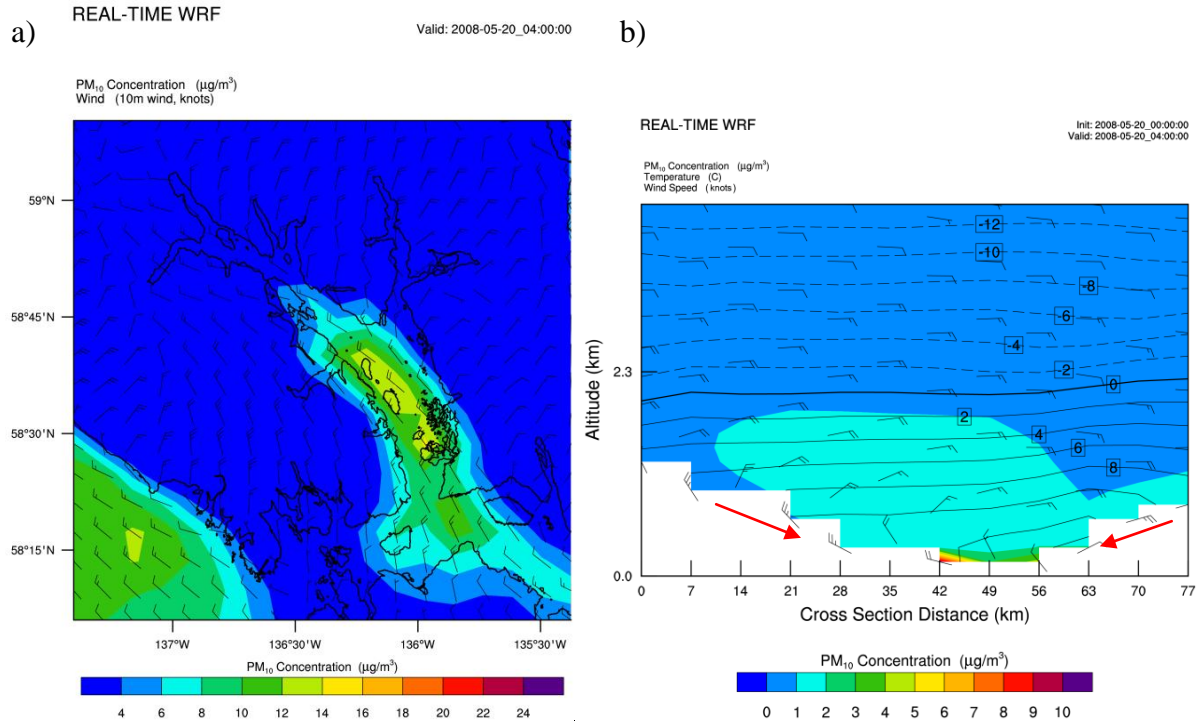

Figure 4.26 a) 1100 UTC May 20 (0200 AST May 20) zoomed-in contour and b) cross section. These plots show how PM_{10} concentrations gradually diminish after the second cruise-ship entry. Slight downsloping winds leads to the development of a cold pool (where isotherms slightly sag) during the nighttime hours due to radiation cooling on the mountain slopes.

4.4.6 May 27-28 Event

      The May 27-28 event shows high levels of particulate matter and strong modeled inversions inside Glacier Bay. Concentrations of PM_{10} begin high (> 20 µg m^{-3}), especially outside of Icy Strait into the Gulf of Alaska early in the day (Fig 4.28). At 0500 AST, winds were calm inside most portions of the park, especially in sheltered locations deeper in the bay. Wind speeds increased to 15-20 knots in the open waters of the Gulf of Alaska. There was some advection of pollutants through Icy Strait at this time, which is likely why the day began with high concentrations of PM_{10}. By 1500 AST, it was hard to differentiate pollution emitted from the cruise-ships in Glacier Bay, although there were two ships that entered the park, and three additional ships passing in the vicinity. By midday (Fig 4.29), PM_{10} concentrations were high (12-14 µg m^{-3}) towards the entrance of the park.

      As midnight approached, particulates largely dispersed after the ships departed Glacier Bay, but pollution remnants of approximately 6-8 µg m^{-3} remained trapped due to persistent inversions. With weak to no WRF/Chem simulated winds deeper in Glacier Bay, the model may have not been able to simulate the spread of PM_{10} concentrations deeper in the bay. The average inversion height and strength was 1.24 K (100 m)$^{-1}$ and 129.2 m, respectively. Inversions were strong (up to 6.7 K (100 m)$^{-1}$) and thick during this event, with inversions spanning up to the first four WRF/Chem levels (402 m), especially in locations close to the entrance of the park. This may be indicative of a subsidence inversion, as result of a stable marine boundary layer. Figs 4.28-4.30 show that winds inside Glacier Bay were calm (generally less than 5-10 knots), as a high pressure system remained relatively stationary in the North Pacific and Gulf of Alaska. WRF/Chem data shows some areas deeper inside Glacier Bay had 0 knot wind speeds.

      Strong inversions again kept cruise ship plumes contained during this event. The average PM_{10} concentration close to the surface was approximately 10.3 µg m^{-3}. Above any inversion levels of around 1 km, the concentrations rapidly diminished to pristine conditions of 1.4 µg m^{-3}.
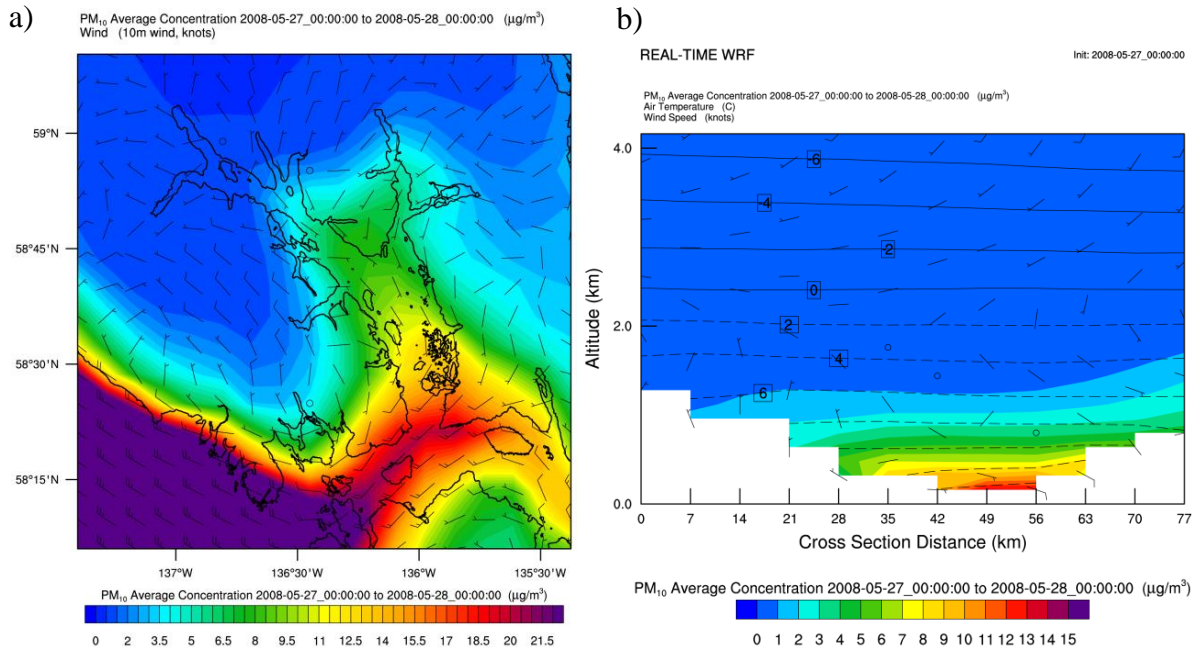
Figure 4.27 a) Daily average zoomed-in contour plot and b) cross section for May 27, 2008. This period occurs at the beginning of the tourist season, and depicts a day with strong inversions, two ships in the bay, and three passing by.
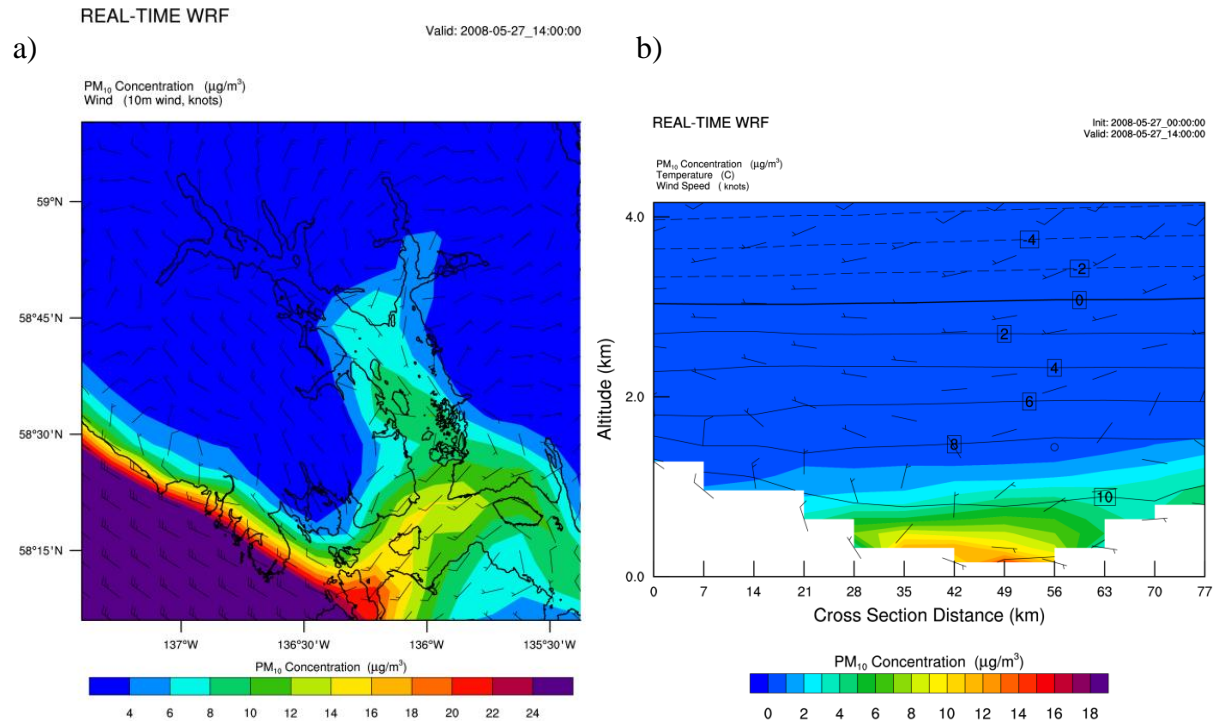
Figure 4.28 a) 1400 UTC (0500 AST) May 27 zoomed- in contour and b) cross section. These plots show the PM_{10} concentration before the cruise-ship entry, plus advection of PM_{10} from ships passing by Glacier Bay.
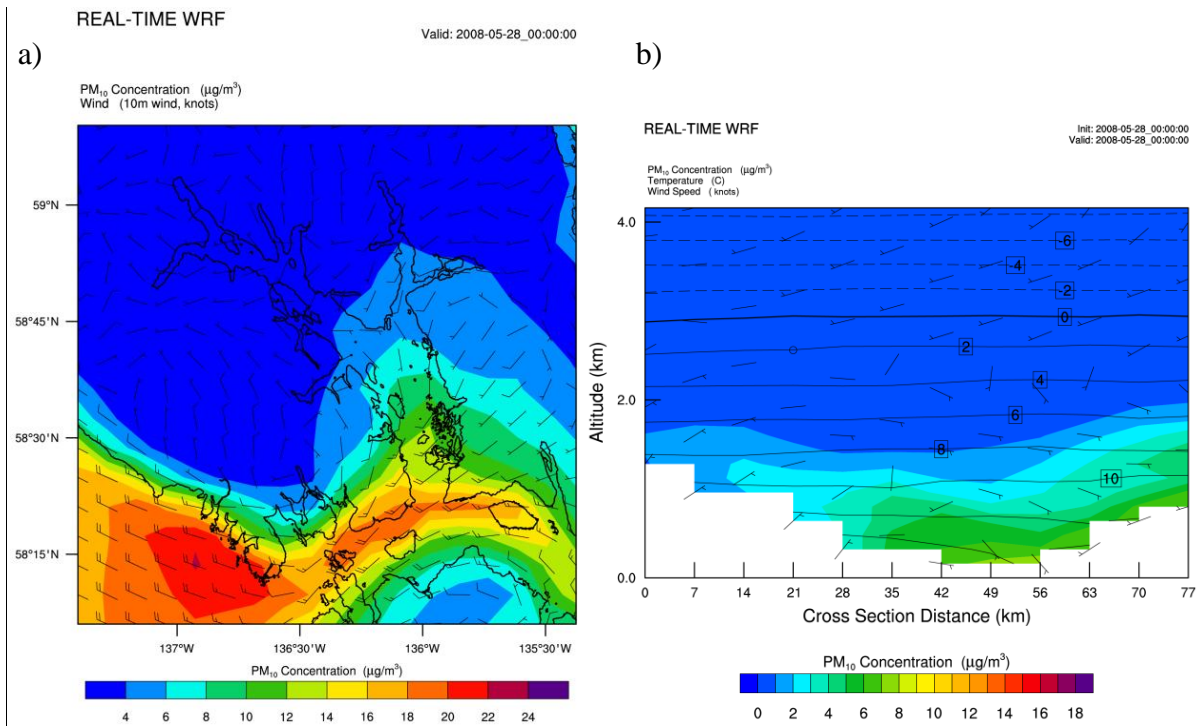
Figure 4.29 a) 0000 UTC May 28 (1500 AST May 27) zoomed-in contour and b) cross section. These plots show the PM_{10} concentration while a ship was in the bay. Note that winds are very calm, potentially indicative of a subsidence inversion.
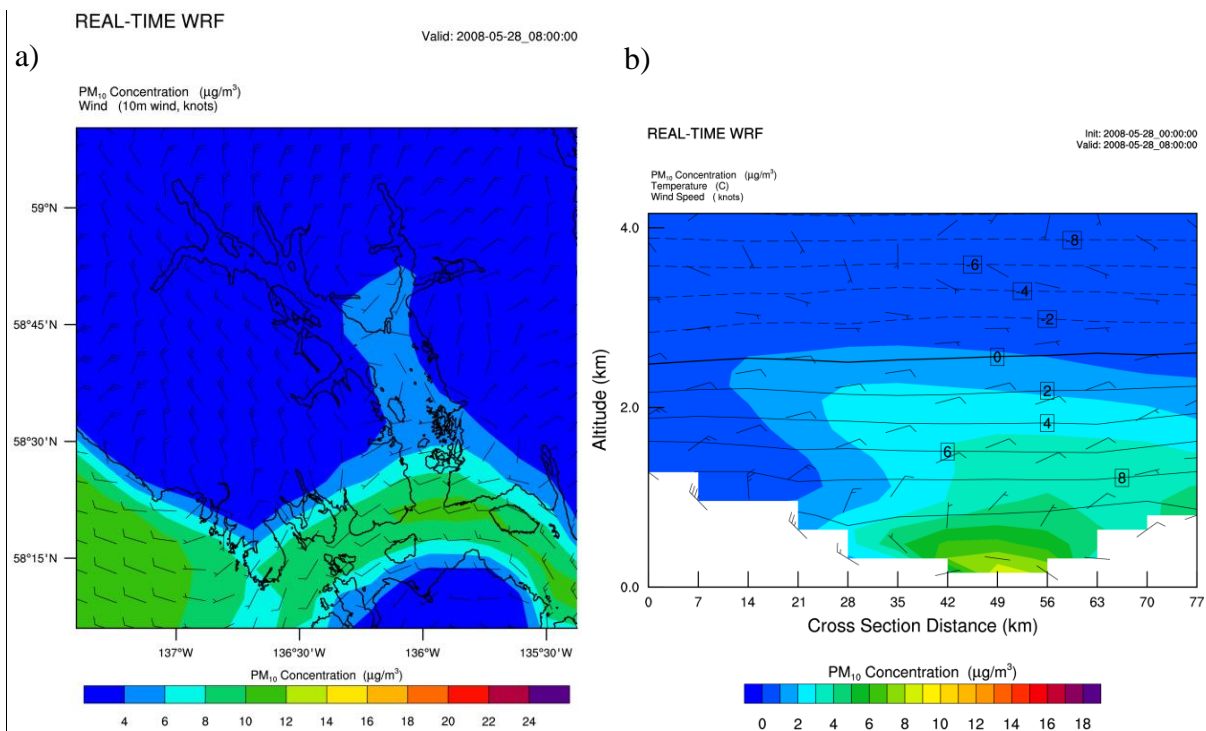
Figure 4.30 a) 0800 UTC May 28 (2300 AST May 27) zoomed-in contour and b) cross section. These plots show the PM_{10} concentrations after the ships departed Glacier Bay.

4.4.7 August 13-14 Event

The August 13-14 event demonstrates the second highest PM_{10} concentration day of the tourist season, with the absence of an inversion due to windy conditions associated with a large 980 hPa low-pressure system over the Gulf of Alaska. This storm resulted in intense orographic lifting, which is common in a region with such great vertical relief (Fig. 4.31). Orographic lifting occurs when an air parcel is forced from a low elevation to a higher one over steep terrain. When the parcel rises, it cools adiabatically and may produce clouds and precipitation if the parcel becomes saturated.

The average concentration of PM_{10} in most places in Glacier Bay reached upwards of 15 $\mu g\ m^{-3}$ with much higher hourly averages (up to 24 $\mu g\ m^{-3}$ by 1500 AST). This day included two cruise-ship entries in the park, with an additional ship passing in the vicinity. High pollutant concentrations from ship traffic in the Gulf of Alaska was present (> 30 $\mu g\ m^{-3}$), despite wind speeds upwards of 25 knots (12.9 m/s). PM_{10} concentrations may have also been elevated due to sea spray associated with the area of low pressure. Sea salt particles are considered one of the largest natural contributors to global aerosol budget (IPCC 2001).

Concentrations of PM_{10} began strong by 0200 AST (up to 20 $\mu g\ m^{-3}$), and a ship appears to be visible with a small 24 $\mu g\ m^{-3}$ bull's-eye of PM_{10} off Pleasant Island near the entrance of Glacier Bay (Fig. 4.33). Strong winds from the southeast around 25 knots were advecting pollution from the Chatham Strait and points eastward. Pollution from the Gulf of Alaska was negligible at this time. By 1500 AST, high concentrations of PM_{10} (> 24 $\mu g\ m^{-3}$) were visible east of Hugh Miller Inlet as the cruise-ship entered the park (Fig. 4.34). For location of geographic features, see Fig. 2.11.

By 0100 AST the following morning (Fig. 4.35), it appeared as though pollutants from regions of high ship traffic outside Glacier Bay became advected over the Fairweather Mountain Range after the cruise-ships had left the park. Wind speeds at 0100 AST approached upwards of 30-40 knots (about 15.4-20.6 m/s) over the Fairweather Range (Fig. 4.35 in both cross section and contour plot). This orographically forced lifting aided in the spreading of additional pollutants inside Glacier Bay. At this time, PM_{10} was still high in Glacier Bay from ships earlier in the day. The zoomed-in cross section shows high concentrations towards the left side of Glacier Bay (towards the southwest) descending down the mountains. Although the steep

121

mountain terrain is smoothed in WRF/Chem, the advection of PM_{10} is a potential geographically forced threat for pollutant transport during certain synoptic situations.

Pollution also remained contained very close to the surface during this event. The average PM_{10} concentration where ships travel was roughly 16.8 µg m^{-3}. At 1 km height, the PM_{10} concentrations subsided to pristine conditions of 1.1 µg m^{-3}.
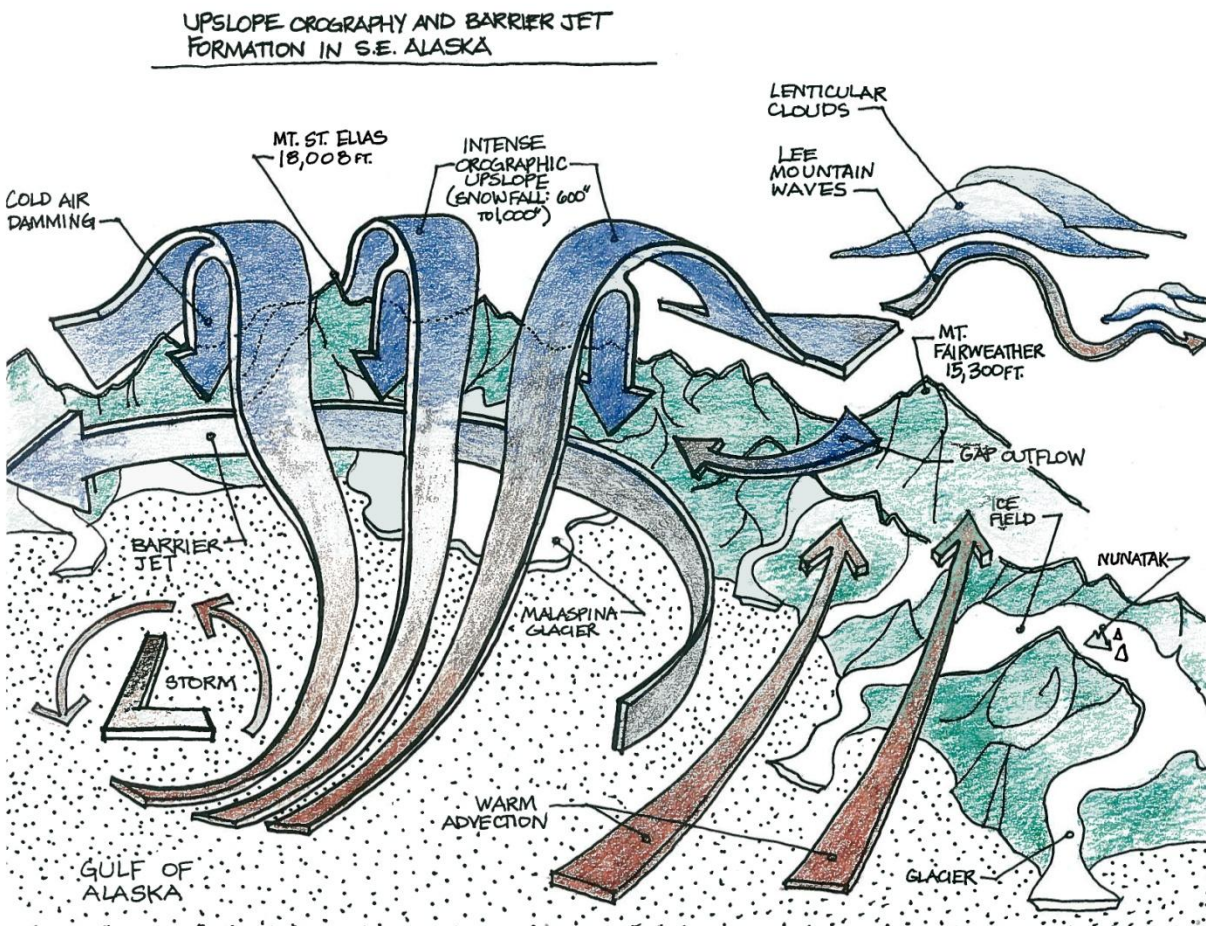
Figure 4.31 Artist's rendering of orographic lifting of air over the Fairweather and Coastal Mountain Ranges of Southeast Alaska. Glacier Bay is on the opposite side of these mountains. Strong orographic lifting is induced by low pressure systems in the Gulf of Alaska. Strong winds from these storms are forced up and over the mountains, some of which have one of the most intense vertical reliefs in the world (Used with permission from: Derek P. Starkenburg).
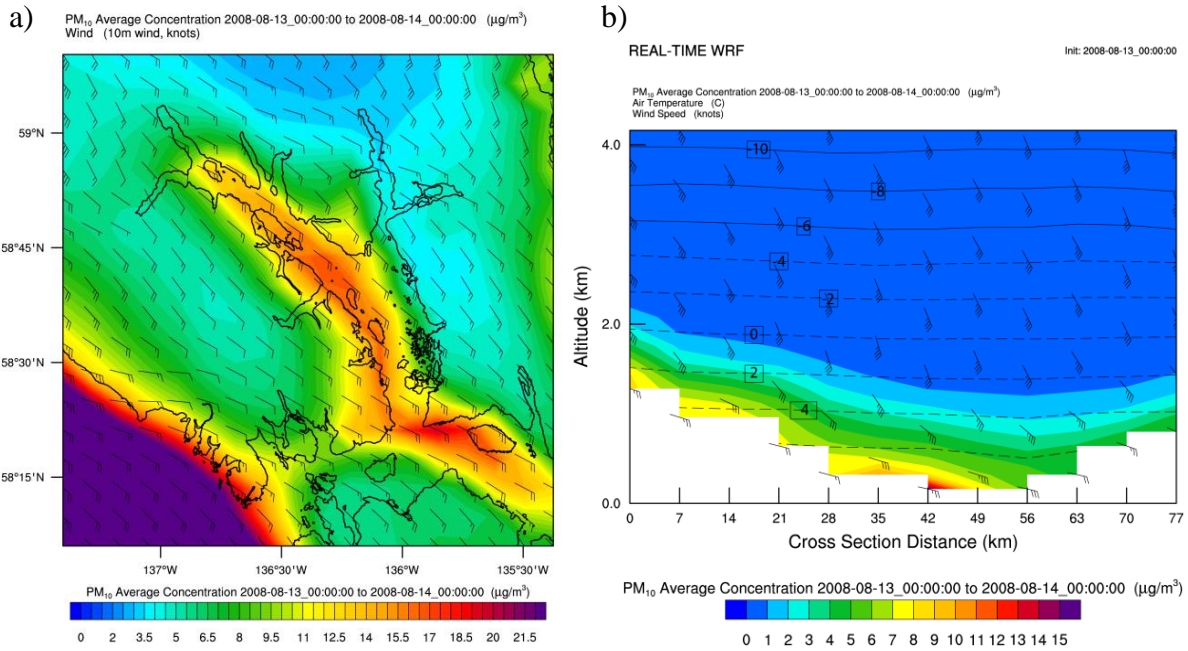
Figure 4.32 a) Daily average zoomed-in contour and b) cross section for August 13, 2008. This is the second highest day of pollution, and illustrates a day with no inversions, two ships in the Bay, and one passing by. There is a low-pressure system in the area, and frequent ship traffic produces high concentrations of PM_{10} off the coast.

Figure 4.33 a) 1100 UTC (0200 AST) August 13 zoomed-in contour and b) cross section. These plots show the PM_{10} concentrations before the ships entered. PM_{10} concentrations were already high due to advection. The pollutants become mixed out for a few hours, which can be seen in this cross section. This was temporary until the wind shifted from the southeast to the southwest later in the day and orographically lifted in more PM_{10}.

123

Figure 4.34 a) 0000 UTC August 14 zoomed-in contour and b) cross section (1500 AST August 13). These plots show the PM_{10} concentration while the ship was in the bay.

Figure 4.35 a) 1000 UTC (0100 AST) August 14 zoomed-in contour and b) cross section. These plots show the PM_{10} concentrations after the cruise-ships departed Glacier Bay. Concentrations become high through an orographically forced lifting of PM_{10} over the Fairweather Range, as denoted by the red ovals. This occurs as the wind shifts towards the south.

4.4.8 September 3 Event

The final event of this discussion, from September 3, is used to demonstrate a typical particulate matter day in Glacier Bay. Two cruise-ships visited the park this day, as well as two additional ships passed nearby. Average daily concentrations of PM_{10} inside Glacier Bay were around 5 μg m^{-3} with equal dispersal throughout the park, except for the Northeast Fork. The air was relatively clean (< 2 μg m^{-3}) on September 3 at 0600 AST (Fig. 4.37), but by 1400 AST (Fig. 4.38) a ship was evident because PM_{10} concentrations increased. By 1800 AST, the pollution dispersed out of the bay and the air remained clean for the rest of the day (Fig. 4.39). Wind direction in the Gulf of Alaska outside of Glacier Bay was largely from the southeast or east-southeast, keeping pollution from the shipping lanes from entering Icy Strait. The 1200 UTC (0300 AST) September 3 surface analysis shows the Alaska Panhandle between a high pressure system in southern British Columbia and low pressure centered over Kodiak. The resultant wind direction makes sense for what WRF/Chem simulated inside Glacier Bay, as winds typically flow counter-clockwise around a low.

The average daily concentration of PM_{10} close to the surface was elevated to 4.1 μg m^{-3} from the cruise ships, but reduced rapidly to 0.3 μg m^{-3} above 1 km in height.
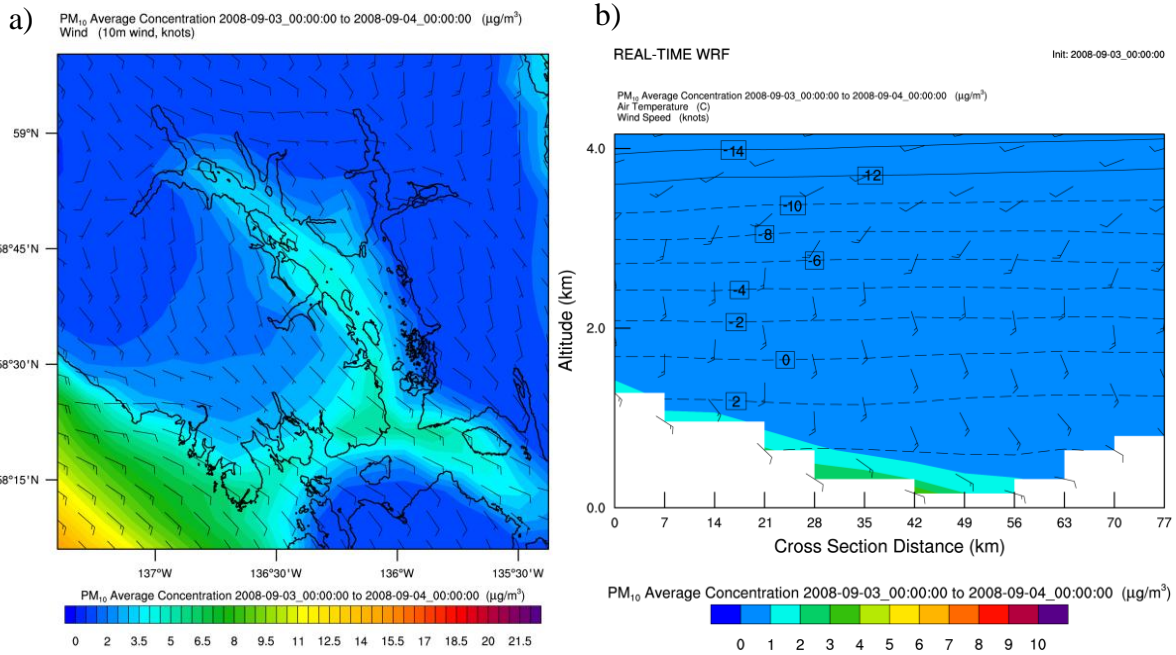
Figure 4.36 a) Daily average zoomed-in contour plot and b) cross section for September 3, 2008. This shows a day of typical average PM_{10} concentrations, no inversions, two ships in the park, and two passing by.
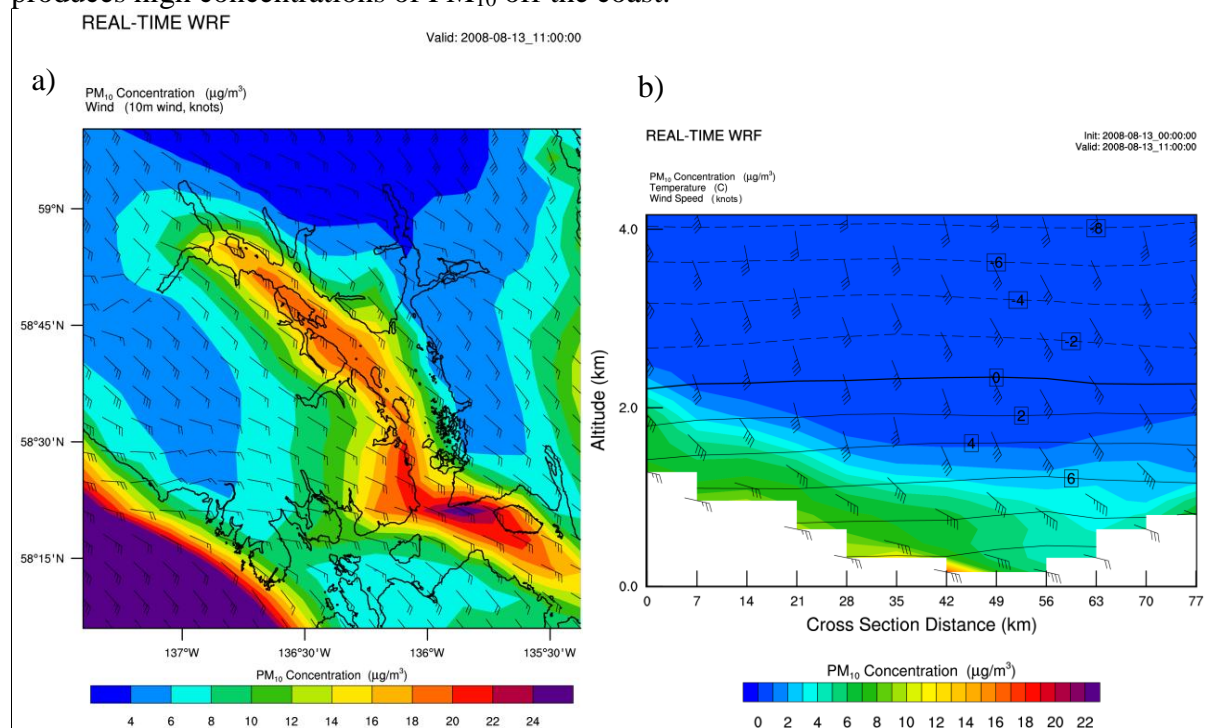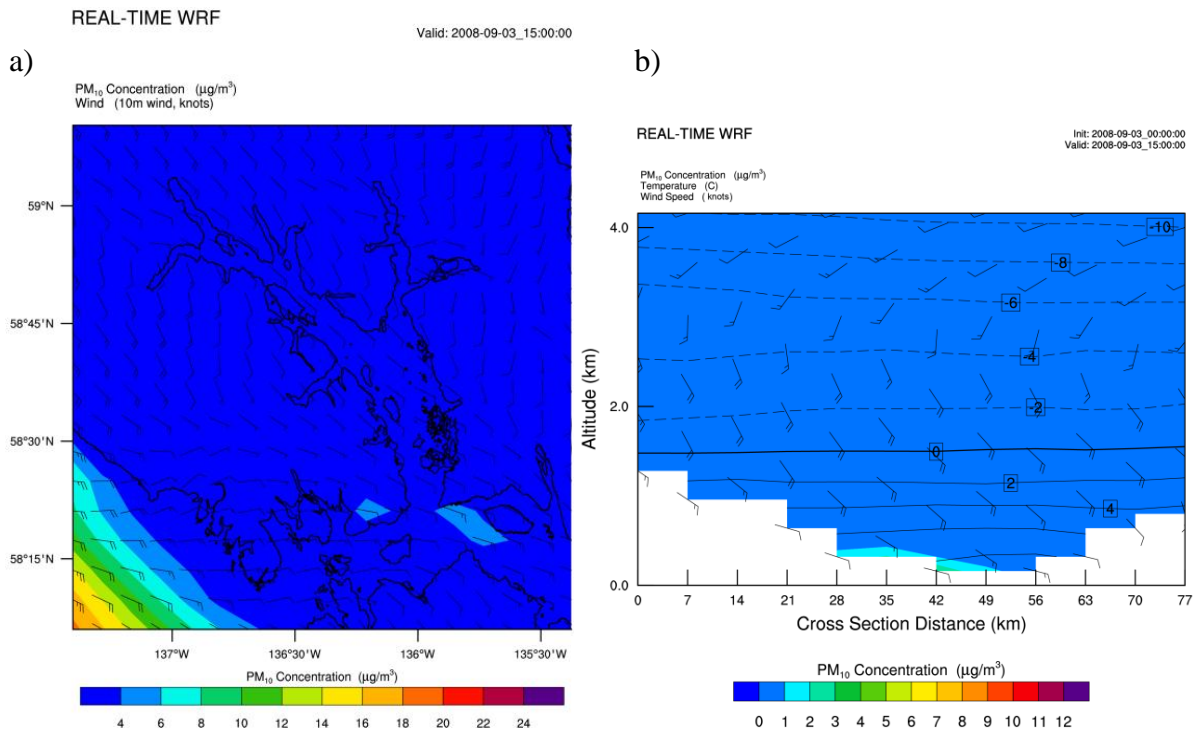

Figure 4.37 a) 1500 UTC (0600 AST) September 3 zoomed-in contour and b) cross section. These plots show the PM_{10} concentration before the ships' entry.
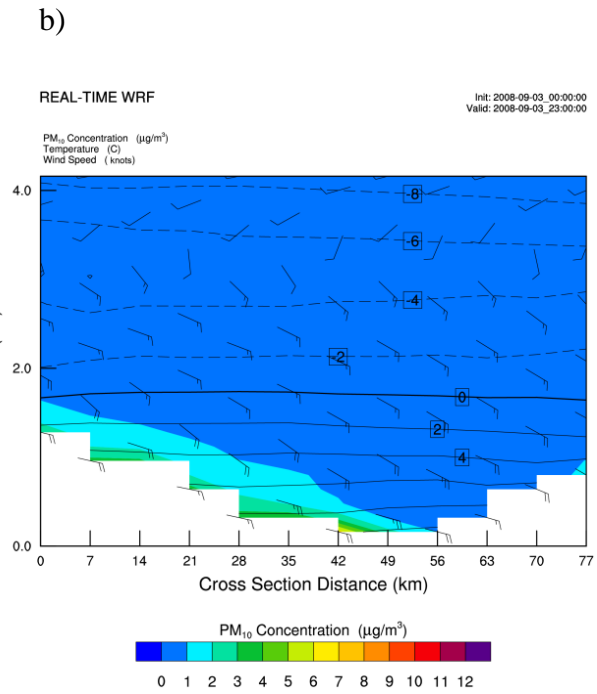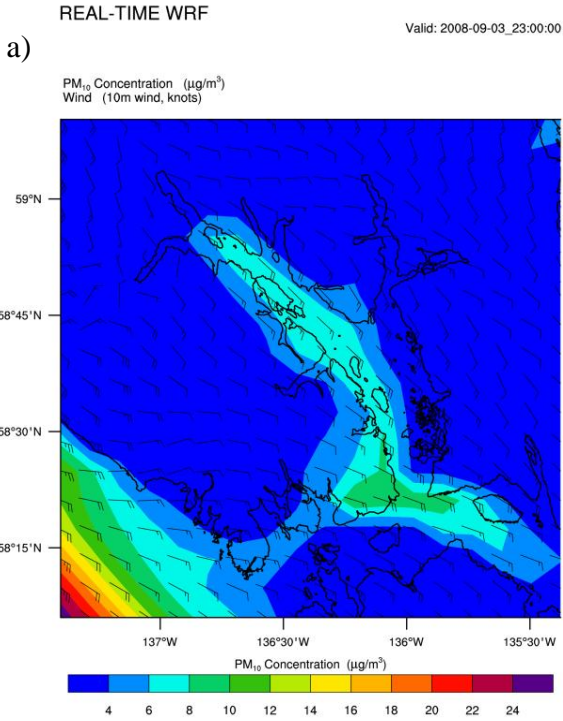
Figure 4.38 a) 2300 UTC (1400 AST) September 3 zoomed-in contour and b) cross section. These plots show the PM_{10} concentration while the ship was in the bay.
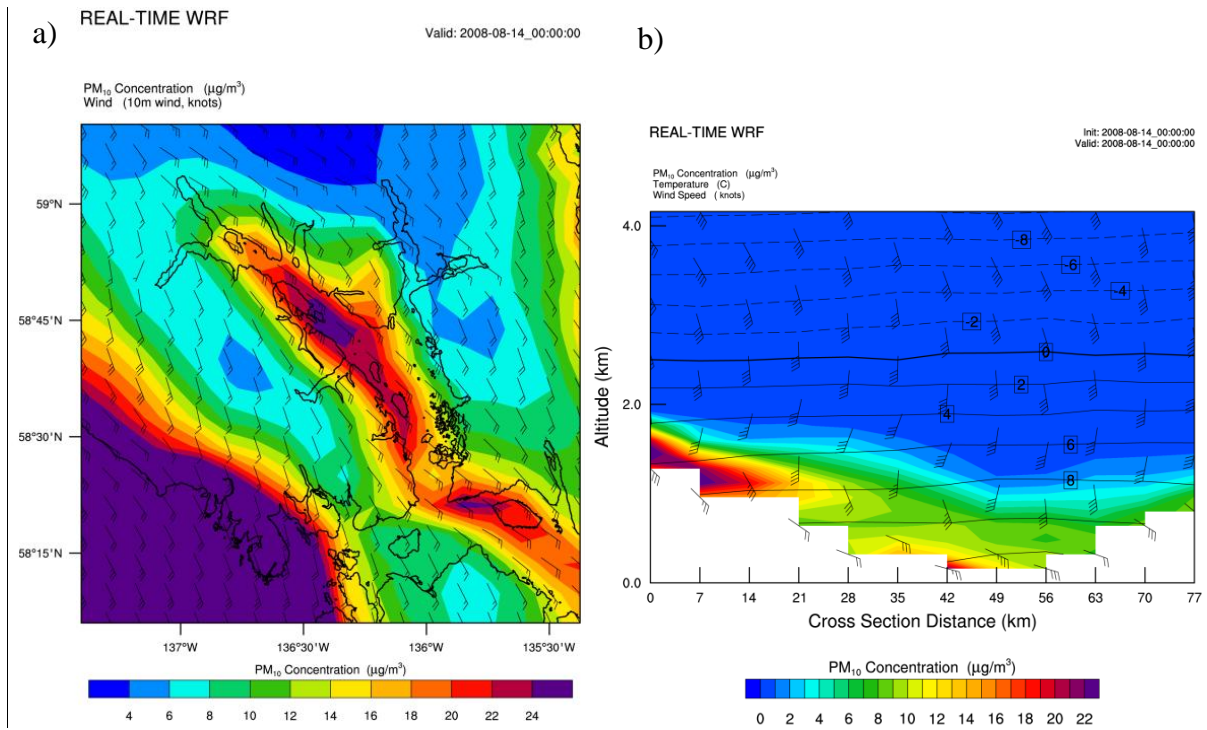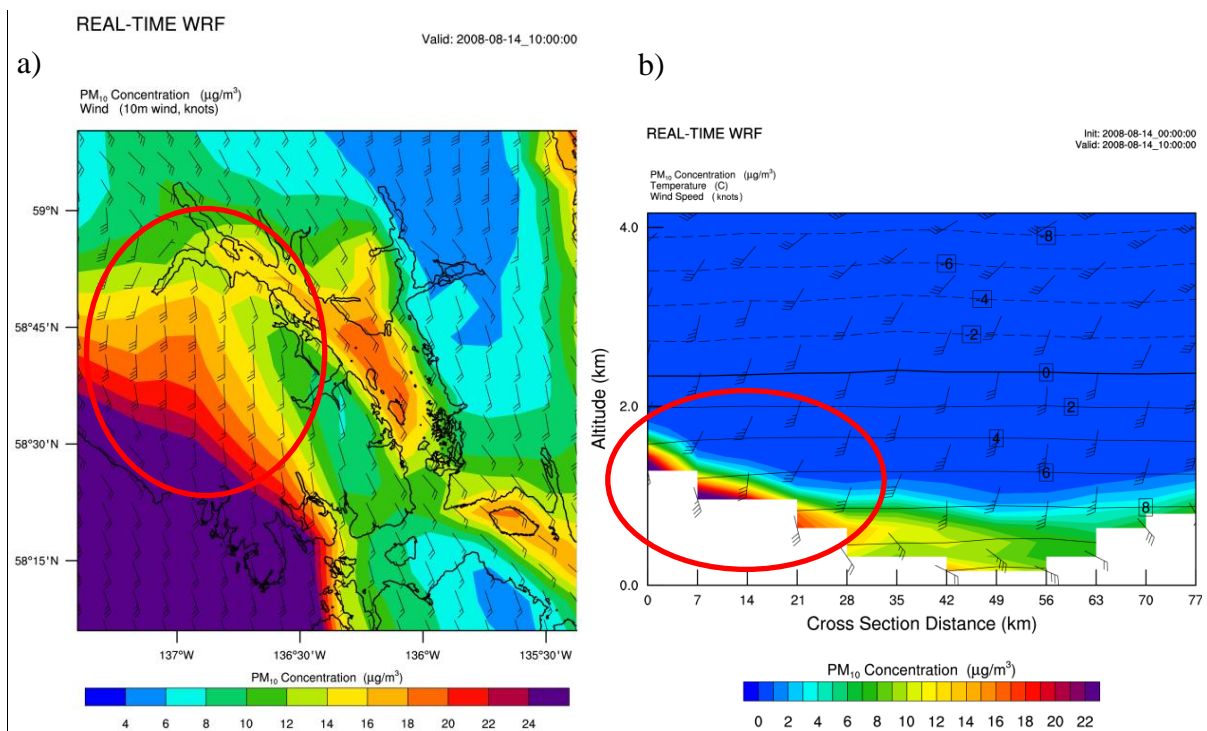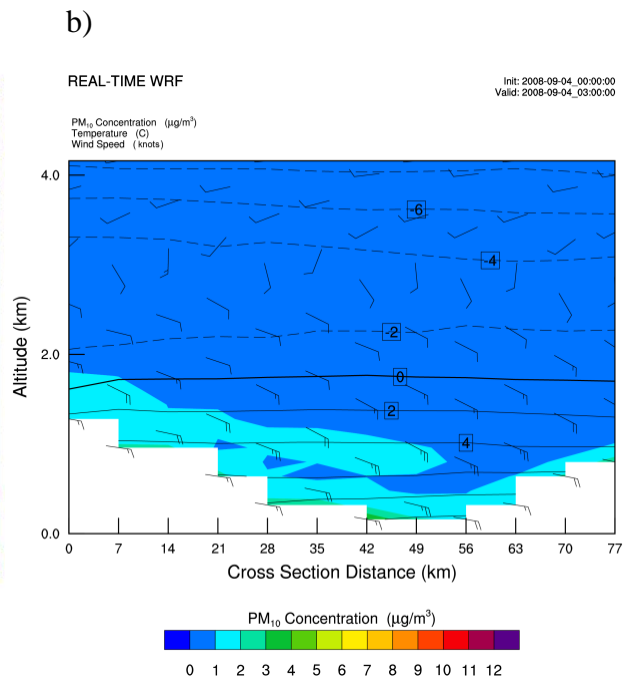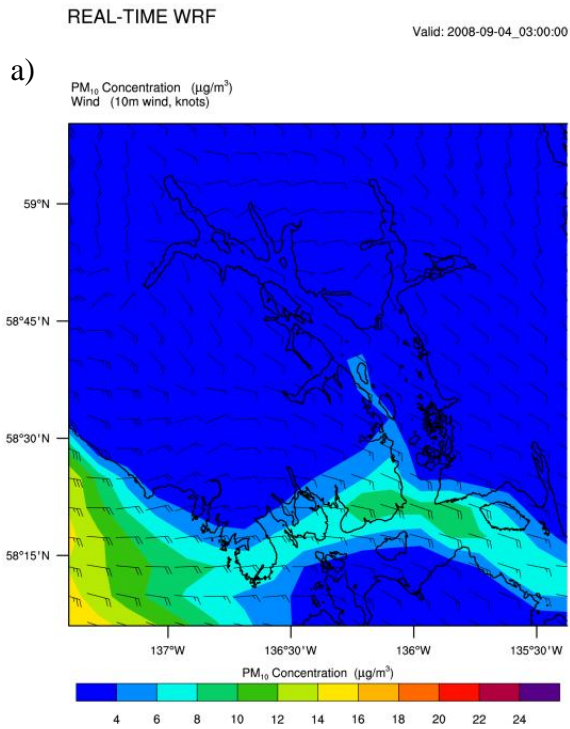

Figure 4.39 a) 0300 UTC September 4 zoomed-in contour and b) cross section (1800 AST September 3). These plots show the PM_{10} concentrations after the ships departed Glacier Bay.

4.4.9 Particulate Matter Conclusions

An activity-based cruise-ship emission inventory and WRF/Chem simulations (Mölders et al. 2013) were used to assess PM_{10} concentrations in Glacier Bay. During most situations, individual cruise-ship plumes were evident. WRF/Chem tended to show stronger advection of pollutants with gusty winds compared to calm winds. The winds appear to draw in PM_{10} from locations outside of Glacier Bay, particularly off the coast in the Gulf of Alaska.

When winds are from the southwest, advection of high concentrations of particulates through Icy Strait tends to occur, and the pollutants frequently reach portions of lower Glacier Bay. Winds from the southeast may advect ship pollution from Chatham Strait, an important ship travel corridor of the Inside Passage. If winds are calm, pollutants do not spread throughout the entire park. Cruise-ship plumes are more likely to remain close to where they were emitted during calm winds, especially if an inversion is present.

Unless concentrations are elevated due to cruise-ships (typically > 10 µg m^{-3}), the furthest inlets keep from experiencing some of the highest pollution. This behavior may be due to topographical or resolution issues in the model as Glacier Bay becomes narrower. WRF/Chem especially keeps higher concentrations of PM_{10} from penetrating the Northeast Fork (Muir Inlet). Weak wind speeds tend to cause PM_{10} levels to linger longer than with stronger winds, especially during inversion events. Regions of frequent inversions (towards the entrance and middle portions of the bay) were also prone to higher PM_{10} concentrations than deeper regions in the bay, which were due not only from cruise-ships passing through the same location twice, but also from particulates that were transported from areas outside Glacier Bay. Inversions trap cruise-ship pollution, as relatively pristine air of 1-2 µg m^{-3} typically exists above 1 km. Elevated levels of PM_{10} are commonly the result of cruise ships, as a simulation without ship emissions showed that background concentrations of PM_{10} are commonly less than 0.3 µg m^{-3}.

Chapter 5 Conclusions

Glacier Bay National Park and Preserve encompasses 13,287 km^2 of remote, pristine wilderness. Glacier Bay is nestled between the Saint Elias, Takhinsha, and Fairweather Mountain Ranges, and is home to fifteen tidewater glaciers. No roads lead into or out of the park. The nearest area of civilization is located a few kilometers to the east of Glacier Bay's entrance in the tiny town of Gustavus (429 inhabitants), with access to Bartlett Cove inside the National Park boundaries. The park has largely remained untouched to anthropogenic influences, although it has become a major destination for cruise-ship companies between ports-of-call. The summer tourist season, which typically operates from May 15 to September 15 each year, attracts visitors from all corners of the globe to take in the park's natural beauty.

Currently, The National Park Service restricts cruise-ship entries at a maximum of two ships per day. The goal of the Park Service is to keep environmental conditions pristine while also providing visitors with a good experience. However, some visitors have expressed concern of increased pollution resulting in decreased visibility from cruise ship exhaust. During periods of quiet weather, temperature inversions develop in Glacier Bay, trapping pollutants and reducing visibility (Mölders et al. 2013). With the absence of winds or storm systems to stir stagnant conditions, an inversion may exist for hours or several days in Glacier Bay, and can trap pollution until air becomes recirculated.

The Weather Research and Forecasting Model, inline coupled with a chemistry package (WRF/Chem; Grell et al. 2005; Peckham et al. 2011) and emissions obtained from an activity-based cruise-ship emission inventory, was run during the 124 day tourist season of 2008 to understand inversion formation, frequency, strength, location, and duration inside Glacier Bay. In addition, WRF/Chem was used to simulate inversions' impacts on pollution from cruise-ship emissions inside and outside of Glacier Bay. Very few modeling studies have been done in Alaska, let alone Glacier Bay, and physical observations are practically non-existent. Thus, this analysis of the WRF/Chem data provides a first glimpse on particulate matter distributions and inversions in Glacier Bay.

The WRF/Chem simulation results were compared to data at 42 meteorological sites within the domain of Southeast Alaska. A variety of sources, including 24 NCDC sites, eleven buoys, and seven Alaska Department of Transportation Road Weather sites were used for

evaluation. This data was used to assess how well WRF/Chem was able to reproduce observed weather. It was found that the model was able to capture the temporal evolution and general weather pattern accurately. Thus, I conclude that the model data serves as a useful tool in understanding meteorological processes in this area, especially since physical and chemical observations are not present in Glacier Bay.

The model performed well in estimating surface temperature, dew-point temperature, and sea-level pressure, but tended to slightly underestimate them (e.g. -0.6 K,-0.2 K, and -0.89 hPa, respectively). WRF/Chem slightly overestimated relative humidity (2.2%), wind speed (1.75 m/s), and wind direction (6°) by small quantities. Discrepancies regarding the major errors could be attributed to terrain influences and model assigned land-use type. Southeast Alaska has some of the most rugged mountains in the world, with intense vertical relief that projects upwards of 3000m directly from sea-level.

To understand the performance of simulating the vertical profiles, WRF/Chem modeled profiles were compared with Yakutat radiosondes for the entire summer tourist season. In general, the model captured most of the profiles well, especially the temporal evolution of the entire upper air profile for the four meteorological variables: temperature, dew-point temperature, wind speed, and wind direction, with respective correlations of 0.85, 0.60, 0.69, and 0.66. It overestimated temperature and dew-point temperature by small margins (0.1 K and 0.8 K, respectively). There was very little, if any, overall wind-speed bias, and a small negative wind directional bias of -11°. Correlations between simulated and observed quantities tended to increase with height. A small area of missing data occurred at approximately 600 m. Having this data would have been useful to make additional conclusions about inversion prediction accuracy.

Errors could be the result of topographical discrepancies, wet radiosonde sensors, or natural balloon drift outside of the WRF/Chem vertical grid-cell column. Since I found that WRF/Chem was able to decently simulate the meteorology, with errors on par with other WRF modeling studies, I conclude that the WRF/Chem results are an excellent tool to understand atmospheric processes in Glacier Bay that we cannot otherwise quantify due to lack of observations.

After analyzing the WRF/Chem data with respect to its performance through surface and upper air validation methods, as well as through the analysis of synoptic patterns when inversions are expected to occur, the *null* hypothesis may be rejected. It is clear that interactions

between large-scale synoptic scale meteorology and mesoscale processes strongly determine the fate of pollutants from ship emissions in Glacier Bay. Inversions commonly develop from stagnant conditions and lack of turbulent flow inside Glacier Bay. Analyses of surface maps confirmed that periods of high pressure systems, which were most prominent during the beginning of the tourist season, resulted in frequent inversion formation. May (albeit only 17 days were examined in this thesis) saw the highest number of inversions (Table 4.2) of all months in the tourist season. By August and September, a more frequent and intense weather pattern set up inside the Gulf of Alaska due to the enhanced temperature contrasts between land and ocean.

There were instances of inversions throughout the 27 grid-cells representing Glacier Bay from 23 to 85 days of the 124 day tourist season, with an overall average of 52 days across the entire bay (Fig. 4.6). The highest frequency of modeled inversions occurred towards the entrance and middle portions of Glacier Bay. This area is where the bay is the widest, and simulated inversion formation may be influenced by the treatment of topography in WRF/Chem.

On days with inversions, the average inversion height and strength across the Glacier Bay during the entire tourist season was 92.5 m and 1.19 K $(100 \text{ m})^{-1}$, respectively. Inversion frequency generally increased throughout the nighttime and early morning hours when the radiation balance was negative. Differing results between various grid-cells may be attributed to terrain and/or advection from neighboring grid-cells. Also drag coefficients differ with land-use classification. An underestimation of inversion events may be the result of the overestimated wind speeds (1.75 m/s on average). A consistent overestimation of wind has been documented by many other WRF studies (e.g.: Zhang et al. 2009; Zhao et al. 2011; Mölders et al. 2012; 2013; Ngan et al. 2013).

WRF/Chem shows notable impacts regarding PM_{10} emitted from cruise-ships inside Glacier Bay. Hourly concentrations do not exceed more than 50 μg m^{-3} inside the park, which is considerably below the 24 hour daily average National Ambient Air Quality Standards (NAAQS) of 150 μg m^{-3} set by the EPA. Daily concentrations are even lower (< 30 μg m^{-3}), as cruise-ships do not spend more than half of the day inside Glacier Bay. In Alaska federally mandated Class I areas, such as those in the maritime regions at the Simeonof and Tuxedni IMPROVE aerosol monitoring sites, typical PM_{10} concentrations are < 6 μg m^{-3}. The Denali IMPROVE site may have PM_{10} concentrations < 1-2 μg m^{-3} when no wildfires are burning.

Using the average observed concentration of 6.72 µg m^{-3} at the Class I maritime sites from the Porter (2009) study, and assuming an ABL height of 1 km with background concentrations of 0.1 µg m^{-3} above that level, a vertically integrated value of approximately 6000 µg m^{-2} would result for pristine air. This is what a satellite would see if it took measurements with a radiometer sensitive to PM$_{10}$.

Most inversions existed very close to the surface. To understand how strongly inversions trap pollutants, a comparison was made between the environmentally pristine air (which is typically on the order of about < 1-2 µg m^{-3}) above most inversion levels (around 1 km) to the value close to the surface where the cruise ships travel. During the highest pollution event, the daily average PM$_{10}$ concentration close to the surface was 20.5 µg m^{-3}. The concentration above any inversion levels was 6.6 µg m^{-3}, and PM$_{10}$ concentrations continued to reduce rapidly with height. On another day with strong inversions and two cruise ship visits, the average PM$_{10}$ concentration close to the surface approximately 4.8 µg m^{-3}. Above any of the inversion levels around 1 km, concentrations rapidly diminished to pristine conditions of 0.9 µg m^{-3}.

Despite the entry of cruise-ships, Glacier Bay still has pristine air, untouched by other anthropogenic effects (i.e. power plants, automobiles, manufacturing, etc.). The elevated PM$_{10}$ concentrations due to cruise-ships are only temporary until particles settle, or air is recirculated, thereby breaking an inversion or augmenting the direction of pollutants from other locations.

The model simulations show that pollution from highly traveled shipping lanes used by cruise ships and ferries, such as the Alaska Marine Highway system, can advect PM$_{10}$ into portions of the park under certain synoptic conditions. When winds are from the southwest, WRF/Chem tends to waft elevated concentrations of particulates through Icy Strait, and frequently into portions of lower Glacier Bay. The model also favors keeping some of the highest pollutants from reaching the deepest fjords and inlets (Fig. 4.27). This feature may be due to model resolution, or the fact that terrain tends to be smoothed (i.e. the steep mountains surrounding small fjords are not resolved by the model). Many of these inlets are subgrid-scale in width, making it impossible for WRF/Chem to accurately simulate processes in these grid cells.

A higher resolution simulation could shed some light on the currently unresolved mesoscale-γ meteorological processes. However, WRF/Chem was able to capture a mesoscale circulation inside of Glacier Bay (Fig. 4.24). Daytime heating on the mountain slopes led to gentle upslope winds, but the spreading of particles was hindered by an inversion. WRF/Chem

was also able to show orographically forced lifting of PM_{10} from regions of high ship traffic in the eastern Gulf of Alaska over the Fairweather Mountain Range into Glacier Bay (Fig. 4.35).

All waters 200 miles off the coast of North America were designated emission control areas (ECAs) in 2010. Once implemented in 2016, cruise-lines will need to reduce fuel sulfur content to 0.1% of 1000 ppm, and lower NO_x emissions by 80%. Mölders et al. (2013) showed that an ECA would result in the largest improvement in air quality (74% reduction in PM emissions) and visibility in Glacier Bay, as opposed to keeping conditions the same, increasing ship speed to 20 knots, or limiting the speed to 13 knots. It would be interesting to study Glacier Bay after these mandatory emission changes are implemented.

It is clear that Glacier Bay needs a way to start documenting in-situ weather observations. While a network of monitoring stations will be costly and potentially unwieldy for the experience of guests, who expect to see untouched natural beauty, direct observations would provide much needed atmospheric information to Park Rangers and researchers. The sites could help the National Park Service monitor weather conditions further inside Glacier Bay, and even aid in management decisions.

Benson et al.'s (1978) study suggested, based on local and limited data, that conditions within the fjords differ appreciably from the nearest meteorological sites, such as those in Gustavus or Juneau. These results have been confirmed by my analysis. The authors also noted that Glacier Bay is extremely sensitive to ship-emitted pollutants because of highly stable conditions. More scientific information is necessary to deal with the problem. They suggested the need for basic, long-term meteorological data in the fjords, pollution monitoring sites, and more detailed micrometeorological studies (Benson et al. 1978). My study also shows the urge for a dense measurement network, as the simulations show that local effects play a large role.

Little has been done in the past 35 years since this University of Alaska-Fairbanks Geophysical Institute report was compiled by Benson et al. While the weather obviously cannot be changed (thus, we need to adapt to the problem), there are some steps we can take to mitigate and better understand the pollution and weather inside Glacier Bay. The future ECA rules should drastically limit pollution levels inside the bay, and some ships already use low-sulfur fuel inside Glacier Bay. The presence of a meteorological and air quality monitoring network is an absolute necessity. However, the site locations should be selected so that they minimize the visible detraction to tourists, and are most suitable to gain understanding for research and monitoring

purposes. These sites could include buoys or remote land-based sensors away from the tourists' typical viewpoint. They could be self-sustaining, powered by solar energy with auxiliary backup batteries, and remotely uplink the data to an archive. If that is not possible, vessels, including cruise-ships, could provide detailed mobile weather information to the National Weather or Park Service. Since ships spend upwards of 8-12 hours inside Glacier Bay, their stay could provide a significant amount of data. In addition, Park Service employees could document weather conditions aboard cruise-ship trips after they are picked up from Bartlett Cove.

Cruise-ship travel remains a popular way for tourists to visit coastal regions of Southeast Alaska, and is not likely to change since most places are remote and inaccessible to vehicle traffic. With over 95% of people visiting Glacier Bay via ship, air pollution concerns due to haze formation on particulate matter will remain high until something is done to change the current situation. Pollution limiting strategies and in-situ measurements can provide valuable ecological and research insight. By understanding the meteorological, physical, and chemical processes behind inversions and ship related pollution concerns in Glacier Bay, the Park Service can continue to provide guests with enjoyable experiences, while also keeping Glacier Bay pristine.

References

Ackermann, I. J., H. Hass, M. Memmesheimer, A. Ebel, F. S. Binkowski, and U. Shankar, 1998: Modal aerosol dynamics model for Europe: Development and first applications. *Atmos. Environ.*, **32,** 2981-2999.

Ahrens, C. D., 1985: *Meteorology Today: An Introduction to Weather, Climate, and the Environment.* 2nd ed., West Publishing Company.

Anthes, R. A., 1983: Regional models of the atmosphere in middle latitudes. *Mon. Wea. Rev.*, **111,** 1306-1335.

Anthes, R. A., Y.H. Kuo, E.-Y. Hsie, S. Low-Nam, and T. W. Bettge, 1989: Estimation of skill and uncertainty in regional numerical models. *Quart. J. Roy. Meteor. Soc.*, **115,** 763-806.

Arakawa, A., and V. R. Lamb, 1977: Methods of computational physics. *Academic Press: New York*, **17,** 174-265.

Benson, C. S., G. Wendler, and R. March, 1978: On the climate and air pollution potential in Glacier Bay National Monument, Alaska. Report to the U.S. National Park Service, Geophysical Institute, University of Alaska Fairbanks, 33 pp.

Benson, C. S., and K. R. Rizzo, 1989: Air pollution in Alaska. *Weatherwise*, **33,** 210-215.

Biello, M. A., 1966: Survey of arctic and subarctic temperature inversions. Technical Report 161, U.S. Army Cold Regions Research and Engineering Laboratory, Hanover, NH, 36 pp.

Binkowski, F. S., and U. Shankar, 1995: The regional particulate matter model, 1. Mode description and preliminary results. *J. Geophys. Res.*, **100,** 26191-26209.

Boé, J., A. Hall, and X. Qu, 2009: Current GCMs' unrealistic negative feedback in the Arctic. *J. Clim.*, **22,** 4682-4695.

Bourne, S. M., 2008: A climate perspective of observed and modeled surface-based temperature inversions in Alaska. M.S. Thesis, Department of Atmospheric Sciences, University of Alaska Fairbanks, 117 pp.

Bourne, S. M., U. S. Bhatt, J. Zhang, and R. Thoman, 2010: Surface-based temperature inversions in Alaska from a climate perspective. *Atmos. Res.*, **95,** 353-366.

Bowling, S. A., 1986: Climatology of high-latitude air pollution as illustrated by Fairbanks and Anchorage, Alaska. *J. Clim. Appl. Meteorol*, **25,** 22-34.

Bridgman, H. A., R. C. Schnell, J. D. Kahl, G. A. Herbert, and E. Joranger, 1989: A major haze event near point barrow, Alaska: Analysis of probable source regions and transport pathways. *Atmos. Environ.*, **23,** 2537-2549.

Brooks, C. E. P., 1931: The vertical temperature gradient in the Arctic. *Meteorology Magazine*, **66,** 267-268.

Brown, M. E., 2008: Impact of local external forcing of the 2006 Augustine volcano eruption on regional weather conditions, M.S. Thesis, Department of Atmospheric Sciences, University of Alaska-Fairbanks, 134 pp.

Buhaug, Ø. et al., 2009: Second IMO GHG Study 2009. Report to the International Maritime Organization, London, England, 240 pp.

Busch, N., U. Ebel, H. Kraus, and E. Schaller, 1982: The structure of the subpolar inversion-capped ABL. *Arch. Met. Geoph. Biocl. A.*, **31,** 1-18.

Chang, J. C., and S. R. Hanna, 2004: Air quality model performance evaluation. *Meteorol. Atmos. Phys.*, **87,** 167-196.

Chen, F., and J. Dudhia, 2001: Coupling an advanced land surface hydrology model with the Penn State/NCAR MM5 modeling system. Part I: model implementation and sensitivity. *Mon. Wea. Rev.*, **129,** 569-585.

Chou, M. D., and M. J. Suarez, 1994: An efficient thermal infrared radiation parameterization for use in general circulations models. NASA Tech. Memo. 104606, Vol. 10, 85 pp. [Available from NASA Center for Aerospace Information, 800 Elkridge Landing Rd., Linthicum Heights, MD 21090]

Collins, W. D., et al., 2004: Description of the NCAR Community Atmosphere Model (CAM 3.0), NCAR Technical Note, NCAR/TN-464+STR, **226**, 214 pp.

Collins, W. D., et al., 2006: The Community Climate System Model Version 3 (CCSM3). *J. Clim.*, **19,** 2122-2143.

Conover, J. H., 1966: Anomalous cloud lines. *J. Atmos. Sci.*, **23,** 778-785.

Contini, D., et al., 2011: The direct influence of ship traffic on atmospheric $PM_{2.5}$, PM_{10} and PAH in Venice. *J. Environ. Manage.*, **92,** 2119-2129.

Cruise Lines International Association (CLIA), 2012: The contribution of the North American cruise industry to the U.S. economy in 2011. *Business Research & Economic Advisors, CLIA August 2012*, 110 pp.

Csanady, G. T., 1974: Equilibrium theory of the planetary boundary layer with an inversion lid. *Boundary-Layer Meteorol.*, **6,** 63-79.

Dalu, G., R. Pielke, R. Avissar, G. Kallos, M. Baldi, and A. Guerrini, 1991: Linear impact of thermal inhomogeneities on mesoscale atmospheric flow with zero synoptic wind. *Ann. Geophysicae,* **9**, 641-647.

Done, J., C. A. Davis, and M. Weisman, 2004: The next generation of NWP: Explicit forecasts of convection using the Weather Research and Forecasting (WRF) model. *Atmos. Sci. Lett.*, **5,** 110-117.

Endresen, Ø., E. Sørgård, J. K. Sundet, S. B. Dalsøren, I. S. A. Isaksen, T. F. Berglen, and G. Gravir, 2003: Emission from international sea transportation and environmental impact. *J. Geophys. Res.: Atmospheres*, **108,** 4560.

EPA (U.S. Environmental Protection Agency), 2010: Designation of North American Emission Control Area to reduce emissions from ships. Office of Transportation and Air Quality, EPA Report EPA-420-F-10-015, 5 pp.

EPA (U.S. Environmental Protection Agency), 2012: Our Nation's Air: Status and Trends through 2010, US EPA Office of Air Quality Planning and Standards, Research Triangle Park, NC, 27 pp.

Etherton, B., and P. Santos, 2008: Sensitivity of WRF forecasts for South Florida to initial conditions. *Wea. Forecasting*, **23,** 725-740.

Eyring, V., H. W. Köhler, J. van Aardenne, and A. Lauer, 2005: Emissions from international shipping: 1. The last 50 years. *J. Geophys. Res.: Atmospheres*, **110,** D17305.

Gabriele, C. M., J. M. Straley, and J. L. Neilson, 2007: Age at first calving of female humpbackwhales in southeastern Alaska. *Alaskan Marine Mammal Science*, **23,** 226-239.

Garratt, J. R., and R. A. Brost, 1981: Radiative cooling effects within and above the nocturnal boundary layer. *J. Atmos. Sci.*, **38,** 2730-2746.

Geiser, L. H., K. L. Dillman, C. C. Derr, and M. C. Stensvold, 1998: Lichens and allied fungi of Southeast Alaska. *Lichenographia Thomsoniana: North American Lichenology in Honor of John W. Thompson*, 24 pp.

Geiser, L. H., and K. L. Dillman, 2012: Likin' the Lichens: What a walk in the woods can tell you about climate and air quality. Paper presented at *Tongass Rainforest Festival*, U.S. Forest Service Pacific Northwest Region Air Program, Petersburg, AK.

Gende, S. M., A. N. Hendrix, K. R. Harris, B. Eichenlaub, J. Nielsen, and S. Pyare, 2011: A Bayesian approach for understanding the role of ship speed in whale–ship encounters. *Ecological Applications*, **21,** 2232-2240.

GINA (Geographic Information Network of Alaska), 2013: MODIS satellite images of Alaska [available online at: http://http://gina.alaska.edu/modis-gallery].

Grell, G., J. Dudhia, and D. R. Stauffer, 1995: A description of the fifth generation Penn State/NCAR mesoscale model (MM5). NCAR Tech Note NCAR/TN-398+STR**,** 138 pp. [Available from NCAR Publications Office, P. O. Box 3000, Boulder, CO 80307].

Grell, G. A., and D. Dévényi, 2002: A generalized approach to parameterizing convection combining ensemble and data assimilation techniques. *Geophys. Res. Lett.*, **29,** 38-31, 38-34.

Grell, G. A., S. E. Peckham, R. Schmitz, S. A. McKeen, G. Frost, W. C. Skamarock, and B. Eder, 2005: Fully coupled "online" chemistry within the WRF model. *Atmos. Environ.*, **39,** 6957-6975.

Grell, G., S. R. Freitas, M. Stuefer, and J. Fast, 2011: Inclusion of biomass burning in WRF-Chem: impact of wildfires on weather forecasts. *Atmos. Chem. Phys.*, **11,** 5289-5303.

Guenther, A. B., P. R. Zimmerman, P. C. Harley, R. K. Monson, and R. Fall, 1993: Isoprene and monoterpene emission rate variability: model evaluations and sensitivity analyses. *J. Geophys. Res.*, **98D,** 12609-12617.

Guenther, A., P. Zimmerman, and M. Wildermuth, 1994: Natural volatile organic compound emission rate estimates for U.S. woodland landscapes. *Atmos. Environ.*, **28,** 1197-1210.

Hand, J. L., et al., 2011: Spatial and Seasonal Patterns and Temporal Variability of Haze and its Constituents in the United States: Report V June 2011, *Interagency Monitoring of Protected Visual Environments*, Cooperative Institute for Research in the Atmosphere, Colorado State University, Fort Collins, CO.

Hewson, M., H. McGowan, S. Phinn, S. Peckham, and G. Grell, 2013: Exploring aerosol effects on rainfall for Brisbane, Australia. *Climate*, **1,** 120-147.

Hines, K. M., and D. H. Bromwich, 2008: Development and testing of polar Weather Research and Forecasting (WRF) model. Part I: Greenland ice sheet meteorology. *Mon. Wea. Rev.*, **36,** 1971-1989.

Hobbs, P. V. et al., 2000: Emissions from ships with respect to their effects on clouds. *J. Atmos. Sci.*, **57,** 2570-2590.

Hoinka, K. P., 1998: Temperature, humidity, and wind at the global tropopause. *Mon. Wea. Rev.*, **127**, 2248-2265.

Hong, S.-Y., J. Dudhia, and S.-H. Chen, 2004: A revised approach to ice microphysical processes for the bulk parameterization of cloud and precipitation. *Mon. Wea. Rev.*, **132,** 103-120.

Hong, S.-Y., and J.-O. J. Lim, 2006: The WRF single-moment 6-class microphysics scheme (WSM6). *J. Korean Meteor. Soc.*, **42,** 129-151.

Hudson, S. R., and R. E. Brandt, 2005: A look at the surface-based temperature inversion on the Antarctic Plateau. *J. Clim.*, **18**, 1673-1696.

Intergovernmental Panel on Climate Change (IPCC), 2001: Aerosols, their Direct and Indirect Effects, Primary and Secondary Sources of Aerosols: Sea Salt. *Climate Change 2001: The Scientific Basis, Working Group I.* Cambridge University Press, 297-299 pp.

Jacobson, M. Z., 2002: *Atmospheric Pollution: History, Science, and Regulation.* Cambridge University Press, 399 pp.

Jacobson, M. Z., 2005: *Fundamentals of Atmospheric Modeling.* Cambridge University Press, 2nd edition, 828 pp.

Janjić, Z. I., 1994: The step-mountain eta coordinate model: further developments of the convection, viscous sublayer and turbulence closure schemes. *Mon. Wea. Rev.*, **122,** 927-945.

Janjić, Z. I., 1996: The surface layer in the NCEP Eta Model. Eleventh Conference on Numerical Weather Prediction, Norfolk, VA, 19-23 August 1996. *American Meteorological Society*, Boston, MA, pp 354-355.

Janjić, Z. I., 2002: Nonsingular implementation of the Mellor-Yamada level 2.5 scheme in the NCEP meso model. NCEP Office Note No. 437, 61 pp.

Kankanala, P., 2007: Doppler sodar observations of the winds and structure in the lower atmosphere over Fairbanks, Alaska. M.S. Thesis, Department of Atmospheric Sciences, University of Alaska Fairbanks, 74 pp.

Klemp, J. B., and W. C. Skamarock, 2004: *Model Numerics for Convective Storm Simulation. Atmospheric Turbulence and Mesoscale Meteorology*, Cambridge University Press, 117-137 pp.

Korotkova, S., 2005: Simulation of particulate matter distribution over Iowa using the WRF-CHEM. M.S. Thesis, Department of Environmental Science, University of Northern Iowa, 126 pp.

Kukkonen, J., et al., 2005: Analysis and evaluation of selected local-scale PM_{10} air pollution episodes in four European cities: Helsinki, London, Milan and Oslo. *Atmos. Environ.*, **39,** 2759-2773.

Laprise, R., 1992: The Euler equations of motion with hydrostatic pressure as an independent variable. *Mon. Wea. Rev.*, **120,** 197-207.

Laroche, S., and R. Sarrazin, 2013: Impact of radiosonde balloon drift on numerical weather prediction and verification. *Wea. Forecasting*, **28,** 772-782.

Larsen, C. F., R. J. Motyka, J. T. Freymueller, K. A. Echelmeyer, and E. R. Ivins, 2005: Rapid viscoelastic uplift in southeast Alaska caused by post-Little Ice Age glacial retreat. *Earth Planet. Sci. Lett.*, **237,** 548-560.

Lawson, D., G. Wiles, and N. Weisenberg, 2011: Paleoclimate of the last 10,000 years, Glacier Bay National Park and Preserve: Progress understanding climate change in Southeast Alaska. U.S. Army Corps of Engineers, Cold Regions Research and Engineering Laboratory, Hanover, NH, 32 pp.

Levi, Y., E. Shilo, and I. Setter, 2011: Climatology of a summer coastal boundary layer with 1290-MHz wind profiler radar and a WRF simulation. *J. App. Meteor. Climatol.*, **50,** 1815-1826.

Madronich, S., 1987: Photodissociation in the atmosphere 1. Actinic flux and the effects of ground reflections and clouds. *J. Geophys. Res.*, **92,** 9740-9752.

Malm, W. C., J. F. Sisler, D. Huffman, R. A. Eldred, and T. A. Cahill, 1994: Spatial and seasonal trends in particle concentration and optical extinction in the United States. *J. Geophys. Res.: Atmospheres*, **99**, 1347-1370.

Mayfield, J. A., 2011: The micrometeorological effects of drainage flow in the winter atmospheric boundary layer. M.S. Thesis, Department of Atmospheric Sciences, University of Alaska Fairbanks, 184 pp.

Mayfield, J. A., and G. J. Fochesatto, 2013: The layered structure of the winter atmospheric boundary layer in the interior of Alaska. *J. App. Meteor. Climatol.,* **52**, 953-973.

McDowell Group, Inc., 2012: *Economic Impact of Visitors to Southeast Alaska, 2010-11*. Report prepared for the Alaska Wilderness League, 29 pp.

McGrath, R., T. Semmler, C. Sweeney, and S. Wang, 2006: Impact of balloon drift errors in radiosonde data on climate statistics. *J. Clim.*, **19**, 3430-3442.

Mellor, G. L., and T. Yamada, 1982: Development of a turbulence closure model for geophysical fluid problems. *Rev. of Geophys. Space Phys.*, **20**, 851-875.

Michael, M., A. Yadav, S. N. Tripathi, V. P. Kanawade, A. Gaur, P. Sadavarte, and C. Venkataraman, 2013: Simulation of trace gases and aerosols over the Indian domain: Evaluation of the WRF-Chem Model. *Atmos. Chem. Phys. Discuss.*, **13**, 12287-12336.

Middleton, P., W. R. Stockwell, and W. P. L. Carter, 1990: Aggregation and analysis of volatile organic compound emissions for regional modeling. *Atmos. Environ.*, **24A**, 1107-1133.

Milford, C., C. Marrero, C. Martin, J. J. Bustos, and X. Querol, 2008: Forecasting the air pollution episode potential in the Canary Islands. *Adv. Sci. Res.*, **2,** 21-26.

Mlawer, E. J., S. J. Taubman, P. D. Brown, M. J. Iacono, and S. A. Clough, 1997: Radiative transfer for inhomogeneous atmospheres: RRTM, a validated correlated-k model for the longwave. *J. Geophys. Res.*, **102**, 16663-16682.

Moldanová, J., E. Fridell, O. Popovicheva, B. Demirdjian, V. Tishkova, A. Faccinetto, and C. Focsa, 2009: Characterisation of particulate matter and gaseous emissions from a large ship diesel engine. *Atmos. Environ.*, **43**, 2632-2641.

Mölders, N., H. Hass, H. J. Jakobs, M. Laube, and A. Ebel, 1994: Some effects of different cloud parameterizations in a mesoscale model and a chemistry transport model. *J. App. Meteorol.*, **33**, 527-545.

Mölders, N., A. Raabe, and G. Tetzlaff, 1996: A comparison of two strategies on land surface heterogeneity used in a mesoscale beta meteorological model. *Tellus*, **48A**, 733-749.

Mölders, N., 2008: Suitability of the Weather Research and Forecasting (WRF) model to predict the June 2005 fire weather for Interior Alaska. *Wea. Forecasting*, **23,** 953-973.

Mölders, N., and G. Kramm, 2010: A case study on wintertime inversions in Interior Alaska with WRF. *Atmos. Res.*, **95,** 314-332.

Mölders, N., S. E. Porter, C. F. Cahill, and G. A. Grell, 2010: Influence of ship emissions on air quality and input of contaminants in southern Alaska National Parks and Wilderness Areas during the 2006 tourist season. *Atmos. Environ.*, **44,** 1400-1413.

Mölders, N., H. N. Q. Tran, P. Quinn, K. Sassen, G. E. Shaw, and G. Kramm, 2011: Assessment of WRF/Chem to simulate sub-Arctic boundary layer characteristics during low solar irradiation using radiosonde, SODAR, and surface data. *Atmos. Pol. Res.*, **2,** 283-299.

Mölders, N., H. N. Q. Tran, C. F. Cahill, K. Leelasakultum, and T. T. Tran, 2012: Assessment of WRF/Chem $PM_{2.5}$ forecasts using mobile and fixed location data from the Fairbanks, Alaska winter 2008/09 field campaign. *Atmos. Pol. Res.*, **3,** 180-191.

Mölders, N., S. Gende, and M. Pirhalla, 2013: Assessment of cruise-ship activity influences on emissions, air quality, and visibility in Glacier Bay National Park. *Atmos. Pol. Res.*, **4,** 435-445.

Monin, A. S., and A. M. Obukhov, 1954: Basic laws of turbulent mixing in the surface layer of the atmosphere. *Contributions of the Geophysical Institute of the Slovak Academy of Sciences*, **151,** 163-187.

Morgan, T., and R. D. Bornstein, 1977: Inversion climatology at San José California. *Mon. Wea. Rev.*, **105,** 653-656.

Mori, Y., 1986: Evaluation of several "Single-Pass" estimators of the mean and the standard deviation of wind direction. *J. Clim. Appl. Meteorol*, **25,** 703-707.

Motyka, R. J., L. Hunter, K. A. Echelmeyer, and C. Connor, 2003: Submarine melting at the terminus of a temperate tidewater glacier, LeConte Glacier, Alaska, U.S.A. *Annals of Glaciology*, **36,** 57-65.

Murphy, S. M., et al., 2009: Comprehensive simultaneous shipboard and airborne characterization of exhaust from a modern container ship at sea. *Environ. Sci Technol.*, **43,** 4626-4640.

Neiburger, M., D. S. Johnson, and C.-W. Chien, 1961: Studies of the structure of the atmosphere over the Eastern Pacific Ocean in summer: I. The inversion over the Eastern North Pacific Ocean. *University of California Publications in Meteorology*, Vol. 1, No. 1, 94pp.

Ngan, F., H. Kim, P. Lee, K. Al-Wali, and B. Dornblaser, 2013: A study of nocturnal surface wind speed overprediction by the WRF-ARW Model in Southeastern Texas. *J. App. Meteor. Climatol.*, **52,** 2638-2653.

PaiMazumder, D., and N. Mölders, 2009: Theoretical assessment of uncertainty in regional averages due to network density and design. *J. App. Meteor. Climatol.*, **48,** 1643-1666.

PaiMazumder, D., D. Henderson, and N. Mölders, 2012: Evaluation of WRF-Forecasts over Siberia: Air mass formation, clouds and precipitation. *The Open Atmospheric Sciences Journal*, **6,** 93-110.

Pavelsky, T., J. Boé, A. Hall, and E. Fetzer, 2011: Atmospheric inversion strength over polar oceans in winter regulated by sea ice. *Clim. Dyn.*, **36,** 945-955.

Peckham, S. E., G.A. Grell, S. A. McKeen, M. Barth, G. Pfister, C. Wiedinmyer, J. D. Fast, W. I. Gustafson, S. J. Ghan, R. C. Easter, J. Barnard, E. Chapman, 2011: WRF/Chem Version 3.3 User's Guide. 94 pp.

Pielke, R. A., 2001: *Mesoscale Meteorological Modeling.* 2nd ed. Academic Press, International Geophysics Series, Vol. 78, 676 pp.

Porter, S. E., 2009: Investigation of the impact of ship emissions on atmospheric composition and deposition into remote, coastal landscapes of Southwest Alaska. M.S. Thesis, Department of Atmospheric Sciences, University of Alaska Fairbanks, 112 pp.

Radke, L., J. Coakley, and M. King, 1989: Direct and remote sensing observations of the effects of ships on clouds. *Science*, **246,** 1146-1149.

Rosenfeld, D., 2003: Ship trails in the region off the Bay of Biscay. The Hebrew University of Jerusalem. Retrieved on March 1, 2013 from: http://oiswww.eumetsat.org/WEBOPS/iotm/iotm/20030127_shiptrails/20030127_shiptrails.html

Ruiz, J. J., C. Saulo, and J. Nogués-Paegle, 2010: WRF Model sensitivity to choice of parameterization over South America: Validation against surface variables. *Mon. Wea. Rev.*, **138,** 3342-3355.

Russell, L. M. et al., 1999: Aerosol dynamics in ship tracks. *J. Geophys. Res.*, **104**, 31077-31095.

Sakiyama, S. K., 1990: Drainage flow characteristics and inversion breakup in two Alberta mountain valleys. *J. App. Meteorol.*, **29,** 1015-1030.

Schell, B., I. J. Ackermann, H. Hass, F. S. Binkowski, and A. Ebel, 2001: Modeling the formation of secondary organic aerosol within a comprehensive air quality model system. *J. Geophys. Res.*, **106,** 28275-28293.

Schreier, M., A. A. Kokhanovsky, V. Eyring, L. Bugliaro, H. Mannstein, B. Mayer, H. Bovensmann, and J. P. Burrows, 2006: Impact of ship emissions on the microphysical, optical and radiative properties of marine stratus: A case study. *Atmos. Chem. Phys.*, **6,** 4925-4942.

Segele, Z., L. M. Leslie, and P. J. Lamb, 2013: Weather Research and Forecasting Model simulations of extended warm-season heavy precipitation episode over the US Southern Great Plains: Data assimilation and microphysics sensitivity experiments. *Tellus*, **65,** 1-28.

Serreze, M. C., and R. G. Barry, 2005: *The Arctic Climate System.* Cambridge University Press, 404 pp.

Serreze, M. C., J. D. Khal, and R. C. Schnell, 1992: Low-level temperature inversions of the Eurasian Arctic and comparisons with Soviet drifting station data. *J. Clim.*, **5,** 615-629.

Shulski, M., and G. Wendler, 2007: *The Climate of Alaska.* University of Alaska Press, 216 pp.

Simpson, D., A. Guenther, C. N. Hewitt, and R. Steinbrecher, 1995: Biogenic emissions in Europe. 1. Estimates and uncertainties. *J. Geophys. Res.*, **100D,** 22875-22890.

Skamarock, W.C., J.B. Klemp, J. Dudhia, D.O. Gill, D.M. Barker, M.G. Duda, X. Huang, W. Wang, and J.G. Powers, 2008: A description of the Advanced Research WRF Version 3. NCAR Technical Note, NCAR/TN–475+STR, 125pp.

Skamarock et al., 2011: Weather Research and Forecasting ARW Version 3 Modeling System User's Guide. National Center for Atmospheric Research Mesoscale and Microscale Meteorology Division, 362 pp.

Smirnova, T. G., J. M. Brown, and S. G. Benjamin, 1997: Performance of different soil model configurations in simulating ground surface temperature and surface fluxes. *Mon. Wea. Rev.*, **125,** 1870-1884.

Smirnova, T. G., J. M. Brown, S. G. Benjamin, and D. Kim, 2000: Parameterization of cold season processes in the MAPS land-surface scheme. *J. Geophys. Res.*, **105**, 4077-4086.

Snyder, J. M., 2007: Prospects for polar tourism. *The Polar Tourism Markets*. Edited by J. M. Snyder, and B. Stonehouse, CABI, Wallingford, 51-70 pp.

Stockwell, W. R., P. Middleton, J. S. Chang, and X. Tang, 1990: The second generation regional acid deposition model chemical mechanism for regional air quality modeling. *J. Geophys. Res.*, **95,** 16343-16367.

Stuefer, M., G. A. F. Grell, S. R. Kulchitsky, A. V., and G. B. Newby, 2009: WRF/Chem forecasting of wildfire smoke in Alaska. *American Geophysical Union,* Fall Meeting 2009, San Francisco, CA.

Sverdrup, H. U., 1933: *The Norwegian North Polar Expedition with the "Maud" 1918-1925: Scientific Results,* Vol. 2., Bergen, 527 pp.

Tran, H. N. Q., and N. Mölders, 2011: Investigations on meteorological conditions for elevated $PM_{2.5}$ in Fairbanks, Alaska. *Atmos. Res.*, **99,** 39-49.

Tran, H. N. Q., and N. Mölders, 2012: Numerical investigations on the contribution of point source emissions to the $PM_{2.5}$ concentrations in Fairbanks, Alaska. *Atmos. Pol. Res.*, **3,** 199-210.

U.S. Forest Service, 2011: *Lichens of Alaska's South Coast*. U.S. Forest Service Alaska Region, 16 pp.

U.S. Forest Service, 2012: *Air Program National Accomplishments and Successes: State of our National Forest Air*. Air Resource Management National Report, U.S. Forest Service, 23 pp.

von Storch, H., and F. Zwiers, 1999: *Statistical Analysis in Climate Research.* Cambridge University Press, 484 pp.

Vutukuru, S., and D. Dabdub, 2008: Modeling the effects of ship emissions on coastal air quality: A case study of southern California. *Atmos. Environ.*, **42,** 3751-3764.

Wendler, G., and K. Jayaweera, 1972: Some measurements of the development of the surface inversion in Central Alaska during winter. *Pure and Applied Geophysics*, **99,** 209-221.

Wendler, G., 1975: Relation between CO concentration and meteorological conditions in a subarctic community. *Journal de Recherches Atmospheriques*, **9,** 135-142.

Wendler, G., and P. Nicpon, 1975: Low-level temperature inversions in Fairbanks, Central Alaska. *Mon. Wea. Rev.*, **103,** 34-44.

Wesely, M. L., 1989: Parameterization of surface resistance to gaseous dry deposition in regional numerical models. *Atmos. Environ.*, **16,** 1293-1304.

Wexler, H., 1936: Cooling in the lower atmosphere and the structure of polar continental air. *Mon. Wea. Rev.*, **64,** 122-136.

Wright, S., A. Parker, C. Lancaster, E. Price, and R. Venables, 2012: Southeast Alaska by the Numbers. Paper presented at Southeast Conference, Sheinberg Associates, Juneau, AK, 12 pp.

Wyszogrodzki, A., Y. Liu, N. Jacobs, P. Childs, Y. Zhang, G. Roux, and T. Warner, 2013: Analysis of the surface temperature and wind forecast errors of the NCAR-AirDat operational CONUS 4-km WRF forecasting system. *Meteorol. Atmos. Phys.*, **122**, 1-19.

Yarker, M. B., D. C. PaiMazumder, C.F. Dehn, J., A. Prakash, and N. Mölders, 2010: Theoretical investigations on potential impacts of high-latitude volcanic emissions of heat, aerosols and water vapor and their interactions on clouds and precipitation. *The Open Atmospheric Sciences Journal*, **4,** 23-44.

Young, C., 2009: Disturbance of harbor seals by vessels in John Hopkins Inlet, Glacier Bay, AK. Moss Landing Marine Laboratories, San José State University, 112 pp.

Zhang, L., J. R. Brook, and R. Vet., 2003: A revised parameterization for gaseous dry deposition in air-quality models. *Atmos. Chem. Phys.*, **3,** 2067-2082.

Zhang, Y., P. Liu, B. Pun, and C. Seigneur, 2006: A comprehensive performance evaluation of MM5-CMAQ for the summer 1999 southern oxidants study episode, part I: Evaluation protocols, databases, and meteorological predictions (Supplement). *Atmos. Environ.*, **40,** 4825-4838.

Zhang, Y., M. K. Dubey, S. C. Olsen, J. Zheng, and R. Zhang, 2009: Comparisons of WRF/Chem simulations in Mexico City with ground-based RAMA measurements during the 2006-MILAGRO. *Atmos. Chem. Phys.*, **9,** 3777-3798.

Zhao, B. S. X. Wang, H. Liu, J. Y. Xu, K. Fu, Z. Klimont, J. M. Hao, K. B. He, J. Cofala, and M. Amann, 2013: NO_x emissions in China: historical trends and future perspectives. *Atmos. Chem. Phys.*, **13,** 9869-9897.

Zhao, Z., S.-H. Chen, M. J. Kleeman, M. Tyree, and D. Cayan, 2011: The impact of climate change on air quality-related meteorological conditions in California. Part I: Present time simulation analysis. *J. Clim.*, **24,** 3344-3361.

Zhong, S., H.-J. In, X. Bian, J. Charney, W. Heilman, and B. Potter, 2005: Evaluation of real-time high-resolution MM5 predictions over the Great Lakes Region. *Wea. Forecasting*, **20,** 63-81.

Zilitinkevich, S. S., 1995: Non-local turbulent transport: pollution dispersion aspects of coherent structure of convective flows. *Air Pollution III: Volume I. Air Pollution Theory and Simulation*, H. Power, N. Moussiopoulos, and C.A. Brebbia, Eds., Computational Mechanics Publications**,** 53-60 pp.

Appendix

A.1 Permission to use Fig. 2.8

Michael Pirhalla

From:	Bob Miller [bob@italio.com]
Sent:	Wednesday, June 19, 2013 10:15 AM
To:	'Michael Pirhalla'
Subject:	RE: Permisson to use image
Attachments:	YAK_pic14_Yakutat-aerials_ Museum.jpg; YAK_pic14-back side_Yakutat-aerials_ Museum.jpg; YAK_pic15_Yakutat-aerials_ Museum.jpg; YAK_pic15-back side_Yakutat-aerials_ Museum.jpg; YAK_pic16_Yakutat-aerials_ Museum.jpg; YAK_pic16-back side_Yakutat-aerials_ Museum.jpg; YAK_pic17_Yakutat-aerials_ Museum.jpg; YAK_pic17-back side_Yakutat-aerials_ Museum.jpg; YAK_pic19_Yakutat-aerials_ Museum.jpg; YAK_pic19-back side_Yakutat-aerials_ Museum.jpg

Hello Michael,

These photos were taken by the FAA and thus are public domain. I don't know who the original photographer was, other than "FAA Photo Lab". I have attached the photos also taken at the same time from other angles, plus what was on the backside of each photo for reference. Looks like they were taken in August 1959. Help yourself! If you would like to give any credit for them, would you mind referencing the Alaska Warbird Museum?

I have many more if you ever need them... ☺

Bob Miller

From: Michael Pirhalla [mailto:mapirhalla@alaska.edu]
Sent: Tuesday, June 18, 2013 5:34 PM
To: info@situk.com
Subject: Permisson to use image

Dear Bob,
I stumbled across your blog while google searching for information about the Yakutat airport. I'm a grad student working on a Masters thesis at UAF, and was hoping to use one of your images in my thesis:
http://situkriver.files.wordpress.com/2012/05/yak_pic19_yakutat-aerials_-museum.jpg.
I'm not sure if you're the owner of this picture, or maybe you can forward me to the person who is. I'm writing up an analysis using model weather data and comparing it to the Yakutat upper air (radiosonde – weather balloon) observations. I think this would be a nice addition to my thesis. You would of course, be properly cited.
Thanks,

Michael Pirhalla
Graduate Research Assistant
University of Alaska Fairbanks
Dept. of Atmospheric Sciences AKA 338A
903 Koyukuk Drive
Fairbanks, AK 99775
(907) 474-5704

A.2 Permission to use Fig. 2.9

Michael Pirhalla

From:	Upperair Upperair - NOAA Service Account [upperair@noaa.gov]
Sent:	Wednesday, July 17, 2013 3:32 AM
To:	Michael Pirhalla
Subject:	Re: Permission to Use Map Image

Flag Status: Flagged

Hello Mr. Pirhalla,

Sure, you may use the map. Just save it as a image file. Please note in your thesis that is was provided courtesy of the NOAA National Weather Service (NWS).

Sincerely,
Bill Blackmore
Meteorologist
NOAA National Weather Service HQ
United States Department of Commerce

On Tue, Jul 16, 2013 at 4:36 PM, Michael Pirhalla <mapirhalla@alaska.edu> wrote:

Hello,

I was hoping to gain permission to use the Alaska radiosonde network map located at: http://www.ua.nws.noaa.gov/nws_upper.htm for use in my Master's thesis. I am explaining the relatively sparse distribution of upper air sites in Alaska, and showing this map portrays a nice visual. If so, how might I site the image (other than the URL)?

Thank you,

Michael Pirhalla

Graduate Research Assistant

University of Alaska Fairbanks

Dept. of Atmospheric Sciences AKA 338A
903 Koyukuk Drive
Fairbanks, AK 99775

(907) 474-5704